Kent Academic Repository

Ahmad, Eamonn (2019) ***Photonic Time-Stretch Enabled High Throughput Microwave and MM-Wave Interferometry Applied to Fibre Grating Sensors and Non-Contact Measurement.*** **Doctor of Philosophy (PhD) thesis, University of Kent, Vrije Universiteit Brussel.**

Photonic Time-Stretch Enabled High Throughput Microwave and MM-Wave Interferometry Applied to Fibre Grating Sensors and Non-Contact Measurement

A Thesis Submitted to the University of Kent for the Degree
of Doctor of Philosophy in Electronic Engineering and to the
Vrije Universiteit Brussel for the
Degree of Doctor in Engineering Science (PhD).

By

Eamonn Jalal Ahmad

April, 2019

Statement of Authorship

I, Eamonn Jalal Ahmad, declare that this thesis entitled, 'Photonic Time-Stretch Enabled High Throughput Microwave and MM-Wave Interferometry, Applied to Fibre Grating Sensors and Non-Contact Measurement' and the work presented is explicitly my own except where identified to the contrary. This work was conducted under the supervision of Dr Chao Wang, Dr Paul Young and Prof Johan Stiens. I confirm that:

- This work was done wholly or mainly while in candidature for a research degree at the University of Kent, Canterbury and while collaborating joint research with the Vrije University Brussel (VUB), Belgium leading to a joint PhD award from both universities as well.

- Where I have consulted the published work of others, this is always clearly attributed.

- Where I have quoted from the work of others, the source is always given. Except for such quotations, this thesis is entirely my work.

- I have acknowledged all primary sources of help.

- Where the thesis is based on work done by myself jointly with others, I have made clear exactly what was done by others and what I have contributed myself.

Signed:

“*The science of today is the technology of tomorrow*.”

Edward Teller

ABSTRACT

The research presented in this thesis is focused towards developing real-time, high-speed applications, employing ultrafast optical microwave generation and characterisation techniques. This thesis presents a series of experiments wherein mode-locked laser pulses are utilised. Photonics-based microwave and MM-Wave generation and detection are explored and employed for applications pertaining to fibre grating sensors and non-contact measurement. The application concepts leverage techniques from optical coherence tomography and non-destructive evaluation of turbid media. In particular, I use the principle of dispersion-induced photonic Time-Stretch to slow down high-speed waveforms to speeds usable by state-of-the-art photo-detectors and digital signal processors. The concept of photonic time-stretch is applied to map instantaneous microwave frequency to the time instant of the signal, which in turn is related to spatial location as established by the space-wavelength-time conversions. The experimental methods applied throughout this thesis is based upon Michelson interferometer architecture.

My original contribution to knowledge is the realisation of Photonics-based, single tone, and chirped microwave and MM-Wave pulse generation applied to deciphering physical strain profile along the length of a chirped fibre Bragg grating employed in a Michelson interferometer configuration. This interrogation scheme allows intra-grating high-resolution, high-speed, and temperature independent strain measurement. This concept is further extended to utilise photonic generation of microwave pulses to characterise surface profile information of thin film and thin plate infrared transparent slides of variable thickness setup in a Michelson interferometer architecture. The method basis for photonically generated high-frequency microwave signals utilises the principle of photonic Time-Stretch. The research was conducted in the Photonics Lab at the University of Kent. In addition, the photonically generated microwave/ MM-Wave pulses is utilised as a potential broadband frequency-swept source for non-contact measurement of turbid media. Investigation of the proof-of-concept based on an MM-Wave coherence tomography set-up is implemented at Vrije Universiteit Brussel (VUB), Department of Electronics and Informatics (ETRO).

ACKNOWLEDGEMENT

I would like to thank my PhD thesis advisor Dr Chao Wang for his continuous support, valuable and superb guidance and active involvement throughout this work. He has been a source of constant encouragement and enthusiasm. Without his advice, trust and assistance, this work would have never been possible. Special thanks to Dr Paul Young, my second supervisor for his generosity in offering support and guidance whenever I approached him. I must mention Professor Johan Stiens from Vrije Universiteit Brussels (VUB), for his technical support and help in providing me access to millimetre wave lab at VUB. With his help, I was able to access facilities beyond University of Kent Photonics lab, explicitly working on V band physics and electronics helping me to expand the versatility of my thesis and enhance my skill set.

I would also like to thank the following people, who are current or former colleagues working with me in the Photonics Research Laboratory at the School of Engineering and Digital Arts, University of Kent: Irfan Ali, Guoqing Wang, Chaithanya Kumar, Usman Habib, Anthony and Shabnam Noor. In addition, colleagues at Vrije Universiteit Brussels (VUB) department of Electronics and Informatics, Ali Pourkazmi, Gokharna Pandey, Vincent and Nathalie. Their strong support and generous help significantly improved my research work. I will always cherish the good memories of working with them. My gratitude goes to all staff in the School of Engineering and Digital Arts and in particular Edwin Lui, Yan Zhang, Antonio Mendoza, Simon Jakes and Joanna Scamp of the IT and technical support department for their help throughout my research.

Finally, I am indebted to my parent’s Dr Hameed Ahmad and Mrs Alia Gul for their encouragement during my years of study, and my siblings, Nofal Ahmed and Zumar Ahmed for their support, understanding, encouragement and constant prayers throughout my research.

Please note: an editor has not been used in the construction of this thesis.

TABLE OF CONTENTS

CHAPTER 3: PHOTONIC TIME-STRETCH ENABLED HIGH THROUGHPUT DISTRIBUTED FBG SENSORS..56

CHAPTER 4: HIGH THROUGHPUT INTERFEROMETRY APPLIED TO DIMENSIONAL METROLOGY OF IR TRANSPARENT SAMPLES.........84

LIST OF PUBLICATIONS

Journal Papers

1. **E. J. Ahmad**, C. Wang, D. Feng, Z. Yan and L. Zhang, High Temporal and Spatial Resolution Distributed Fibre Bragg Grating Sensors Using Time-Stretch Frequency-Domain Reflectometry, "*Journal of Lightwave Technology,"* vol. 35, no. 16, pp. 3289-3295, 15 Aug. 2017.

Conference Papers

1. **E. J. Ahmad** and C. Wang, Photonic microwave frequency up-conversion using unbalanced temporal pulse shaping in a cascaded modulation scheme, "*14th International Conference on Optical Communications and Networks (ICOCN),"* Nanjing, China, 3-5 Jul. 2015.
2. **E. J. Ahmad**, C. Wang and J. Stiens, Broadband frequency swept millimeter-wave source based on cascaded temporal optical pulse shaping, "*2015 IEEE International Topical Meeting on Microwave Photonics (MWP),"* Paphos, Cyprus, 26-29 Oct. 2015.
3. **E. J. Ahmad**, D. Feng, and C. Wang, Analysis on spatial and temporal resolution in photonic Time-Stretch frequency domain reflectometry based fully distributed fibre Bragg grating sensors, "*The 15th International Conference on Optical Communications and Networks (ICOCN),"* Hangzhou, China, 22-26 Sep. 2016. (Invited)
4. **E. J. Ahmad**, C. Wang, D. Feng, Z. Yan, and L. Zhang, Ultrafast interrogation of fully distributed chirped fibre Bragg grating strain sensor, "*2016 IEEE Photonics Conference (IPC),"* Waikoloa, Hawaii, USA, 2-6 Oct. 2016.
5. D. Feng, **E. J. Ahmad**, and C. Wang, High-resolution crack detection using fully distributed chirped fibre Bragg grating sensors, "*The 6th Asia Pacific Optical Sensors Conference (APOS),"* Shanghai, China*,* 11-14 Oct. 2016.
6. C. K. Mididoddi, **E. J. Ahmed** and C. Wang, All-optical random sequence generation for compressive sensing detection of RF signals, *"2017 International Topical Meeting on Microwave Photonics (MWP),"* pp 1-4, Beijing, 2017.
7. C. K. Mididoddi, **E. J. Ahmad** and C. Wang, Data-efficient high-throughput fibre Bragg grating sensors using photonic time-stretch compressive sensing, *"Conference on Lasers and Electro-Optics Europe (CLEO-Europe),"* Munich, Germany, 25-29 June 2017.

LIST OF ABBREVIATIONS

ACC	Autonomous Cruise Control
ADC	Analogue to Digital Converter
AOM	Acousto Optic Modulator
AOTF	Acousto-optic Tunable Filter
ASE	Amplified Spontaneous Emission
AST	Anamorphic Stretch Transform
AWG	Arbitrary Waveform generator
B	External magnetic field
BPF	Bandpass filter
bps	Bit per second
BS	Beam Splitter
CFBG	Chirped Fibre Bragg Grating
CPA	Chirped Pulse Amplification
CSR	Carrier Suppression ratio
CT	Computed Tomography
CW	Continuous-wave
DAC	Digital-to-analogue converters
dB	Decibel
D	Electric displacement
DCF	Dispersion compensating fibre
DE	Dispersive Element
DL	Delay Line
DFB	Distributed Feedback
DFT	Discrete Fourier Transform
DOF	Depth of focus
DSP	Digital signal processor/processing
DST	Direct Space to Time
E	External electric field
EA	Electronic amplifier
EAM	Electro-absorption modulator

EDFA	Erbium-doped fibre amplifier
EM	Electromagnetic wave
EOM	Electro-optic modulator
ESA	Electrical Spectrum Analyser
FBG	Fibre Bragg Grating
FD-OCT	Frequency Domain – Optical Coherence Tomography
FFT	Fast Fourier Transform
FMCW RADAR	Frequency Modulated Continuous Wave RADAR
fs	Femto-second
FSR	Free Spectral Range
FT	Fourier Transform
FTIR	Fourier Transform Infrared Spectroscopy
FTM	Frequency-to-Time Mapping
FP	Fabry-Perot
FWHM	Full-width Half Mximum
Gbps	Gigabits per second
GDD	Group Delay Dispersion
GHz	Gigahertz
GVD	Group Velocity Dispersion
ICI	Inter-carrier interference
IEEE	Institute of Electrical and Electronics Engineers
IF	Instantaneous frequency
IM	Intensity Modulator
IR	Infrared
LC-FBG	Linearly Chirped Fibre Bragg Grating
LC-SLM	Liquid Crystal Spatial Light Modulator
LD	Laser diode
LO	Local oscillator
LOS	Light-of-sight
LPF	Low pass filter
LS	Least square
LTI	Linear Time invariant system

MEMS	Micro-Electro-Mechanical Systems
MHz	Megahertz
MIMO	Multiple-input, multiple-output
MISO	Multiple-input, single-output
MLL	Mode-Locked-Laser
MM-Wave	Millimetre-wave
MMF	multi-mode fibre
MPF	Microwave Photonic filter
MVNA	Microwave Vector Network Analyser
mW	Milli-Watt
MWP	Microwave Photonics
MZI	Mach-Zehnder interferometer
MZM	Mach-Zehnder modulator
NDE	Non-Destructive Evaluation
NDT	Non-Destructive Testing
NIR	Near Infrared
nm	Nano-metre
ns	Nano-second
NRW	Nicholson-Ross Weir method
OAWG	Optical arbitrary waveform generation
OBPF	Optical band-pass filter
OC	Optical Circulator
OCT	Optical Coherence Tomography
O/E	Optical to electrical conversion
OEO	Opto-electronic oscillator
OF	Optical Fibre
OIL	Optical Injection Locking
OPLL	Optical-Phase-Locked-Loop
OSA	Optical Spectrum Analyser
OSSR	Optical Sideband Suppression ratio
PAPR	Peak-to-average power ratio
PC	Polarisation Controller

PD	Photodiode
PIC	Photonic integrated circuit
PM	Phase modulator
ps	pico-second
RADAR	Radio Detection and Ranging
RF	Radio Frequency
RIN	Relative Intensity Noise
RoF	Radio-over-fibre
RT-FDTCT	Real-time Frequency-Domain THz coherence tomography
SAR	Synthetic Aperture RADAR
SCM	Suppressed Carrier Modulation
SG	Signal generator
SINR	Signal-to-interference plus noise
SLM	Spatial Light modulator
SMF	Single-mode fibre
SNR	Signal-to-noise ratio
S-parameter	Scattering Parameter
SSB	Single sideband
SS OCT	swept source optical coherence tomography
STFT	Short-Time-Fourier-Transform
SUT	Sample under Test
SVEA	Slowly Varying Envelope Approximation
TBWP	Time-Bandwidth Product
TE	Transverse Electric mode
THz	Terahertz
TM	Transverse Magnetic mode
TOD	Third order Dispersion
TPS	Temporal Pulse Shaping
UB-TPS	Unbalanced Temporal Pulse Shaping
UTC-PD	Uni-Traveling-Carrier Photodiode
UWB	Ultra-wide band
V-band	Frequency Range of 50 – 75 GHz

VCO	Voltage Controlled Oscillator
VNA	Vector Network Analyser
VSA	Vector Signal Analyser
VSG	Vector Signal Generator
WTM	Wavelength to Time mapping

LIST OF FIGURES

LIST OF TABLES

CHAPTER 1

INTRODUCTION

1.1 Microwave Photonics: Overview

Engineering technology and scientific concepts have emancipated themselves since the 1990s. Ubiquitous computing is already becoming a reality with the progress of information technologies like smartphones, tablet computers, wearable devices and other gadgets. Similarly, improvement in laser technology and fibre optics over the past two decades have contributed immensely to advancement in modern-day communication and sensing applications [1, 2].

Despite immense progress made in scientific technology, conventional means enabling high-speed real-time events such as cellular dynamics, microfluidic interrogation for rare cancer cells detection, chemical analytics and exploring rare events such as a random decay process amidst a million of background radiation in nuclear physics has always imposed technical challenges [3 – 5]. Slow temporal response and bandwidth characterise analogue electronic components. Similarly, analogue-to-digital conversion of high-speed signals requires tremendous sampling speeds, and signals obtained are usually buried in noise. Advanced signal processing algorithms are used to extract information in post-processing which generally involves approximations and iterations thus inhibiting accurate information retrieval and limiting system implementation to monitor real-time high-speed dynamic events.

The nature of leading-edge, advanced, coherent ultrashort laser pulses allows monitoring real-time events such as cellular dynamics, analytics governing chemical reactions at an ultrafast rate and novel concepts wherein ultrafast lasers form the base for quantum computing, atomic clocks and next-generation technology [6 – 8]. Thus, an ever-increasing interest in the field of photonics and electronics integration has been a critical scientific trend in the current decade.

The separation between conventional electronics and modern-day photonics had kept research communities apart. It became increasingly difficult to solve future problems by merely combining existing theories or incremental advance in electronics or photonic technology. This pursuit has led researchers to adopt a clean slate multi-disciplinary approach to tackling modern-day scientific problems and pave the way for future innovation. In this pursuit, a new systems science, which combines fundamentals of both electronics and photonics into one has been actively investigated and employed. This interdisciplinary scientific approach that combines electronics and photonics fundamentals is known as microwave photonics.

Microwave photonics studies the interaction between microwaves and optics [9 - 11]. Microwave photonic techniques, in essence, deal with the photonic generation, photonic processing, photonic distribution and photonic analogue-to-digital conversion of microwave signals. The term microwave in microwave photonics implies not only GHz but also THz frequencies and, equivalently, for picosecond or femtosecond timescales in the time domain. Processing information such as microwave signals in optical domain is assisted by the inherent low loss (0.2 dB/km) and high bandwidth capability of optics. Generation, control and distribution are not only limited to microwave domain, but the Radio Frequency (RF), millimetre-wave, sub Tera-Hertz (sub THz) and Tera-Hertz (THz) regime can all be exploited. Although, different research groups have defined the microwave, MM-Wave and THz regime into different frequency ranges, a standardized frequency range separating each spectral band is specified in this thesis. The RF spectra is the frequency range from 30 MHz to 300 MHz, the microwave regime corresponds to the frequency range 300 MHz to 30 GHz, the MM-Wave regime is identified as the frequency range from 30 GHz to 300 GHz whereas the sub THz and THz regime imply the 300 GHz to 1 THz and 1 THz to 10 THz frequency band respectively.

Microwaves and high-frequency MM-Waves have already found numerous applications such as communication channels for inter-satellite networking, military and defence communications, astronomical observations characterising the fabric of the cosmos and industrial non-destructive material evaluation techniques [12 – 15]. The industrial trend towards automation has opened the gateway to exploring both short range (few millimetres to 50 metres) and long range (~ 300 metres to several kilometres) non-contact sensing schemes wherein speed is essential for dynamic monitoring applications [16 – 18]. The autonomous car is a potential candidate that requires novel solutions enabling both long distance object detection and short distance strain detection for airbag activation in real time.

Microwave Photonic techniques employing ultra-short mode-locked laser pulses has established as an active area of research in recent years, transforming conventional microwave and MM-Wave generation utility. Inherent characteristics of coherent ultra-short state-of-the-art lasers allow broad spectral bandwidth and impressive pulse repetition rates can be applied to characterising high-speed dynamic events. State-of-the-art microwave photonic techniques have been used extensively to improving system performances in Radio Detection and Ranging (RADAR) and broadband communication, where wideband signals have the advantage of immunity to multipath interference and allow transmission of data rates at high-speed; microwave photonics also has applications in wireless sensor networks, warfare and instrumentation [19 - 21]. Microwave photonics technology is already an emerging field seeking cutting-edge solutions to a modern society with an ever-increasing bandwidth for technology. Figure 1 provides a generic classification of the microwave photonics application realm. Combining high-speed photonics with microwave and millimetre waves (MM-Wave) frequencies paves the way for future innovation.

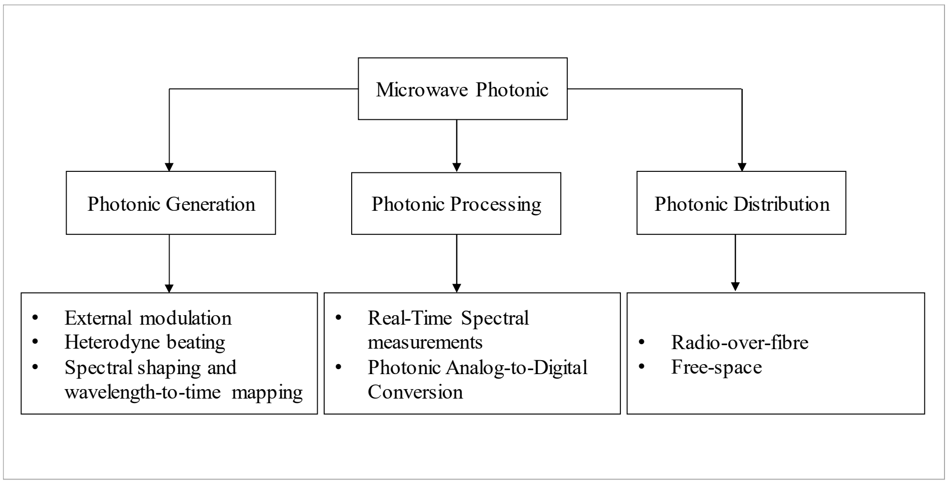

Figure 1.1 A simplified classification of the field of microwave photonics is depicted. This interdisciplinary field is located at the boundary between microwave and MM-Wave techniques and ultrafast electronics and photonic technologies, and typical investigations include, for example, high-speed microwave signal generation, signal processing and conversion, as well as the distribution and transmission of microwave signals via optical fibre.

Novel free space and fibre based solutions derived from state-of-the-art microwave photonic principles are explored and improvised upon as part of this thesis.

1.2 Motivation

The generation of millimetre waves or sub-Terahertz waves (frequency range 30 GHz – 1 THz) has been a challenging topic. Conventional means of generating millimetre waves based on electronics consists of many stages of frequency multiplication and filtering. However, the associated system is costly and complicated. Using high multiplication factors introduces a lot of non-linearity thus corrupting the signal with phase noise [19, 22, 23].

Similarly, real-time ultrafast measurement capability enhances system utility in dynamic applications such as surface vibration measurement, scanning large area in the shortest time possible, chemical analytics and biology. However, state-of-the-art engineering technologies, essential for studying ultrafast phenomenon are limited in speed and sensitivity due to compatibility mismatch with modern-day electronics [1 - 5]. Experimental research, aimed at investigating high-speed measurement and high speed scanning capability is desired.

Recent scientific innovation and inter-disciplinary efforts have explored the capability of microwave and MM-Wave and even THz in non-invasive sensing. Microwave offers deeper penetration capability however accompanied by a poor lateral resolution. Similarly, as the wavelength decreases up to the THz and sub THz regime, the penetration depth decreases, however, resolution improves. Thus, a broadband approach benefits from comprehending depth and resolution more precisely. The MM-Wave regime in particular provides a good compromise between penetration depth and resolution, and thus provides an interesting frequency band to explore for non-contact measurement solutions. Photonics presents a unique solution to the formation and detection of high-frequency microwave and millimetre wave (MM-Wave) signals by offering higher frequency, improved tunability and improved reconfigurability with the maximum microwave and MM-Wave bandwidth achieved constrained only by state-of-the-art photodetectors.

More importantly conventionally the generated microwave or millimetre-wave pulses are usually not chirped over a wide bandwidth. Chirp is defined as the linear increase or decrease in signal frequency with time. For many applications, frequency swept or chirped signals are highly desired in order to implement pulse compression at a receiver [24, 25]; frequency jammers can be countered by employing even wider band signals for transmitting information and swept source coherence tomography applications [26].

In addition, the development of fast femtosecond lasers has enabled active pulse shaping and optical arbitrary waveform generation techniques in photonics. Mode-locked lasers currently serve as the best means of generating pulses of very short duration and hence wide spectral bandwidth [27]. Cutting-edge state-of-the-art research is even working on realising coherent attosecond pulse trains. Using these femtosecond sources, a variety of applications, specifically pertaining to ultrafast phenomena such as chemical and biological applications, nonlinear optics, imaging, control of molecular and atomic processes, quantum control, and spectroscopy can be exploited [17, 18, 28]. Ultrafast phenomenon requires high throughput measurement schemes. The capability of utilising optics for microwave and MM-Wave/sub-THz generation and detection can enable a plethora of applications yet to be explored. Experimental research is still in its infancy stage and an attempt at developing novel and unique techniques exploring potential high throughput applications is presented in this thesis. High throughput refers to the high-speed signal generation, data acquisition and processing requirement.

The modern trend for microwave and MM-Wave equipment is growing at an enormous pace. The global microwave and MM-Wave market are forecast to grow from $47 million in 2012 to $482 million in 2022. Microwave photonic market in the Asia Pacific is expected to increase at a 26.50% annual rate between 2015 and 2022 [29, 30]. Essential applications ranging from concealed weapons and explosives detection to pharmaceutical quality assurance have already been executed using microwaves and MM-Waves with a vast market space still available.

1.3 Microwave Photonics: Applications

State-of-the-art exploration of microwave photonics technology is focussed on the photonic generation of microwave and MM-Wave signals. Many techniques demonstrating the photonic generation of microwave and MM-Wave signals have been realised. One of the most popular methods is based on optical to electrical conversion of a shaped time domain optical waveform [31, 32]. An ever-increasing interest into research and development of a novel microwave photonic source is observed since electromagnetic waves ranging from 30 - 300 GHz, covering the high-frequency microwave, MM-Wave and sub-THz regime are highly suited for spectroscopy and sensing applications [13 - 15]. They have found tremendous value in applications such as concealed weapons detection in airport security scanners and non-destructive testing of turbid media. Traditional sensing schemes demonstrate limited axial scan speed (~kHz) and thus an inability to monitor high-speed dynamic events. A high throughput ultrafast frequency swept source is required to explore potential applications wherein real time measurement is necessary. Similarly, utilising photonic detection of microwave and MM-Wave signals, measuring encoded spectral information translated to the time domain, one can enable fast measurement solutions as well.

Furthermore, sensing applications can be further grouped into fibre based sensing and non-invasive contactless sensing. The merger of photonics and microwave electronics as a combined field established as microwave photonics enables optical generation, processing and distribution capability of microwave and MM-Wave/sub-THz signals. Microwave Photonics allows novel techniques wherein microwave and MM-Wave/sub-THz signals can radiated into free space after photodetection using an antenna and also transported in fibre modulated over an optical carrier and down-converted to the electrical waveform at the photodetector.

The versatility of optical techniques demonstrating generation and detection of microwave and MM-Wave signals has paved the way for both distributed and embedded sensing applications pertaining to structural and civil engineering, aeronautical engineering and even MEMS technology [33, 34]. Thus, in this pursuit, both fibre based and free space-based solutions exploring its utility as a high throughput system is explored. Photonic microwave signal generation and detection applied to chirped fibre grating sensors and non-contact measurement have been adopted and implemented in this thesis.

1.3.1. Interrogation of Fibre Gratings Sensors

Fibre Bragg Gratings enable infinitesimal physical strain and ambient temperature changes to be monitored very efficiently. Change in strain and or temperature modifies both the effective refractive index and grating period of the FBG resulting in a shift in the reflected wavelength. Thus, the ability of FBGs to translate a change in its physical structure due to external strain and or temperature to a change in a measurable indicator, in this case, reflected Bragg wavelength, allows an FBG to be used as a sensor for physical strain and or temperature change measurement [35, 36]. Fibre Bragg grating based optical sensors offer many advantages such as lightweight, small size and a cost-effective market. They exhibit sturdiness over time, capable of weathering harsh environmental conditions and their size enables multiple FBGs to be structured [37], allowing the ability to communicate a vast amount of information over a complex, interconnected network. The work presented in [35] identifies a number of bus topology networks for remote fibre sensing over several kilometres. A tunable laser based fibre grating sensing scheme has been widely employed. In [36], the laser sweeps through a wide optical spectrum directed to an array of FBGs. The unstrained Bragg wavelengths of the FBGs are chosen such that the individual FBG reflection spectra do not overlap. An optical power meter detects the reflected light from the FBG array. FBG also opens the gateway for future civil engineering and aerodynamics applications enabling smart material integration allowing materials with real-time sensing and monitoring capability. Interrogation schemes relating the wavelength shift to external perturbation can be classified as follows;

- **Wavelength-Amplitude Conversion**: A change in the Bragg wavelength due to applied strain or temperature deviation can be related to the signal amplitude at the receiver by employing, e.g. an edge filter. The Wavelength-dependent power profile can be linked to detecting the shift in amplitude received [38, 40].
- **Wavelength-Frequency Conversion**: Wavelength-dependent transmission through an Acousto-Optic Tunable Filter (AOTF) based on fixed applied

radio frequency can be observed. Any deviation in the Bragg wavelength will result in a shift in the RF frequency [39].

- **Wavelength-Phase Conversion**: An interferometric set up such as an unbalanced Mach Zehnder modulator translating the wavelength shift to a phase shift that can be detected based on lock-in detection and or a phase meter can also be used for FBG interrogation [40].
- **Wavelength-Position Conversion**: A spectrometer can be employed that spreads the spectrum along an array of CCD detectors. A shift in Bragg wavelength will be diffracted in a different direction and translated to a shift in position on the detector thus illuminating different areas of pixel [41, 42].
- **Wavelength-Time Conversion**: Novel demodulation schemes using highly dispersive fibre translating grating wavelength change to a shift in the arrival time of the reflected pulse have been implemented [43]. In the time domain, the reflected signal from an array of FBGs can be intuitively understood as a series of pulses separated by time of flight between the gratings in addition to a Wavelength-dependent delay resulting from the two-fold pass through the DCF. Ultrafast and precise interrogation of FBG sensors based on WTM incorporating higher order dispersion has been previously demonstrated [44]. Higher order dispersion introduces a frequency chirp to the original ultrashort pulse.

Fibre based solutions benefit from low insertion loss, immunity to electromagnetic interference, ability to function in harsh environments such as in high voltage machinery and compatibility with fibre optics systems [37, 41]. Despite the many advantages offered by fibre based sensors, the commercial market has still not fully accepted fibre based sensors, mainly due to the already well established traditional methods occupying a considerable market share. However, recent success with novel techniques achieving real-time ultra-fast sensing capability, fibre based solutions are increasingly sought after.

1.3.2. Non-Contact Measurement

Similarly, utilising the free space emission of frequency swept MM-Wave pulses, one can take advantage of the optimum resolution and penetration depth achieved by MM-Waves for non-invasive contact-less imaging and depth profiling or ranging along with the enhanced real-time measurement capability and high sensitivity provided by the advantages that stem from the Photonics-based technique itself.

The generation of MM-Waves, essentially frequency band, 30 to 300 GHz is crucial due to its uniquely identified features such as the ability to penetrate fog, clouds, snow and dust storm. These features enable MM-Waves to be applied in various fields, namely, inter-satellite links, high capacity terrestrial MM-Wave communication systems. Defence applications include RF jamming techniques employing wide bandwidth signals to block a considerable portion of the electromagnetic spectrum. Autonomous Cruise Control (ACC) radar, military applications for a wide range of sensors, missile seeker and fire control functions. Moreover, MM-Wave imaging applied in airport security scanners for concealed weapons detection and explosives. Broad bandwidth microwave and MM-Wave signals have also been employed for secure communication due to its lower probability of interception and effective material penetration capability [12, 13].

Traditional Non-Destructive measurement schemes can be broadly classified based on the electromagnetic wavelength utilised. Infrared obtains thermography, high energy electromagnetic waves for radiography testing. Light, for optical coherence tomography, state-of-the-art solutions rely on principles of LIDAR and Laser Doppler Vibrometry [45]. Laser triangulation measures distance by calculating the reflected angle. Some advanced solutions include Acoustic force microscopy, which is characterised by a slow measurement speed; confocal laser microscopy and white light interferometry are also employed. Existing tools characterising surface profile information are large in size and or require some sort of material contact and thus destructive in nature. The resolution capability is usually associated with wavelength employed and spectroscopic techniques are characteristically slow, yielding a trade-off with measurement speed. The merger of photonics and electronics as microwave photonic techniques paves the way for novel ultrafast and ultrahigh-resolution demodulation schemes.

Microwave photonic techniques for high throughput fibre Bragg grating sensing and non-contact measurement are investigated as part of this research. Moreover, the findings of this thesis sow the ideal tools for detecting rare high-speed events and monitoring real-time dynamics at ultrahigh-resolution. The photonic means of high-frequency chirped pulse generation is demonstrated to be extremely reconfigurable. High-speed Terahertz signals can be radiated into free space as well; the maximum bandwidth achieved is constrained only by the bandwidth of state-of-the-art photodetectors, in addition, inherent limitations employed for post-processing is revealed by the research analysis. The need for an improved signal processing algorithm for extracting information encoded within the instantaneous frequency of microwave and MM-Wave pulse is highlighted due to Short Time Fourier Transforms time and frequency resolution trade-off.

A critical review of traditional schemes enabling non-contact measurement is presented in Chapter 2. The techniques adopted in this thesis for non-contact measurement are inspired from the fundamentals of photonic Time-Stretch and Michelson interferometry. Both photonic generation and photonic detection of microwaves and MM-Waves are explored; the experimental method for non-contact measurement is applied to both infrared and MM-Wave regimes.

1.4 Research Hypothesis and Objectives

Photonic generation, processing and distribution of microwave and MM-Wave signals has shown great promise as compared to conventional means of microwave and MM-Wave generation based on electronics [31, 32]. The research hypothesis revolves around the aim of utilising mode locked laser pulses for broad bandwidth microwave and MM-Wave generation and detection. The capability of optics to generate ultrashort laser pulses (~ ns) and an ultrafast microwave and MM-Wave frequency chirp (~ GHz) within the short temporal pulses for generation and detection would enable high-speed non-contact measurement solutions. Though, a commercial solution is yet to mature, increasing interest in Photonics-based schemes for implementing microwave and MM-Wave signals have led to the implementation of novel techniques realising the theoretical principles. The most common method amongst the various microwave photonic generation techniques applied is based on harnessing the phenomena of dispersion enabling photonic Time-Stretch and or wavelength to time mapping (WTM) [43].

The focus on optical arbitrary waveform generation (OAWG) and pulse shaping in recent years have been due to the capability of using photonics techniques that have a more enormous potential to generate complex high-frequency waveforms than current techniques that can currently only generate arbitrary signals limited up to a few GHz [8 – 10]. This results from the fact that traditional techniques have to rely on electronic circuits to produce arbitrary waveforms and these circuits suffer from inherent speed and bandwidth limitations [11].

Photonic generation of microwave signals can be tailored to generate microwave and MM-Wave signals with a large Time-Bandwidth Product (TBWP) enabling applications in a wide range of scientific disciplines including defence, wireless and satellite communications, optical signal processing [16] and medical imaging systems using both Terahertz (THz) waves and optical coherence tomography techniques [19 – 21]. The Time Bandwidth Product (TBWP) of a pulse is the product of its temporal and spectral Full Width Half Maximum (FWHM) and is essentially a figure of merit for the signal and in the optical domain determines how close the optical pulse is to its bandwidth limit, i.e. the minimum possible duration achieved by a pulse for a given bandwidth. In RADAR design, the TBWP signifies design parameters limiting the receiver bandwidth to mitigate additional noise being collected. Also, the transport of the generated microwave and MM-Wave signals over large distances via coaxial cables is accompanied by high loss. Similarly, millimetre wave signals in free space attenuate rapidly due to humidity in the air. Photonic generation and further on the distribution of MM-Wave signals over long distances via optical fibres provides a much better solution [22, 31]. Recent progress in microwave photonic techniques employing both free space and fibre based microwave and MM-Wave generation and detection schemes also pave the way for ultrafast measurement capability in applications pertaining to structural health monitoring, non-contact measurement and infrared transparent samples metrology as laid out in this thesis.

Research objectives met include

- Enable a novel scheme utilising photonic microwave detection for chirped fibre Bragg grating based high-throughput intra-grating strain sensing.

- Improvise upon the proposed concept and utilise the photonic detection of microwave and MM-Wave signals for applications pertaining to dimensional metrology of infrared transparent samples.
- Implementation of frequency swept MM-Wave pulse source and exploring its utility as a source for MM-Wave coherence tomography in High-throughput NDT application.

1.5 Research Significance

The primary work presented in this thesis concerns exploring and improving upon cutting-edge state-of-the-art microwave photonic techniques for generation and detection of broadband microwave and MM-Wave signals. Applications pertaining to deciphering physical strain upon a chirped fibre Bragg grating and obtaining surface profile information and material thickness non-invasively at high throughput, axial scan rate corresponding to 50 MHz are explored. An implementation of the system concept is demonstrated.

Both free space and fibre-based solutions are investigated. The principal advantage of using free space optics is its reconfigurability. The major limitation of an optical system based on free space optics is a large size. In addition, a strict alignment of the devices is needed which makes the system complicated. Fibre based solutions benefit from the ease of installation, limited power loss, and is thus more promising. The advantages associated with each applied method and the limitations of each technique are addressed in this thesis.

The unique contribution of this thesis include:

- Firstly, carrying out an experiment that enables high-speed, high sensitivity, and temperature independent strain sensing capability along the length of a chirped fibre Bragg grating. Optical Time-Stretch frequency domain reflectometry is applied to obtain a novel interrogation technique for fully distributed linearly chirped fibre Bragg grating (LCFBG) strain sensors with simultaneous high temporal and spatial resolution [46]. A multi-point high throughput interrogation scheme allowing fully distributed sensing is compared to conventional quasi-distributed and distributed sensing.

- In addition, a novel application concept amalgamating pulse propagation in thin films, optical coherence tomography and photonic Time-Stretch has been proposed and implemented for determining the thickness of infrared transparent samples based on the instantaneous frequency estimation at micrometre scale resolution. The instantaneous spatial location can be calculated from the time instant of the signal thus enhancing its capacity in dynamic event monitoring applications. Short Time Fourier transformation is employed for post-processing of time domain signal obtained in both fibre grating sensors and infrared transparent surface metrology applications.
- Finally, photonic time-stretch enabled microwave and MM-Wave generation is explored for mocking a unique MM-Wave source that would allow for MM-Wave coherence tomography at an unprecedented axial scan rate. The unbalanced temporal pulse shaping is explored, and improvement upon existing techniques have been demonstrated mainly based on simulations. A chirped MM-Wave source with enhanced TBWP is produced [49, 50]. The experimental challenges and limitations are outlined. Alternatively, the generation of broadband MM-Wave pulses based on all fibre based differential dispersion mechanism is experimentally demonstrated. Pure MM-Wave coherence tomography is performed; utility of a novel sensing source in non-contact dimensional metrology at an ultra-fast rate, corresponding to the repetition rate of the mode-locked laser source is proposed and explored.

A list of publications produced as a result of the work carried out as part of this thesis is provided in the references [46 – 53].

1.6 Thesis Outline

This research aims at applying novel system concepts to enable high throughput measurements utilising Michelson interferometer based architecture for fibre grating sensing and non-contact measurement applications. It is believed that photonic Time-Stretch enabled Wavelength-to-Time mapping would provide a

means of analysis in the temporal domain thus allowing high-speed signal generation, processing and detection.
This thesis is structured as follows:

Chapter 2 focuses on the underlying theoretical basis, the mathematical model-relating signal Free Spectral Range (FSR) to frequency detected in the time domain. The propagation of ultra-short optical pulses and principle of photonic Time-Stretch and dispersive Fourier transformation are elaborated. An overview of main photonic microwave and MM-Wave generation schemes and electromagnetic waves based non-destructive material characterisation techniques have been provided. Similarly, performances of the underlying techniques were compared.

Chapter 3 focuses on fibre gratings and CFBG sensing. The adaptation and implementation of a novel interrogation scheme for physical strain sensing, principle, and experimental results are presented.

Chapter 4 introduces another novel technique for surface profiling of infrared transparent samples by amalgamating optical coherence tomography and dispersive Fourier transformation. System concept, experimental results and limitations are discussed.

Chapter 5 focusses on the chirped microwave and MM-Wave generation schemes adopted at the University of Kent and the utilization of the generated microwave and MM-Wave signal for propagation in free space and MM-Wave coherence tomography applications for optical path length difference measurement at Vrije Universiteit Brussel, Belgium.

Chapter 6. Finally, this chapter summarises the key findings of this research and offers some recommendations for future work in the area of photonic Time-Stretch enabled high throughput microwave and MM-Wave interferometry.

REFERENCES

[1] M. Azadeh, *Fibre Optics Engineering*: Springer US, 2009.

[2] R. R. Alfano, *The Supercontinuum Laser Source*: Springer New York, 2013.

[3] H. R. Petty, "Spatiotemporal chemical dynamics in living cells: From information trafficking to cell physiology, " *Biosystems,* vol. 83, pp. 217-224, 2006.

[4] J. P. Gleghorn, E. D. Pratt, D. Denning, H. Liu, N. H. Bander, S. T. Tagawa, D. M. Nanus, P. A. Giannakakou, B. J. Kirby, "Capture of circulating tumor cells from whole blood of prostate cancer patients using geometrically enhanced differential immunocapture (gedi) and a prostate-specific antibody", *Lab on a Chip,* vol. 10, no. 1, pp. 27 – 29, 2010.

[5] D. R. Solli, C. Ropers, P. Koonath, B. Jalali, "Optical rogue waves," *Nature*, vol. 450, pp. 7172, 2007.

[6] F. Riehle, "Optical Atomic Clocks for a Future New Definition of the Second," in CLEO: 2014, *OSA Technical Digest (online) Optical Society of America*, 2014.

[7] J. Capmany and D. Novak, "Microwave photonics combines 2 worlds," *Nature Photonics,* vol. 1, pp. 319-330, 2007.

[8] J. Capmany, G. Li, C. Lim, and J. Yao, "Microwave Photonics: Current challenges towards widespread application," *Optics Express,* vol. 21, pp. 22862-22867, 2013.

[9] A. J. Seeds, "Microwave Photonics," *IEEE Transactions on Microwave Theory and Techniques,* vol. 50, pp. 877 - 887, 2002.

[10] J. Yao, "Microwave photonics," *Lightwave Technology, Journal of,* vol. 27, pp. 314-335, 2009.

[11] C. H. Lee, *Microwave Photonics, Second Edition*: Taylor & Francis, 2013.

[12] A. Y. Nashashibi, K. Sarabandi, P. Frantzis, R. D. D. Roo, and F. T. Ulaby, "An ultrafast wide-band millimeter-wave (MM-WAVE) polarimetric radar for remote sensing applications," *IEEE Transactions on Geoscience and Remote Sensing,* vol. 40, pp. 1777 - 1786, 2002.

[13] S. Chen, J. Kupershmidt, K. Korolev, and M. Afsar, "A High-resolution Quasi Optical Spectrometer for complex permittivity and loss tangent measurements at Millimeter Wavelengths," in *Instrumentation and Measurement Technology Conference Proceedings*, Warsaw, pp. 1 – 5, 2007.

[14] J. M. Payne, J. W. Lamb, J. G. Cochran, and N. Bailey, "A new generation of SIS receivers for millimeter-wave radio astronomy," *Proceedings of the IEEE,* vol. 82, pp. 811 - 823, 1994.

[15] W. F. Moulder, "Development of a high-throughput microwave imaging system for concealed weapons detection," presented at the *IEEE International Symposium on Phased Array Systems and Technology (PAST)*, Waltham, MA, USA, 2016.

[16] R. A. Minasian, X. Yi, and L. Li, "Microwave photonic processing of high-speed microwave signals," presented at the *18th International Conference on Transparent Optical Networks (ICTON),* Trento, 2016.

[17] D. Brinks, R. Hildner, E. M. H. P. van Dijk, F. D. Stefani, J. B. Nieder, J. Hernando, and N. F. van Hulst, "Ultrafast dynamics of single molecules," *Chemical Society Reviews,* vol. 43, pp. 2476-2491, 2014.

[18] N. L. Gruenke, M. F. Cardinal, M. O. McAnally, R. R. Frontiera, G. C. Schatz, and R. P. Van Duyne, "Ultrafast and nonlinear surface-enhanced Raman spectroscopy," *Chemical Society Reviews,* vol. 45, pp. 2263-2290, 2016.

[19] T. Isogawa, T. Kumashiro, S. Ho-Jin, K. Ajito, N. Kukutsu, K. Iwatsuki, and T. Nagatsuma, "Tomographic Imaging Using Photonically Generated Low-Coherence Terahertz Noise Sources," *Terahertz Science and Technology, IEEE Transactions on,* vol. 2, pp. 485-492, 2012.

[20] M. L Dufour, G. Lamouche, V. Detalle, B. Gauthier, and P. Sammut, "Low-coherence interferometry - An advanced technique for optical metrology in industry," *Insight - Non-Destructive Testing and Condition Monitoring,* vol. 47, 2005.

[21] J. Xu, C. Zhang, J. Xu, K. K. Y. Wong, and K. K. Tsia, "Megahertz all-optical swept-source optical coherence tomography based on broadband amplified optical time-stretch," *Optics Letters,* vol. 39, pp. 622-625, 2014.

[22] J. Yao, "Photonic generation of microwave arbitrary waveforms," *Optics Communications,* vol. 284, pp. 3723-3736, 2011.

[23] E. Kemptner and S. Thurner, "Free space material characterisation for microwave frequencies," presented at *the 6th European Conference on Antennas and Propagation (EUCAP)*, Prague, 2012.

[24] C. Wang and J. Yao, "Photonic generation of chirped microwave pulses using superimposed chirped fibre Bragg gratings," *IEEE Photonics Technology Letters,* vol. 20, no. 11, pp. 882-884, June 2008.

[25] J. Chou, Y. Han, and B. Jalali, "Adaptive RF-photonic arbitrary waveform generator," in *Microwave Photonics, 2002. International Topical Meeting on*, pp. 93-96, 2002.

[26] P. A. Testoni, "Optical Coherence Tomography," *The Scientific World JOURNAL,* vol. 7, 2007.

[27] Z. Jiang, D. E. Leaird, and A. M. Weiner, "Line-by-Line Pulse Shaping Control for Optical Arbitrary Waveform Generation," in *Conference on Lasers and Electro-Optics/Quantum Electronics and Laser Science Conference and Photonic Applications Systems Technologies*, Long Beach, California, 2006.

[28] B. Gu, C. Zhao, A. Baev, K.-T. Yong, S. Wen, and P. N. Prasad, "Molecular nonlinear optics: recent advances and applications," *Advances in Optics and Photonics,* vol. 8, pp. 328-369, 2016.

[29] K. Boutros, W. B. Luo, Y. Ma, G. Nagy, J. Hacker, "5W GaN MMIC for millimeter-wave applications," *Compound Semiconductor Integrated Circuit Symposium*, 2006.

[30] U. Pfeifer, J. Grzyb, D. Liu, B. Gaucher, T. Beukema, B. Floyd, S. Reynolds, "A chip scale packaging technology for 60 GHz wireless chip set," *IEEE Transactions on Microwave Theory and Technology*, vol. 54, no. 8, pp. 3387 – 3397, 2006.

[31] C. Hao, Z. Fei and Y. Jianping, "Photonic Generation of Microwave Signals Based on Pulse Shaping," *Photonics Technology Letters, IEEE*, vol. 19, pp. 668-670, 2007.

[32] C. B. Huang, Z. Jiang, D. Leaird, J. Caraquitena and A. Weiner, "Spectral line-by-line shaping for optical and microwave arbitrary waveform generations," *Laser & Photonics Reviews*, vol. 2, pp. 227-248, 2008.

[33] F. Zhang, X. Ge, and S. Pan, "Background-free pulsed microwave signal generation based on spectral shaping and frequency-to-time mapping," *Photonics Research,* vol. 2, pp. 5-10, 2014.

[34] J. Arana and L. R. Chen, "Pulse shaping using a space-to-frequency-to-time mapping technique," *Lasers and Electro-Optics CLEO '02. Technical Digest.*

Summaries of Papers Presented at the, Long Beach, CA, USA, pp. 358-359 vol.1, 2002.

[35] M Fernandez-Vallejo and M. Lopez-Amo “Optical Fiber Networks for Remote Fiber Optic Sensors.” *Sensors*. vol. 20, no. 4, 2012.

[36] M. J. Connelly, S. Moloney, and P. Butler "Tunable laser based carbon composite strain sensing system using wavelength division multiplexed fiber Bragg grating sensors", *SPIE Conference Proceedings*, pp. 5758, Smart Structures and Materials: Smart Sensor Technology and Measurement Systems, 2005.

[37] A. Kersey, M. A. Davis, H. J. Patrick, M. Leblanc, K. P. Koo, C. G. Askins, M. A. Putnam, and E. J. Friebele, "Fibre grating sensors," *Lightwave Technology, Journal of,* vol. 15, pp. 1442-1463, 1997.

[38] S. M. Melle, K. Liu and R. M. Measures, "A passive wavelength demodulation system for guided-wave Bragg grating sensors," in *IEEE Photonics Technology Letters*, vol. 4, no. 5, pp. 516-518, 1992.

[39] B. Griffin and M. J. Connelly, "Digital Signal Processing of interferometric fibre optic sensors," in *Proceedings of the Lightwave Technologies in Instrumentation and Measurement Conference*, Palisades, NY, USA, pp. 153 – 156, 2004.

[40] A. B. Lobo Ribeiro, L. A. Ferreira, M. Tsvetkov, and J. L. Santos, “All-fibre interrogation technique for fibre Bragg sensors using a biconical fibre filter,” *Electronics Lett.*, vol. 32, no. 4, pp. 382–383, 1996.

[41] C. R. Giles, "Lightwave applications of fibre Bragg gratings," *Journal of Lightwave Technology*, vol. 15, no. 8, pp. 1391-1404, Aug. 1997.

[42] J. Hervás, J. Madrigal, D. Barrera and S. Sales, "Multiplexing FBG sensors combining microwave photonics and phase modulation," *2017 19th International Conference on Transparent Optical Networks (ICTON)*, pp. 1-4, Girona, 2017.

[43] M. Lei, W. Zou, X. Li and J. Chen, "Ultrafast FBG Interrogator Based on Time-Stretch Method," in *IEEE Photonics Technology Letters*, vol. 28, no. 7, pp. 778-781, April, 2016.

[44] B. Culshaw, "Optical fibre sensor technologies: opportunities and-perhaps-pitfalls," in *Journal of Lightwave Technology*, vol. 22, no. 1, pp. 39-50, Jan. 2004.

[45] S.J. Rothberg, M.S. Allen, P. Castellini, D. Di Maio, J.J.J. Dirckx, D.J. Ewins, B.J. Halkon, P. Muyshondt, N. Paone, T. Ryan, H. Steger, E.P. Tomasini, S.

Vanlanduit, J.F. Vignola, “An international review of laser Doppler vibrometry: Making light work of vibration measurement”, *Optics and Lasers in Engineering*, vol. 99, pp. 11-22, 2017.

[46] E. J. Ahmad, C. Wang, D. Feng, Z. Yan and L. Zhang, “High Temporal and Spatial Resolution Distributed Fibre Bragg Grating Sensors Using Time-Stretch Frequency-Domain Reflectometry,” *Journal of Lightwave Technology*, vol. 35, no. 16, pp. 3289-3295, 15 Aug. 2017.

[47] E. J. Ahmad, C. Wang, D. Feng, Z. Yan, and L. Zhang, “Ultrafast interrogation of fully distributed chirped fibre Bragg grating strain sensor,” 2016 *IEEE Photonics Conference (IPC)*, Waikoloa, Hawaii, USA, 2016.

[48] E. J. Ahmad, D. Feng, and C. Wang, “Analysis on spatial and temporal resolution in photonic Time-Stretch frequency domain reflectometry based fully distributed fibre Bragg grating sensors,” *The 15th International Conference on Optical Communications and Networks (ICOCN)*, Hangzhou, China. (Invited), 2016

[49] E. J. Ahmad, C. Wang and J. Stiens, “Broadband frequency swept millimeter-wave source based on cascaded temporal optical pulse shaping,” 2015 *IEEE International Topical Meeting on Microwave Photonics (MWP),* 26-29, Paphos, Cyprus, 2015.

[50] E. J. Ahmad and C. Wang, “Photonic microwave frequency up-conversion using unbalanced temporal pulse shaping in a cascaded modulation scheme,” 14th *International Conference on Optical Communications and Networks (ICOCN)*, pp. 3-5, Nanjing, China, 2015.

[51] D. Feng, E. J. Ahmad, and C. Wang, “High-resolution crack detection using fully distributed chirped fibre Bragg grating sensors,” *The 6th Asia Pacific Optical Sensors Conference (APOS),* pp. 11-14, Shanghai, China, 2016.

[52] C. K. Mididoddi, E. J. Ahmed and C. Wang, All-optical random sequence generation for compressive sensing detection of RF signals, *“2017 International Topical Meeting on Microwave Photonics (MWP),”* pp 1-4, Beijing, 2017.

[53] C. K. Mididoddi, E. J. Ahmad and C. Wang, Data-efficient high-throughput fibre Bragg grating sensors using photonic time-stretch compressive sensing, *“Conference on Lasers and Electro-Optics Europe (CLEO-Europe),”* Munich, Germany, 25-29 June 2017.

CHAPTER 2

BACKGROUND STUDY AND LITERATURE REVIEW

Chapter 1 is devoted to the introduction, motivation and state-of-the-art overview of microwave photonic techniques applied to practical solutions for fibre grating sensors and non-contact measurement. In this chapter, I demonstrate the theoretical basis that leads to sensing schemes based on photonic Time-Stretch enabled microwave and MM-Wave interferometry. A mathematical study of ultra-short optical pulse propagation is provided followed by the concept of photonic Time-Stretch enabled dispersive Fourier transformation. A literature review of state-of-the-art Photonics-based microwave and MM-Wave generation schemes and non-contact measurement techniques are presented. The theoretical model shown in this chapter is further utilised and expanded to fibre grating strain sensors application and non-contact sensing in the following chapters.

2.1 Ultra-short Optical Pulse Propagation in Optical Fibre

Electromagnetism is necessarily the study of the relationship between electric and magnetic fields. Combining Faraday and Gauss's law, James Maxwell was able to unify the entirety of electromagnetism into a set of 4 equations that became known as Maxwell's equations [1, 2]. The crux of Maxwell's equations is that a changing magnetic field, B, would induce a changing electric field, E, which in turn would produce a changing magnetic field and so on. The net result of these changing fields would consist of changing E and B that can propagate through space as electromagnetic waves. Thus, the inter-dependency of electric and magnetic field allows either of the field quantity to express an electromagnetic wave. We employ the electric field E as the basis function for explaining theoretical fundamentals in this chapter and where applicable throughout this thesis. An accelerated charge would radiate electromagnetic waves, i.e. alternating electric and magnetic field propagating through space. Many different types of electromagnetic fields exist;

they differ from each other based on the frequency and or wavelength of the wave. The electromagnetic spectrum with the low frequency Radio Frequency band omitted is depicted in Figure 2.1 as follows:

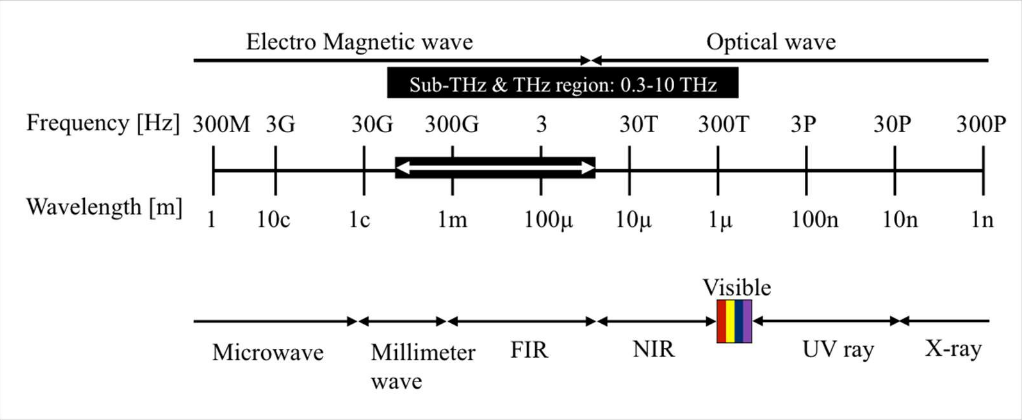

Figure 2.1 Time-varying electric and magnetic fields also known as electromagnetic waves must satisfy Maxwell's equations. The MM-Wave and sub-terahertz (sub-THz) range of the electromagnetic wave spectrum is the spectral band of 30 GHz to 3 THz, which corresponds to the wavelength region from 10mm-100µm. This region lies at the interface between electronics and photonics and is an underdeveloped region from an industrial point of view.

A plane wave solution to the wave equation is characterised as a complex exponential function. The general solution takes the form:

$$\mathbf{E}(\mathbf{z},t) = E_0 e^{i(\omega t - \mathbf{kz} + \phi)} = E_0 \cos(\omega t - \mathbf{kz} + \phi) \tag{2.1}$$

where E_0 is the electric field magnitude, ϕ is the constant phase shift, ω is the angular frequency and k is the wave vector or spatial frequency along propagation direction, z. The resolution represents a travelling wave propagating at velocity v along the z-direction. For many applications, pulsed laser sources are utilised to enable fast processes in physics, chemistry and biological studies [1, 3]. This quest has pushed researchers to design and develop ultra-short laser pulses with high energy concentrated in a very short duration. An ultra-short electromagnetic wave, $G(t)$ can be mathematically denoted as the product of plane wave approximation and time-dependent envelope $A(t)$.

$$G(z,t) = A(t) E_0 e^{i(\omega t - kz + \phi)} \tag{2.2}$$

Since mode locked lasers typically have a Gaussian distribution of optical power versus time, the ultrashort optical pulse with a Gaussian envelope can be modelled as:

$$A(t) = Ae^{-\Gamma t^2} \tag{2.3}$$

Where the envelope is given by a Gaussian function $e^{-\Gamma t^2}$ and Γ can be complex.

$$\Gamma = \Gamma_1 + i\Gamma_2 \tag{2.4}$$

Γ_1 is related to the pulse duration τ, and the complex term determines the time-dependent phase shift $\Phi(t)$ from which the time-dependent frequency $\omega(t)$ can be retrieved.

$$\tau = \sqrt{\frac{2\ln 2}{\Gamma_1}} \tag{2.5}$$

$$\omega(t) = \frac{d\Phi(t)}{dt} = \omega_0 + 2\Gamma_2 t \tag{2.6}$$

The generation of ultra-short optical pulses in our lab is achieved using a commercial mode locked laser. Ultrashort ~ 800 fs temporal duration and a bit rate of 50 MHz are generated. Mode locking (ML) is an optics concept wherein a laser can be made to produce intense and short pulses of light. A fixed phase relationship is established between the various longitudinal modes within the laser cavity, constructive interference between these modes leads to a laser pulse train.

A fixed phase relationship between the various longitudinal modes can be established by placing an optical device exhibiting intensity dependent transmission in the laser resonator such as a saturable absorber or an active device such as an Acousto Optic Tunable Filter (AOTF). A saturable absorber is formed by doping absorber ions into a lossy medium in order to reduce high-energy photon absorption [4, 5]. The intrinsic properties of the saturable absorber to absorb low intensity and transmit high intensities leads to amplification of the high-intensity signal when the process repeats after bouncing back and forth within the laser resonator. Figure 2.2 depicts the mode locking mechanism, interference between longitudinal modes within laser cavity results in an ultrashort coherent pulse train. The optical bandwidth is determined by the laser gain medium and round trip time within the cavity determines the laser bit rate.

In addition, the Fourier transform theory [2] establishes that a continuous wave signal has an infinite extent in time but has a limited bandwidth in the spectral domain, whereas a time-limited pulse has a broad spectral bandwidth.

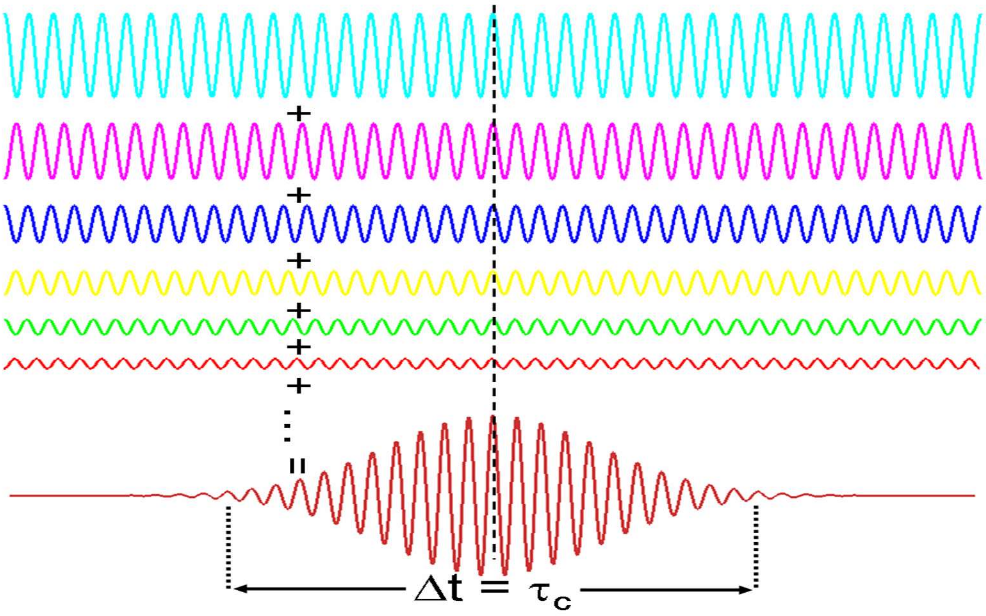

Figure 2.2 Mode-Locking Principle. Constructive interference between laser modes inside the laser cavity with a fixed phase relationship leads to the generation of a coherent ultrashort pulse burst with high peak power, gain bandwidth determined by the laser gain medium and pulse repetition rate determined by the optical round trip time within the laser resonator

Assuming pulse emitted from a laser has a Gaussian profile, *A(t)*, and its Fourier transform *G(ω)* can be simplified mathematically and denoted as follows:

$$A(t) = A.\exp(-\frac{t^2}{2\tau^2}) \quad (2.7\ (a))$$

$$G(\omega) = \tau\sqrt{2\pi}A.\exp(\frac{-\tau^2\omega^2}{2}) \quad (2.7\ (b))$$

where *A* denotes the pulse amplitude, and τ denotes the Full-width Half maximum of the Gaussian pulse. The time bandwidth product uncertainty [6, 7] implies that there is a limit to the minimum bandwidth achieved for a given pulse duration. The minimum temporal duration that can be achieved for a given bandwidth is called a transform limited pulse. A transform limited has constant spectral phase.

The Sellmeier equation [8] plays a fundamental role in the propagation of a broadband signal in a material medium, as different spectral components travel at different velocities, v denoted as follows;

$$v = \frac{c}{\eta(w)} \tag{2.8}$$

Propagation through a dispersive medium of length z leads to the signal picking up a phase factor $\psi(z) = k(w)z$ denoted by:

$$G(z,\omega) = G(\omega).\exp(ik(\omega)z) \tag{2.9}$$

Where *k(w)* is propagation constant of the dispersive medium. Similarly, the dispersion relation denoted by expanding the propagation constant, *k(w)* in a Taylor series around the central optical frequency can be mathematically described as follows [9 - 11]:

$$k(w) = \eta(w)\frac{w}{c} = k_o + k_1(w - w_o) + \frac{1}{2}k_2(w - w_o)^2 + \frac{1}{6}k_3(w - w_o)^3 .... \tag{2.10}$$

The parameters k_1 and k_2 are related to the refractive index η and its derivatives through the relations;

$$k_1 = \frac{1}{v_g} = \frac{1}{c}\left(\eta + w\frac{d\eta}{dw}\right) = \frac{1}{c}\left(\eta - \lambda\frac{d\eta}{d\lambda}\right) \tag{2.11}$$

$$k_2 = \frac{dk_1}{d\omega} = \frac{1}{c}\left(2\frac{d\eta}{dw}\eta + w\frac{d^2\eta}{dw^2}\right) \tag{2.12}$$

Where n_g is the group index, and v_g is the group velocity. k_o denotes the phase shift upon the optical carrier. k_1 generates time delay upon the propagating envelope and k_2 is responsible for amplitude reduction and spread of the envelope profile. The rate that changes in amplitude or envelope of the wave propagates is group velocity, v_g.

$$v_g = c\left(\eta - \lambda\frac{d\eta}{d\lambda}\right)^{-1} \tag{2.13}$$

A more often description of dispersion parameter *D* is established in terms of *ps/nm.km*. For a frequency component of *ω* in a broadband pulse, the propagation time, $\Delta\tau$ through a dispersive medium with a dominant first order propagation constant $k_2(\omega)$, length of *L* is $L/v_g(\omega)$, the difference of propagation time between *ω* and ω_0, is expressed as

$$\Delta\tau(\omega) = \tau(\omega) - \tau(\omega_o) = k_2(\omega - \omega_o)L = \left(2\frac{d\eta}{d\omega} + \omega\frac{d^2\eta}{d\omega^2}\right)\frac{(\omega-\omega_o)L}{c} \tag{2.14}$$

By substituting equation (2.13) to equation (2.14), the difference of propagation time between *ω* and ω_0, is rewritten as

$$\Delta\tau(\omega) = \frac{\lambda^3 L(\omega-\omega_0)}{2\pi c^2}\frac{d^2 n}{d\lambda^2} \tag{2.15}$$

In fiber optics, the frequency is usually substituted by wavelength, the wavelength offset $\Delta\lambda = \lambda - \lambda_0$. Thus time delay in terms of optical wavelength is denoted as:

$$\Delta\tau(\lambda) = \frac{-2\pi c k_2 \Delta\lambda L}{\lambda^2} = D\Delta\lambda L \tag{2.16}$$

where *D* is the dispersion parameter with units of *ps/(nm*km)*, which is defined as

$$D = \frac{-2\pi c k_2}{\lambda^2} = \frac{-\lambda}{c}\frac{d^2 n}{d\lambda^2} \tag{2.17}$$

The Group Velocity Dispersion (GVD), $\ddot{\Phi}$ in ps^2 determines the consequent pulse spread in time after passing through a dispersive element. GVD can be mathematically derived as follows

$$\ddot{\Phi}(v) = \frac{d\tau(v)}{dv} = 2\pi\frac{d\tau(\omega)}{d\omega} = 2\pi k_2(\omega) \tag{2.18}$$

The temporal progression of the pulse can be obtained by obtaining an inverse Fourier transform of the spectrum, *G(z, w)*.

$$G(z,t) = G_o e^{-a(z)\left(t - \frac{a_o}{v_g}\right)^2} e^{-i\omega\left(t - \frac{z}{v_{ph}}\right)} \qquad (2.19)$$

Where;

$$\frac{1}{a(z)} = \frac{1}{a_o} - 2ik_2(w_o)z \qquad (2.20)$$

Consequently, pulse shape is determined by real and imaginary parts of *a(z)*

$$a_R(z) = \frac{a_o}{1 + 4a_o^2 k_2(w_o)^2 z^2} \qquad (2.21)$$

$$a_{\mathrm{Im}}(z) = \frac{2a_o^2 k_2(w_o)z}{1 + 4a_o^2 k_2(w_o)^2 z^2} \qquad (2.22)$$

A pulse propagating through a dispersive medium will broaden based on the Group velocity dispersion parameter, k_2. The higher order propagation constants obtained by Taylor expansion of *k(w)* determine the chirp induced onto the propagating optical pulse. The imaginary part of *a(z)* introduces quadratic temporal phase upon transform limited pulse travelling along the dispersive medium [12]. A transform-limited pulse as defined is an optical pulse of minimum possible duration for a given spectrum and thus minimum time bandwidth product possible. An ultrashort pulse will conform the frequency-to-time mapping if its transform limited and the dispersion introduced is much greater than the pulse duration.

2.2 Photonic Time-Stretch

2.2.1. Mathematical Proof

Ultra-short optical pulses spread by linear propagation in a dispersive medium due to the fact that each harmonic travels at a frequency dependent phase velocity. Dispersion is the dependence of phase and or group velocity on frequency. The result of ultra-short pulse propagation through a dispersive medium is a difference in arrival time of individual spectral components [9 – 18]. In a normally dispersive medium, the low harmonic components travel faster, and high-frequency components move slower causing the signal to be positively chirped, whereas in an anomalously dispersive medium, high-frequency components travel quicker and low-frequency components travel slower leading to negative chirp in the signal. Frequency-to-time mapping principle establishes that once sufficient dispersion has been introduced onto an ultra-short pulse, its temporal profile becomes a scaled replica of the optical spectrum [13 - 15]. A broadband signal comprising a band of frequencies will spread in time as every spectral component arrives at a different moment in time.

Assume a transform-limited Gaussian pulse with a temporal profile denoted by *g(t)* and pulse width t' propagating through a dispersive medium $\ddot{\Phi}$ (ps^2). The frequency to time mapping phenomena based on the far-field Fraunhofer criterion [16] can be mathematically denoted as;

$$y(t) = g(t) * e^{\left(i\frac{t^2}{2\ddot{\Phi}}\right)} \tag{2.23}$$

$$= \int g(\tau) \times e^{i\frac{\left(t-t'\right)^2}{2\ddot{\Phi}}}\, dt'$$

Far-field Fraunhofer criterion requires phase variation within the temporal duration of input waveform be much less than a tolerable value; and the square of pulse width to be significantly shorter as compared to system dispersion [17, 18]:

$$\frac{t'^2}{2\ddot{\Phi}} << 1$$

Leading to;

$$y(t) = e^{\left(\frac{it^2}{2\ddot{\Phi}}\right)} \times \int g(t') \times e^{\left(-\frac{it}{\ddot{\Phi}}t'\right)} d\tau \tag{2.24}$$

$$= e^{\left(i\frac{t^2}{2\ddot{\Phi}}\right)} \times G(\omega)\Big|_{\omega=\frac{t}{\ddot{\Phi}}}$$

Thus, output temporal waveform can be approximated to be a scaled replica of the input power spectrum [15].

2.2.2. Principle

Fraunhofer diffraction equation is used to model the diffraction of waves when diffracting pattern is viewed at a long distance from the diffracting object also when it is viewed at the focal plane of an imaging lens. The temporal signal at the output of a dispersive element is the Fourier transform of the temporal signal at the input of the dispersive element [14 – 18]. A unique one-to-one frequency-to-time mapping is achieved. Figure 2.3 depicts an illustration to provide an intuitive description of the far-field Fraunhofer criterion mapping the power spectral density at the input of a dispersive element to its temporal profile at the output, also known as photonic time-stretch. Fresnel diffraction equation governs diffraction pattern created near the object in the near field [19].

The principle of frequency to time mapping is utilised for photonic generation of microwaves and MM-Waves. Similarly, it is also employed in applications requiring slowing down of the waveform enabling digitisation and signal processing in real-time.

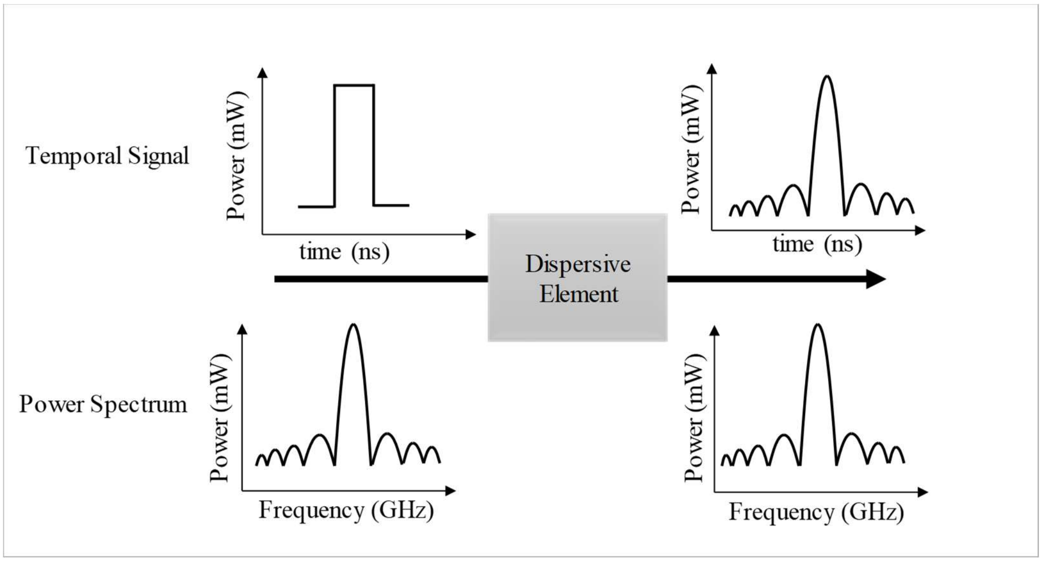

Figure 2.3 The principle of Photonic Time-Stretch is depicted. A realisation of the Fraunhofer criterion enabling unique one-to-one frequency-to-time mapping after propagation of an ultrashort pulse through a highly dispersive medium acting as a real-time Dispersive Fourier Transformer is illustrated. An ultrashort rectangular pulse with a sinc spectrum when propagates through a highly dispersive medium, a sinc profile in time domain is observed at the output of dispersive element.

Strict Fraunhofer condition restricts the complexity of the generated waveform. State-of-the-art research has also focussed on achieving FTM utilising significantly lower dispersion amount. The antennae designer formula relaxes the dispersion condition as follows [14, 19, 20];

$$D > \frac{\tau}{\pi} \tag{2.25}$$

In addition to the coherent frequency to time mapping, incoherent frequency to time mapping has also been achieved. Coherent systems require carrier phase information at the receiver, and they use matched filters to detect and decide what data was sent while non-coherent systems do not need carrier phase information and use methods like the square law to recover the data. As demonstrated in reference [21], an incoherent broadband signal is used as the source. Spectral components of the light are entirely uncorrelated. An external modulator with pulse gate longer than source coherence time enables the spectral components to become partially correlated without significant modification to the amplitude spectral profile. Later, after stretching the pulse in a DE, incoherent FTM maps synthesised energy spectrum of the light source to its averaged intensity profile. This technique also offers flexibility in the electrical tuning of generated waveform's repetition rate. The optical spectrum of the incoherent source is broader and flatter than a coherent source, thus helpful for spectral shaping and lower dispersion required for realising incoherent crossed FTM.

2.2.3. Anamorphic Stretch Transform

Using optical dispersive elements with a linear group delay results in signals with basically the same Time-Bandwidth-Product (TBWP). Linear group delay compresses bandwidth and expands temporal profile. Using specially designed nonlinear group delay elements, one can engineer the obtained TBWP [7, 22]. Non-linear group delay can result in bandwidth compression without a significant increase in recorded length. Anamorphic Stretch Transform (AST) enables selective stretching and warping of a signal. Similarly, TBWP expansion can be obtained depending on signal sparsity and proper choice of warped GD profile using AST. Thus, warped Time-Stretch DFT can be used to either compress or expand the TBWP of analogue signals. Signals with different spectral shapes would require different group delay profiles in order to stretch or compress accordingly. The concept has also been extended to attain data compression by reshaping signals before sampling and selectively stretching sharp features in the data to allow them to be captured at a lower sampling rate.

2.2.4. Short Time Fourier Transform

The ability of photonic Time-Stretch enabled wavelength to time mapping allows temporal domain analysis of signals with spectral features containing useful information content translated to time. Thus, signal post-processing requires reading instantaneous frequency profile along the temporal duration of the signal. The change in frequency at time instant '*t*' that can be further mapped to spatial location based on linear wavelength to time mapping as a result of the dispersive Fourier transformation principle.

Short Time Fourier Transformation (STFT) and spectrogram are used to analyse the frequency content of a signal when that frequency content varies with time. Utilising energy changes over time and frequency extraction tools many applications pertaining to speech analysis, music, seismology and neural network activity have already been implemented [23]. The basic concept of signal processing stems from Fourier series and Fourier transform theorem that allows analysing a temporal signal's frequency content and vice versa a spectral profile can be mapped to its corresponding temporal domain.

STFT principle decomposes a signal into segments, window those out from the rest of the signal and apply Fourier Transform (FT) to windowed signal section. The result will return DFT coefficients as a function of time and frequency. Each FT provides the spectral information of a separate time-segment of the signal, providing simultaneous time and frequency information. Spectrogram is defined as magnitude square of STFT. Assume we have a discrete signal *x[n]* and we want to obtain the frequency information for the signal with respect to time. The entire signal is sliced using a window segment *w[n]* and each windowed segment Fourier transformed. The STFT, which is a modified version of the Discrete Fourier Transform can be represented as:

$$x[t,\lambda] = \sum_{n=-\infty}^{\infty} x[n]w[n+m]e^{-i\lambda m} \qquad (2.26)$$

Where *w[n+m]* is the sliding window function of length *N*. Sampling λ at $\lambda_k = \frac{2\pi k}{N}$

$$x[t,\lambda] = \sum_{n=-\infty}^{\infty} x[n]w[n+m]e^{-i\frac{2\pi k}{N}m} \tag{2.27}$$

A limitation of implementing STFT analysis is that the window section length trades temporal resolution for frequency resolution. As window length increases, a more extended section of time is used; thus an increased segment length, consequently not able to see details that change in time as well but as window length increases we get better frequency resolution. Conversely, a short window implies dividing the signal into many small chunks leading to the precise location of transitions. But a short window results in fewer DFT points and ultimately lower frequency resolution. Thus, an arbitrary resolution in both time and frequency is impossible to achieve as a consequence of the uncertainty principle.

2.3 Photonic Time-Stretch Enabled Microwave and MM-Wave Generation

Various scientific applications benefit from pulse shaping and arbitrary waveform generation [24, 25]. In RADAR, signal processing, communications, and control applications, the ability to customise a signal is beneficial since an input signal can be optimised for better system performance as well as specified to simulate an arbitrary real-world signal [26]. A summary of various Photonics-based microwave and MM-Wave generation schemes based on both CW and pulsed laser sources is presented in the table below

Table 2.1: Comparison of various photonic microwave generation schemes

Photonic Generation Scheme	Advantages	Disadvantages	Frequency Generated	Fibre or Free space solution
Liquid Crystal based Spatial Light Moduator	Accuracy and good stability	Bulky, expense, slow refresh rate	10 ~ 40 GHz	Free space
Optical Heterodyne Photomixing	Fairly good tunability, stability and flexibility	Fairly complex, OIL and OPLL required	< 70 GHz	Fibre based

External modulation	Good tunability and excellent stability	No improvement in TBWP of generated microwave signal	< 70 GHz	Fibre based
FBG based	FBG used for both spectral shaping and WTM; enhanced integration	Lower reconfigurability as system response is fixed	< 70 GHz	Fibre based
Optoelectronic oscillator	Good tunability and minimum phase noise	Slightly complex	< 70 GHz	Fibre based

2.3.1. Spectral Shaping and Wavelength to Time Mapping

An optical method that makes use of photonic Time-Stretch principle for arbitrary microwave generation consists of a broadband signal comprising of a band of frequencies to be spectrally shaped in a spectral filter such as a Spatial Light Modulator (SLM). An input optical signal is diffracted in space and the individual spectral lines directed towards an array of liquid crystal modulators as shown in Figure 2.4. SLM consists of an array of nematic liquid crystals [3, 24]. Applied electric field modifies the properties of the liquid crystal. In the absence of an electric field, the molecules within the crystal are arranged with their long axis along the y-axis. Light polarised along the y-axis will observe a larger refractive index with respect to x-polarised light. Thus, the phase of y polarised light is changed via electric field control. Using a 45° polariser SLM can also be employed for amplitude shaping when accompanying phase change can be ignored. Incoming linearly polarised light is split in 2, each beam suffering different phase retardation [27, 28]. A polariser removing one of the polarisation states leads to amplitude modulation.

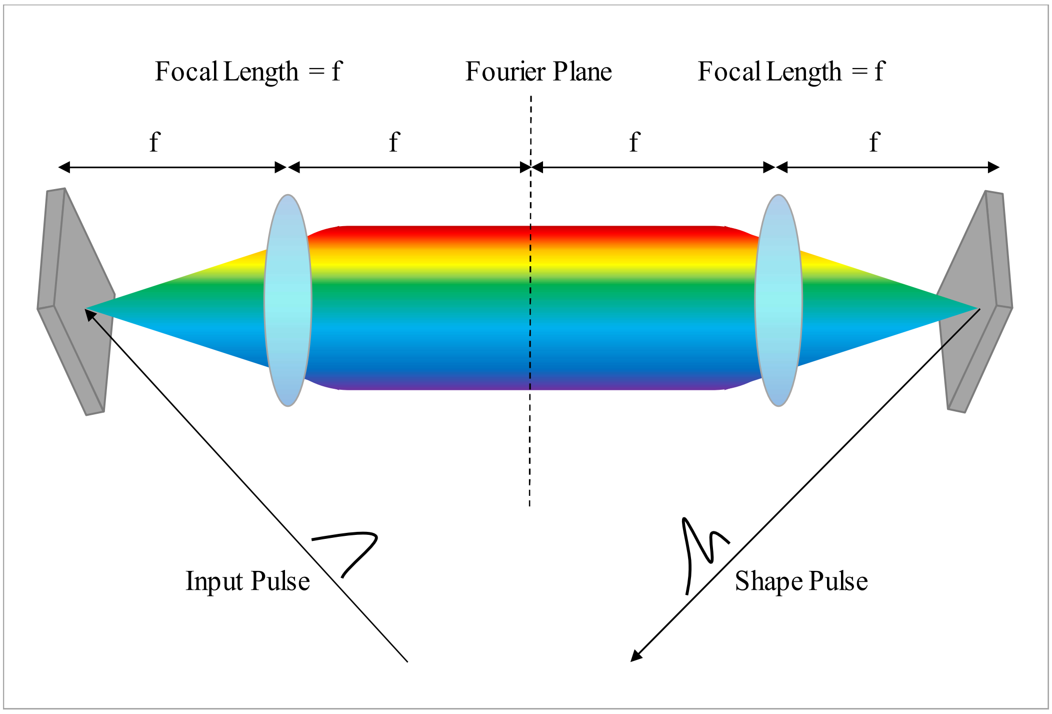

Figure 2.4 Liquid Crystal Spatial Light Modulator (SLM) in Fourier plane enabling spectral shaping of an ultrashort broadband optical pulse [3, 28]. The individual spectral components diffracted in space are amplitude or phase modulated by an applied voltage.

An electrical voltage applied to the liquid crystal array modulates the amplitude and or phase of the individual spectral components incident. The modulated spectral lines are recombined, and the spectrally shaped signal can be further on mapped to time using a dispersive element such as an optical fibre or Fibre Bragg Grating (FBG) obtaining the arbitrary microwave and MM-Wave signal after photodetection [29]. Tailoring the output profile of a signal can be used as a mock input signal for evaluating accurate system response as well as set to imitate real-world complex signals. Such signals have large applications in radio engineering, signal processing, and control electronics [27, 28]. The primary requirement for a line by line spectral shaping is a high enough spectral resolution to distinctly separate adjacent spectral lines.

The concept of frequency to time mapping also known as photonic Time-Stretch has been mathematically elaborated in the preceding section. The terms photonic Time-Stretch, dispersive Fourier transform, wavelength–to–time mapping and frequency-to-time mapping will be used interchangeably throughout this thesis. The photonic Time-Stretch property enables a dispersive element to translate the spectrum of an ultra-short pulse to a replica of its temporal intensity profile upon propagation through it [13 – 15]. Figure 2.5 below depicts the generation of arbitrary high-frequency microwave pulses concept based on spectrum shaping and wavelength to time mapping.

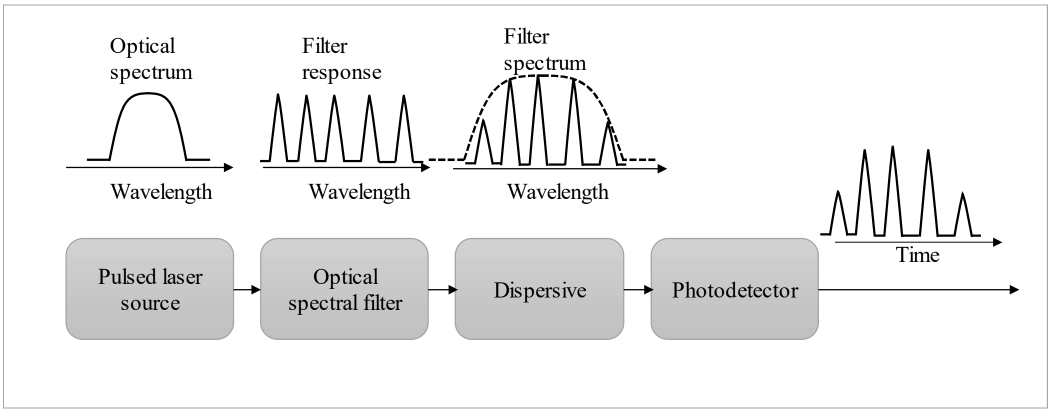

Figure 2.5 Arbitrary waveform generation concept based on Spectral shaping and Dispersive Fourier Transformation [29].

Photonic generation of RF and microwave signals based on pulse shaping and FTM has been pursued intensively [16 – 20]. Though, the problem associated with liquid crystal based spectral shaping technique is that SLM's are bulky and expensive. The refresh rate, which refers to the real-time ability of the liquid crystal modulator to switch the amplitude and phase modulation parameters upon individual spectral lines is also limited to the characteristic properties of the crystal used for optical signal modulation.

In addition, the spectral response is fixed and cannot be altered once implemented. Besides fibre to free space and free space to fibre coupling would introduce a high amount of loss as well. Thus, an inherent limitation of spectral shaping and wavelength to time mapping arise from the spectral shaping capability and the bandwidth of the optical to electrical converter such as a photodetector [28]. Various other spectral shaping schemes including direct space to time pulse shaping and arrayed waveguides have been utilised.

Chip-level optical pulse shaper has also been proposed and implemented [30, 31]. In one scheme, a spectral shaper with an MZI geometry with multiple microring resonators are cascaded. Ability to customise the radii of the micro-rings allows spectral control of pulse shape. The output waveform is tailored to reflect an increasing/decreasing FSR. A key advantage of the technique is the design and configuration flexibility. Each ring will selectively transfer the optical power at its resonance wavelength [26].

Similarly, Fibre Bragg Gratings and Chirped Fibre Bragg Gratings can be employed for spectral shaping and photonic time-stretch applications. Chirped Fibre Bragg gratings exhibit a characteristic linear group delay response, allowing them to act as a dispersive element and achieve wavelength-to-time mapping upon an ultrashort pulse. Their spectral response can also be tailored to attain spectral shaping [32, 33]; one approach obtains spectral shaping by infusing a 3 dB coupler to the terminals of a chirped fibre Bragg grating to create a Sagnac loop mirror. A tunable delay line in the fibre loop helps tune both the central frequency of the generated microwave pulse and the output chirp profile [34]. The configuration attains both spectral shaping of incoming optical pulse and dispersive Fourier transformation based on the gratings dispersion characteristics.

Tailoring spectral profile of optical signal has also been achieved by superposing chirped fibre Bragg gratings with different chirp rates. The overlapping of CFBG's is engineered such that a Fabry-Perot cavity length linearly depending on resonance wavelength, ensuing in a spectral profile with an increasing or decreasing Free Spectral Range [35] carved out. Dispersion induced frequency to time mapping translates the FSR to its corresponding temporal pattern. To generate pulses with a large TBWP, a large 2nd order dispersion is required. However, higher order dispersion would lead to unexpected ripples [17, 18]. Dominant higher order dispersion coefficients of $k(\omega)$ will skew the linear frequency-to-time mapping

An alternative approach to generating high-frequency MM-Wave pulses is based on frequency up-conversion of low-frequency microwave signals wherein a low frequency signal modulated onto an optical carrier can be manipulated to yield a high frequency signal at the photodetector [36]. The critical advantage of photonic microwave generation based on a pulsed source such as a mode-locked laser relative to continuous wave source is that high-frequency microwave pulses and MM-Wave pulse are generated at an ultra-fast rate dictated by the bit rate of the laser.

2.3.2. Temporal Pulse Shaping

Photonic-assisted tunable microwave frequency up-conversion has been achieved using unbalanced temporal pulse shaping (UB-TPS) technique as well [37], wherein a low-frequency microwave signal is firstly modulated on a pre-chirped optical pulse and then compressed by unbalanced dispersion compensation. An advantage of the underlying technique is the up-conversion of a slow microwave drive signal and high-frequency microwave or MM-Wave pulses repeating themselves as dictated by the bit rate of the laser in addition to the improved temporal resolution provided time domain spectral shaping. One disadvantage of this frequency up-conversion method is that the frequency multiplication ratio is limited and Time-Bandwidth product (TBWP) of the generated MM-Wave pulses cannot be improved. To solve this problem, I have improvised upon the existing UBTPS scheme by cascading two modulators in cascade and both biased at the minimum transmission point. An illustration of the proposed concept is presented in Chapter 5. An enhanced frequency multiplication factor has been obtained, and the technique has also been demonstrated to generate chirped MM-Wave pulses by driving the Mach Zehnder modulator (MZM) by a chirped low-frequency RF signal, wherein the chirp in the microwave source is translated to chirp in the generated microwave signal. An improved Time-Bandwidth product is also obtained.

In this thesis, a microwave and MM-Wave generation scheme based on temporal interferometry and unbalanced dispersion has also been implemented, and the generated microwave and MM-Wave signal is applied to physical strain sensing along the length of a chirped fibre Bragg grating. Non-destructive testing and surface profiling of IR transparent glass slides based on the principle of coherence tomography has also been achieved.

2.4 Microwave and MM-Wave interferometry

According to Fourier theory, the spectrum of a Gaussian source is a Gaussian distribution as well. However, the spectrum of a Gaussian pulse train has a spectral interference pattern with its FSR determined by the time delay between consecutive pulses. Utilising the photonic Time-Stretch principle, the FSR can be mapped to its corresponding microwave and MM-Wave pulse after photodetection. Higher order dispersion can be introduced to add chirp to the generated microwave and MM-Wave signal.

Figure 2.6 indicates that the FFT of a Gaussian pulse results in a Gaussian spectrum. Similarly, FFT of a Gaussian pulse train separated by a time interval στ results in a Gaussian envelope with an interference spectrum. The temporal separation determines the Free spectral range (FSR). FSR in interference spectrum in terms of optical wavelength can be calculated as $\Delta\lambda = \frac{\lambda^2}{2c\sigma\tau}$.

The far-field Fraunhofer criterion establishes the dispersion required to map the spectral intensity profile to its temporal analogue. Thus, the interference spectrum of a Gaussian pulse train can be mapped to a temporal intensity signal after passing through a dispersive element acting as a real-time Fourier transformer. The output signal can be analysed via photodetection.

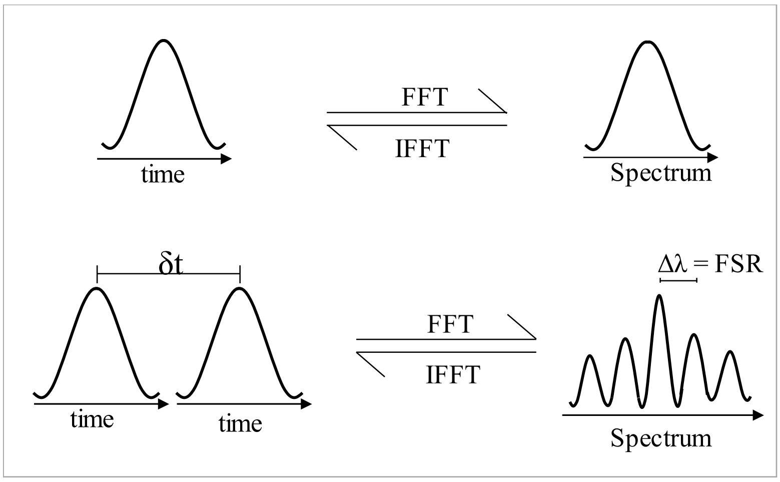

Figure 2.6 Time and Spectrum relationship for a Gaussian laser source. The first row denotes the time spectrum relationship for a single Gaussian pulse, the second row denotes the time frequency relationship for two consecutive Gaussian pulses separated by a time interval.

Thus, optical interference can be translated to an electrical waveform with its central frequency determined by the temporal separation between pulses and overall system dispersion. Thanks to the dispersion-induced wavelength-to-time mapping, this interference spectrum is converted to a temporal interference pattern with its period given by $\Delta t = \Delta\lambda * \ddot{\Phi}$. Figure 2.7 depicts a translation of spectral interference pattern to its temporal analogue after passing through a dispersive element.

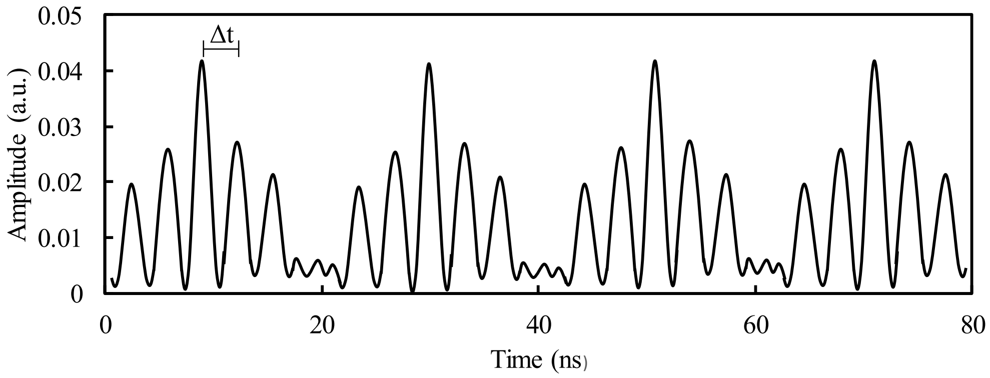

Figure 2.7 The spectral interference mirrored to temporal interference pattern for five successive pulses leading to microwave and MM-Wave carrier frequency determined by the optical time delay and system dispersion.

Similarly, dividing a Gaussian pulse signal into two arms so as to introduce a time delay between the two signals, and allowing both pulses to stretch differentially before interference would also result in a signal with frequency chirp. The dispersion imbalance determines the chirp rate. A demonstration of the underlying technology is presented in Chapter 5 for developing a unique frequency swept, high throughput MM-Wave source.

Also, the concept of optical interferometry enabling microwave and MM-Wave generation can also be extended to interferometry in the MM-Wave region itself. The ability of interference to measure distances with utmost precision allows exploring MM-Wave interferometry capable of resolving distances within MM-Wave range. An ultrafast swept source could benefit from high depth resolution due to large bandwidth capability, high A-scan rate per sec that depends on the chirp rate of the source. Photonics-based MM-Wave swept source could allow for high throughput, high precision swept source MM-Wave coherence tomography. Figure 2.8 depicts the proposed setup for utilizing a photonics-based chirped MM-Wave generation scheme as a potential source for MM-Wave coherence tomography.

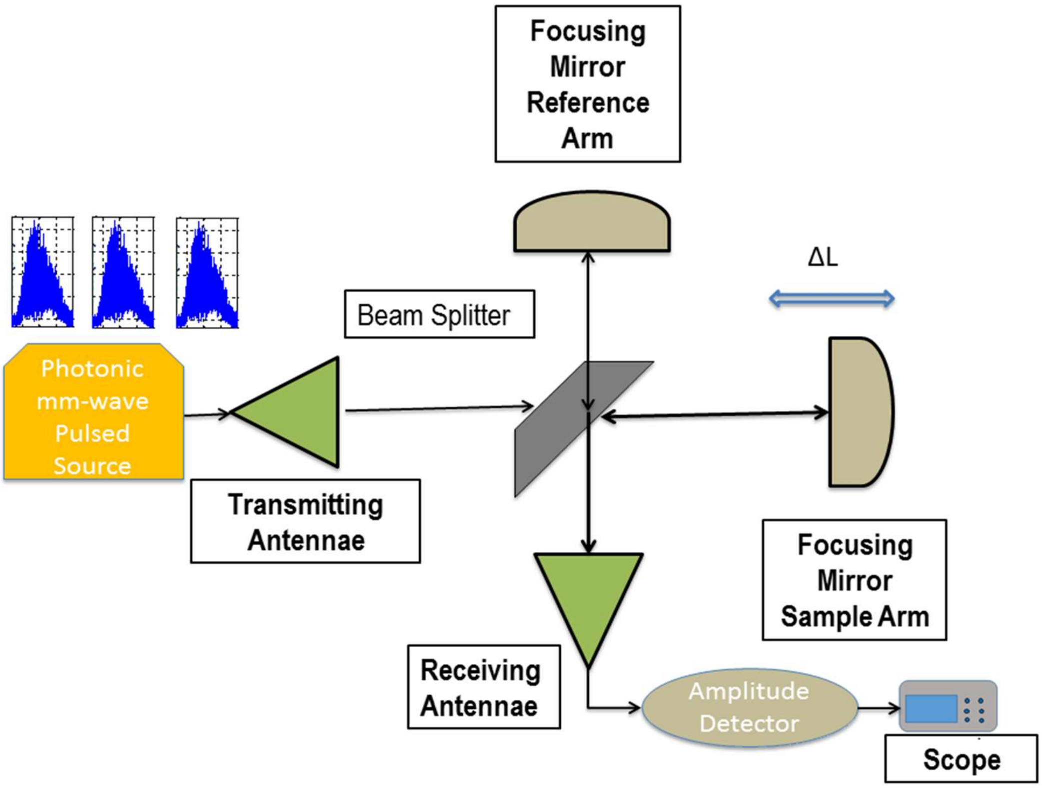

Figure 2.8 Schematic of proposed Michelson Interferometer Structure Employed for high throughput photonics-based chirped MM-Wave Coherence Tomography.

MM-Waves from a Photonics-based chirped MM-Wave source can be directed onto a beam splitter, dividing the incident beam to be investigated into two beams. One beam is reflected back onto itself by a fixed mirror, a mirror also reflects the other one but the beam travelling a reference path can be adjusted to obtain a variable path length and thus time delay. MM-Waves reflected from the specimen and reference beam are combined at a detector, and the interference between the two beams is measured. When the optical path length of the reference arm is tuned, different delays of backscattered light from within the sample can be mocked yielding depth-dependent information. Following an axial sweep, the incident beam is scanned in the transverse direction, and multiple axial measurements are performed.

Superposition of the source signal divided into two beams $I_1(t)$ and $I_2(t)$ at the output expressed as a function of the average intensity I_0:

$$I = I_0\{1 + \cos(k(l_1 - l_2))\} \tag{2.28}$$

Where l_1-l_2 denotes the path length difference yielding a depth-dependent Free Spectral Range (FSR) for a given sweep bandwidth. Further on, the Wiener Khinchin theorem establishes a Fourier transform relationship between the coherence function and the Power Spectral Density of the source. The experiment demonstrated in Chapter 5 is based on the concept of swept source frequency domain Coherence Tomography (CT) setup recording Interference signal as a measure of wavelength. In such a configuration the reference arm can be fixed as depth information can be deciphered by a Fourier transform of the light spectrum at the output of a Michelson interferometer since a given phase difference generates a unique Wavelength-dependent signature of phase differences. Fourier domain CT has the advantage of higher sensitivity and non-mechanical A-scan recording relative to Time Domain Coherence Tomography. Similarly, swept source Coherence tomography refers to a Coherence Tomography setup wherein source is rapidly tunable allowing depth information to be encoded in the spectral interference pattern that can be recorded using an MM-Wave envelope detector.

2.5 Non-Contact Measurement: Existing Methodologies and Critical Review

The concept of non-contact sensing has applications in a vast number of scientific disciplines including medicine, pharmacy, engineering (mechanical, civil, aeronautical, and electrical systems) [38 – 43]. The penetration, reflection and transmission properties of acoustic and electromagnetic waves interacting with matter have been exploited for several decades. Based on the wave-matter interaction, various mathematical operations can be employed to retrieve differences between the incident and reflected/transmitted beam and the change in signal behaviour related to determining characteristic properties of the material under test and also locate any subsurface anomaly or defect that may form over a period of time or due to error while manufacturing. Figure 2.9 classifies the various methodologies employed in the field of industrial engineering incorporating Non-Destructive Testing (NDT) applications. The terms Non Destructive Testing (NDT, non-contact sensing and Non Destructive Evaluation (NDE) are used interchangeably. In this section, different noncontact optical and electromagnetic procedures that can be utilized to quantify distances to objects, and related parameters, for example, object thickness, surface profiles, speeds and vibrations are analysed.

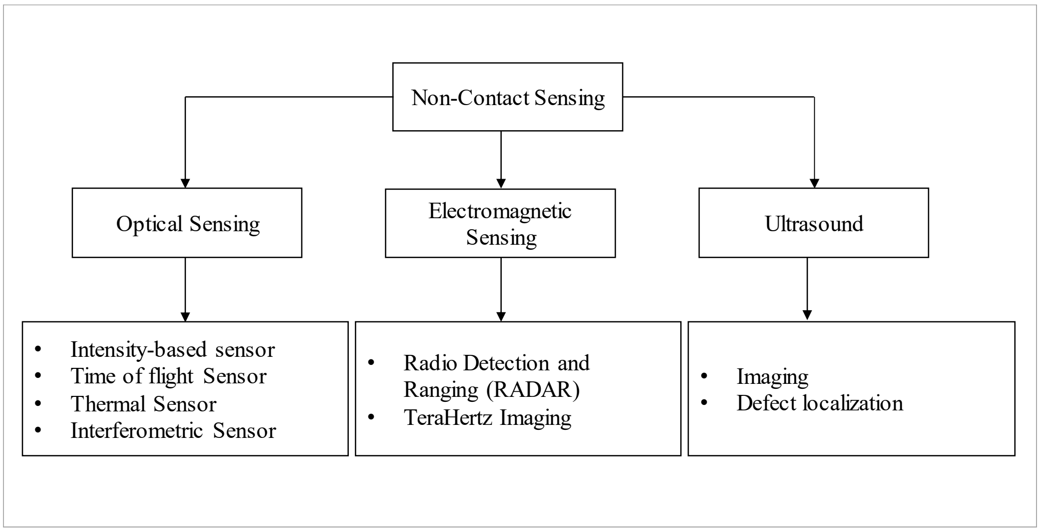

Figure 2.9 Classification of NDT or Non-Contact Measurement techniques within three general Non-Contact measurement methodologies employed over the years.

2.5.1. Optical Sensing

High precision and accuracy are a requirement for optical non-contact sensing. Industrial quality assurance practices rely on fast scanning dimensional metrology and surface inspection techniques. Intensity-based sensors measure the distance dependent intensity loss incident towards a sample under test. However, a limitation of the technique arises from the fact that any intensity dependent loss would be interpreted as an optical path length difference. The technique is also more suitable for short distance ranging. Long distance ranging can be done using the well-known time-of-flight method wherein the time taken for incident optical pulse reflected from object under test to reach the sensor is calculated [40 – 42].

An optical non-contact sensing that achieves sub wavelength displacements of an object is based on interferometry. The coherence of two waves follows from how well correlated the waves are as quantified by their cross-correlation function. Two waves are said to be coherent if they have a constant relative phase difference. Spatial coherence describes the correlation between waves at different points in space and temporal coherence illustrates the relationship between the signal of interest at different moments in time, the ability of the wave to interfere with itself at different moments in time is expressed as temporal coherence. The temporal coherence function or autocorrelation function, where *u(t)* is a stationary complex random function is mathematically denoted as follows:

$$G(\tau) = \int u^*(t)u(t+\tau)dt \tag{2.29}$$

Where $u^*(t)$ is the complex conjugate of *u(t)*. Intensity *I* is peak intensity at *G(0)*. The normalised function *g(τ)* is derived as follows:

$$G(\tau) = \frac{\int u^*(t)u(t+\tau)dt}{\int u^*(t)u(t)dt} \tag{2.30}$$

The coherence time τ_c related to the inverse of the spectral bandwidth and coherence length l_c can be obtained as follows:

$$\tau_c = \int |g(\tau)| d\tau \tag{2.31}$$

$$l_c = c\tau_c \tag{2.32}$$

Further on, the Wiener Khinchin theorem relates power spectral density of source *S(v)* to the autocorrelation function *G(τ)* as follows:

$$S(v) = \int_{-\infty}^{\infty} G(\tau) e^{-i\omega\tau} d\tau \tag{2.33}$$

Interferometry based sensing consists of coherent light from a source directed towards a beam splitter, one of the beams is directed towards the sample whereas the second beam travels a reference path with a known path length and time delay. Back-scattered light from the sample interferes with reflected light from the reflector in the reference arm, and interference signal detected at the output. If the light source is coherent, then interference fringes will be observed as the relative path lengths are varied, however, if low coherence or short pulse light is used then interference fringes will be only observed when the two path lengths are matched to within the coherence length of light. The echo time delay and intensity of back-scattered light from within the sample can be measured and detected by demodulating the interference output while scanning the reference path length [43].

The famous Michelson interferometer is most commonly employed and the technique is known as Optical Coherence Tomography (OCT). An improvement in the actual Optical coherence tomography experiments has been achieved by replacing detector with a low loss spectrometer. Interference signal as a measure of wavelength can be obtained. In such a setup the reference arm can be fixed as depth information can be deciphered by a Fourier transform of the light spectrum at the output of a Michelson interferometer since a given phase difference generates a unique Wavelength-dependent signature of phase differences. Fourier domain OCT has the advantage of higher sensitivity and non-mechanical A-scan recording relative to Time Domain Optical Coherence Tomography. Similarly, swept source OCT refers to an OCT setup wherein source frequency can be rapidly and readily swept allowing depth information to be encoded in the spectral interferogram which can be recorded using a photodetector [43, 44].

Infrared-based sensors can be broadly divided into two categories; thermal and non-thermal [45] sensors. Thermal Infrared (IR) based sensing can be extended to Non Destructive Evaluation techniques to measure subsurface deformation and or contamination. Thermal IR based sensing consists of infrared thermography wherein an object under test is irradiated with uniform thermal energy. And the rate of change of temperature across the surface is monitored. A calibration scheme wherein a perfectly normal surface without any subsurface damage is considered for reference purposes in most cases. Defect location can be obtained by comparing sound sample to a defective sample. An abnormal temperature profile is seen in the region surrounding the defect, which is usually at a different temperature relative to the rest of the material. Various algorithms have been devised locating the size of the defect to a high degree of accuracy as well. Most common materials employed for thermal based IR techniques are composites, solar cells, inspection of welded metal and plastic joints and electronics. Thermal IR based NDE has the advantage of being applied to a wide number of materials for inspection of internal cracks and or defects. However, thermal IR based NDE evaluation suffers from the high-cost price of the system and the need to ascertain a reference sample for comparison.

FTIR Absorption, Reflection and Transmittance Spectroscopy Non-thermal Infrared-based NDE are also popularly implemented using Fourier Transform Infrared (FTIR) Spectroscopy. FTIR spectroscopy is based on the samples chemical nature enabling absorption of the incident IR bandwidth. IR absorption occurs when infrared radiation interacts with a molecule undergoing change in dipole during vibration and when the photon energy is sufficient to allow the transition to an excited energy level. FTIR spectrometers are based on providing a spectral fingerprint specific to the sample under test. Energy as a function of time for all wavelengths is simultaneously recorded. They have found applications in the pharmaceutical industry, identifying chemical composition and or contaminants in oral and injectable solutions, as well as amorphous and solid capsules.

2.5.2. Electromagnetic Sensing

The section of electromagnetic sensing is dedicated to high-frequency microwave, MM-Waves and THz based non-contact sensing schemes employed. MM-Waves are electromagnetic waves that are characterised by wavelength in the 1-10 mm range. They lie between the microwave and infrared regime of the electromagnetic spectrum. Millimetre-wave (MM-Wave) pulses have been widely used for data transmission at high throughput due to their immunity to multipath interference [38, 39].

The ability of MM-Waves to penetrate electrically non-conductive material including wood, paper, fog, dust and fibre composites allows them to be applied in various non-destructive and non-invasive material characterisation and imaging techniques. They are also non-ionizing electromagnetic waves, and no known hazards to human health have been observed. Ordinary gypsum drywall material is very transparent well into the MM-Wave band and plywood, and particle board are also relatively easy to penetrate [46].

Amongst the many applications MM-Waves are utilised for, the most prominent ones are in defence. An important application also known as ACC (Autonomous Cruise Control) has been extensively studied. The ACC Radio Detection and Ranging (RADAR) unit is placed in the front of a car. It sends a pulsed radar signal to measure the front distance. When the distance is too close, the radar sends a warning signal. Military applications include employing MM-Wave signals for a wide range of sensors, tactical surveillance systems as well as for missile seeker and re-control functions. Due to the ability of MM-Wave signals to penetrate cloth, they are also employed for concealed weapons detection at airport security scanners. In addition, MM-Wave signals are also applied in astronomical observations to study the fabric of the cosmos [38, 39, 47]. Molecules in the atmosphere such as ozone, water vapours, oxygen etc. exhibit characteristic spectral band absorption in the MM-Wave range. However, rapid attenuation of MM-Wave signals in free space is a challenge.

High-frequency microwave, millimetre wave and THz range finding and NDE techniques consist of Frequency Modulated Continuous Wave RADAR and Terahertz Time domain and Frequency domain reflection. In the FMCW RADAR scheme, a chirped signal is directed towards a target; the reflected signal is down-converted at the detector by mixing it with a replica of the incident signal. The Doppler frequency is recorded, and target range along with velocity can both be established. Similarly, spectroscopic techniques in the microwave, MM-Wave and THz domain are limited to specific frequency bands due to the limited bandwidth of antennas and beam forming components. While MM-Wave systems penetrate better through some barrier materials compared to THz systems, the spatial resolution favours the latter ones for imaging applications. The spatial resolution depends on bandwidth employed and varies between 0.4 mm and 3 mm [46]. Terahertz detection inherently has a roughly ten times better spatial resolution compared to MM-Wave systems just because the electromagnetic wavelength of THz radiation is approximately ten times shorter than MM-Wave radiation. However, the generation of Terahertz has been a challenging topic, and detection techniques based on electronics along with high atmospheric absorption limited initial research funding into THz physics. Novel techniques, enabling both generation and detection of high-frequency sub-THz waves and THz waves are exploited in this thesis opening the gateway for unique non-destructive evaluation schemes.

The dielectric properties of a material can be investigated by implementing a quasi-optical technique. The sample under test is illuminated with a Gaussian beam. The beam is partially reflected and partially transmitted at the sample interface; the measured information is further processed to extract the characteristic properties of the object, including the complex permittivity, permeability, refractive index and material thickness.

In the microwave and MM-Wave regime, the most commonly applied Non-Destructive Evaluation mechanism implemented is based on measuring scattering parameters (S-parameter) of a sample under test using an MVNA (Microwave

Network Analyser). The S-parameters (S_{ab}) are a measure of the electrical energy propagating through a system with impedance mismatch. The coefficients represent input-output paths determining reflection or transmission characteristics at an interface between transmitting and receiving antennae. Permittivity and permeability as a function of S-parameter can be extracted using the Nicholson-Ross Weir (NRW) algorithm [48]. A method devised to extract geometrical properties of turbid media at the MM-Wave frequency is the NRW method. A Microwave Vector Network Analyser is used to characterise the incident and transmitted MM-Wave spectrum. A system of equations [49] is solved to extract the transmission and reflection coefficient, T and Γ respectively from the S_{11} and S_{21} parameters obtained.

$$\Gamma = K \pm \sqrt{K^2 - 1} \qquad (2.27)$$

The plus or minus sign in the equation is chosen such that $|\Gamma| \leq 1$ and K is calculated as follows:

$$K = \frac{S_{11}^2 - S_{21}^2 + 1}{2S_{11}} \qquad (2.28)$$

The equation can be further simplified to relate the relative permittivity, ε_r, to the reflection coefficient assuming non-magnetic material as follows [50]:

$$\varepsilon_r = (\frac{1-\Gamma}{1+\Gamma})^2 \qquad (2.29)$$

Diffraction limits the resolution of all imaging systems, but it’s particularly important for microwave and MM-Wave and THz systems due to its longer wavelength. The resolution can be optimised by operating in the near field and using large imaging apertures. Coherent detection of the scattered wavefront amplitude and phase is a vital concept of synthetic imaging techniques. Near field planar wideband holographic imaging merges the characteristics of microwave holography with synthetic aperture RADAR (SAR) to form high-resolution fully focussed 3-dimensional imagery [50]. This method directs a diverging wide beam width microwave or MM-Wave beam at the imaging target and scans it over a rectangular planar aperture. The scattered wavefront phase and amplitude or in-phase and quadrature signals are obtained from a receiver scanned along with transmitter. Receiver waveforms are discretely sampled over the frequency sweep. This 3-dimensional data set is then focussed using a Fourier optics based computer image reconstruction algorithm. The algorithm uses 2-D FFT to decompose the scattered wave-front into an equivalent superposition of plane waves that correspond to a range of azimuth and elevation angles. Each of the plane wave components can then be phase shifted or back propagated to the target depth. These data are then interpolated into 3-D spatial frequency space. An inverse 3-D FFT then transforms the data back to the spatial domain. The magnitude of the complex image then yields a real image of the target.

Some other well established and most commonly employed electromagnetic based Non Destructive Evaluation of industrial objects consist of radiographic and X-ray imaging. These techniques though very useful suffer from causing ionization and thus harmful to living cells and tissue analysis and the health and safety of personnel carrying out radiographic based non-destructive testing.

2.5.3. Ultrasound

Ultrasound refers to continuous pressure waves beyond the audible range of 20 Hz-20 kHz. Directing ultrasound waves with a known incident profile towards “turbid media” [51] and analysing the change in amplitude and phase of the signal upon interaction with the object under investigation can be utilised to image within the material medium. In essence, the reflected signal is analysed and the echo time delay is calculated to reveal the depth of the structure. Based on the acoustic impedance of the various layers making up the sample, different depths would reflect signals of different amplitudes and associated time delays. The reflection direction is also an essential parameter as scattering from irregular surfaces leads to only a portion of the incident energy received. Similarly, absorption also plays a significant role as material properties would attenuate the incident ultrasound. The attenuation is also dependent on the incident signal frequency. The term ultrasound, though synonymous with medical imaging and thus internal body imaging, the technique can also be employed to locating subsurface defects within steel, alloy, concrete, wood and composite materials. An axial resolution of 0.5 mm and transversal resolution of 0.4 mm can be achieved [52]. Ultrasound techniques are limited by the fact that a couplant is required to enable transmission into sample under test and thus is not totally contact-free. The technique fails to characterise thin layers and is not very suitable for examining irregularly shaped objects. Irregular objects tend to scatter ultrasound in random directions resulting in interference of the waves with random phases interacting with each other. This results in speckle, which is deemed as noise in imaging applications.

2.5.4. Fiber Bragg Grating Sensing

It is worth mentioning that Fiber Bragg Gratings (FBG) can also be employed for minimally invasive sensing. They can be inscribed into optical fibers and attached or integrated into structures for strain and temperature sensing. A sensing device inherently changes its physical properties in some way to external influences; a processing unit can thereon indicate the physical deviation to a change in the output parameter monitored. Many schemes for fibre optics based sensing [53, 54] have been successfully implemented for decades, a Fibre Bragg Grating is often utilised wherein the Bragg wavelength is monitored to indicate an external influence such as strain or temperature. Simply put, an FBG is a Bragg reflector. Rather than having a uniform refractive index along the core of the fibre, the refractive index can be modified to change periodically along its length. When a broadband spectrum is directed towards an FBG, a specific wavelength of the incident spectrum known as the Bragg wavelength is reflected while transmitting all others thus acting as a notch filter. The Bragg wavelength reflected depends upon the effective refractive index and grating period of the FBG fabricated.

2.5.5. Sensing Scheme Proposed

Coherence tomography has emerged as an effective asset for in-depth imaging of the interior structure of an object non-invasively. THz coherence tomography provides a good combination of resolution and penetration and has recently found practical applications for non-destructive testing (NDT) in medical imaging, material characterisation, sensing, and security systems. However, basic research and advanced technology developments in sub-THz or MM Wave coherence tomography are very limited compared to their well developed counterparts at microwave and optical frequencies resulting in a lack of available fast-sweeping broadband sub-THz sources. This thesis proposes a completely new kind of real-time, high-frequency MM-Wave and THz coherence tomography utilising photonic generation of chirped MM-Wave pulses, empowering high-throughput tomography at a sweep rate of ~50 MHz. The work expands on University of Kent's expertise in photonics and microwaves, (for example, optical coherence tomography, ultrafast optical imaging, photonic generation of microwaves/mm-waves, microwave and MM-Wave engineering), and VUB skill in THz (for instance, spectroscopy, detecting and imaging in the sub-THz regime). A broadband frequency-sweeping sub-THz source is developed at Kent utilizing photonic time-stretch, which is the essential source of a real-time frequency-domain sub-THz coherence tomography framework. In the second stage of the work, VUB allowed the completion of the MM-Wave coherence tomography system by providing a wide range of V-band components and detectors at the sub-THz band [55].

2.6 Summary

A detailed background study on optical devices, techniques and system structures in Photonic Time-Stretch Enabled High Throughput Measurement schemes is presented.

The theoretical connotations that form the base for the research carried out in the next three chapters have been mathematically demonstrated. In addition, ultrashort optical pulse characteristics, the principle of mode locking and the propagation of ultrashort pulses in a dispersive medium are outlined. Similarly, the concept of dispersive Fourier transformation and mapping of the spectral profile to its temporal domain is presented. State-of-the-art Photonics-based microwave and MM-Wave generation schemes are compared. Short Time Fourier Transform (STFT) is employed for post processing of signal obtained. A theoretical understanding of the underlying concept utilised for decoding and demodulating information content in the temporal domain from signals analysed as a result of photonic microwave generation and detection is presented. A comparison of traditional non-destructive testing techniques is also highlighted, and the need for a novel ultrafast time-domain sensing scheme concluded. A comparison of various non-contact sensing schemes is presented in Table 2.2.

Table 2.2: Summary of various Non-Contact Sensing schemes and their characteristics.

	Method	Pros	Cons	Probing Distance	Spatial Resolution	Scan rate
Optical Sensing	Intensity-Based Sensing Time-of-Flight Thermal Sensing Interferometric Sensing	Simplicity, Very accurate, commercially available Long-range and short range applications	Expensive Complex data acquisition	Few mm (OCT) to metre (TOF)	Few nm - µm	Few kHz – 20 MHz [40]
Electromagnetic Sensing	Microwave MM-Wave TeraHertz	Structural Health Monitoring Radio Astronomy Concealed weapons detection	Polarization dependence Spatial resolution dependent on BW	Few mm to 50 metre	0.3 mm to few cm	100 Hz – 1 kHz [46]
Ultrasound	Imaging Time-of-Flight	Biological applications (internal body imaging) Non Destructive Evaluation; Defect localization	Noise Sensitive Skill and training (expensive)	Direct coupling	200 – 800 µm	30 - 100 Hz [52]
FBG Sensing	Time Doman Sensing Spectral Domain Sensing Intensity and Phase-Based Sensing	Multiplexing capability Immunity to EM interference	Minimally invasive; requires contact with surface under inspection	Few mm to km	Few µm to mm	Few Hz – 100 kHz [53]

REFERENCES

[1] C. Rulliere, *Femtosecond Laser Pulses: Princoples and Experiments*, Berlin Heidelberg: Springer, 2013.

[2] G. J. Gbur, *Mathematical Methods for Optical Physics and Engineering*, Cambridge University Press, 2011.

[3] A. M. Weiner, "Femtosecond pulse shaping using spatial light modulators," *Review of Scientific Instruments,* vol. 71, pp. 1929-1960, 2000.

[4] K. Stankov, "Methods of passive and active mode locking using intracavity optical frequency mixing," *Optics Letters*, vol. 14, pp. 51-53, 1989.

[5] A. Schmidt *et al.*, "Passive mode locking of Yb:KLuW using a single-walled carbon nanotube saturable absorber," *Optics Letters*, vol. 33, pp. 729, 2008.

[6] G. Hongbiao, M. H. Asghari and B. Jalali, "Time-bandwidth engineering for arbitrary waveform generation," in *Signal and Information Processing (GlobalSIP), 2014 IEEE Global Conference on*, pp. 355-358, 2014.

[7] B. Jalali, J. Chan and M. H. Asghari, "Time-bandwidth engineering," *Optica,* vol. 1, pp. 23-31, 2014.

[8] M. Bass, C. DeCusatis, J. Enoch, V. Lakshminarayanan, G. Li, C. MacDonald, V. Mahajan, and E. Van Stryland, *Handbook of Optics, Third Edition Volume IV: Optical Properties of Materials, Nonlinear Optics, Quantum Optics (set): Optical Properties of Materials, Nonlinear Optics, Quantum Optics (set)*: McGraw-Hill Education, 2009.

[9] K. Thyagarajan and B. P. Pal, "Modeling dispersion in optical fibres: applications to dispersion tailoring and dispersion compensation," *Journal of Optical and Fibre Communications Reports,* vol. 4, pp. 173-213, 2007.

[10] W. Chao and Y. Jianping, "Fourier Transform Ultrashort Optical Pulse Shaping Using a Single Chirped Fibre Bragg Grating," *Photonics Technology Letters, IEEE,* vol. 21, pp. 1375-1377, 2009.

[11] R. A. Minasian, "Photonic signal processing of microwave signals," *Microwave Theory and Techniques, IEEE Transactions on,* vol. 54, pp. 832-846, 2006.

[12] H. Furukawa, T. Makino, X. Wang, T. Kobayashi, M. Asghari, P. Trinh, B. Jalali, W. S. Man, K. S. Tsang, and N. Wada, "Time-Stretch dispersive Fourier

transform based single-shot pulse-by-pulse spectrum measurement using a pulse-repetition-frequency-variable gain-switched laser," in *SPIE LASE*, pp. 6, 2018.

[13] Y. Han and B. Jalali, "Photonic time-stretched analogue-to-digital converter: fundamental concepts and practical considerations," *Lightwave Technology, Journal of,* vol. 21, pp. 3085-3103, 2003.

[14] V. Company, D. E. Leaird, and A. M. Weiner, "Dispersion requirements in coherent frequency-to-time mapping," *Optics Express*, vol. 19, pp. 24718-24729, 2011.

[15] D. R. Solli, J. Chou, and B. Jalali, “Amplified wavelength-time transformation for real-time spectroscopy,” *Nature Photonics* vol. 2 no. 1, pp. 48–51, 2008.

[16] Y. Dai, J. Li, Z. Zhang, F. Yin, W. Li, and K. Xu, "Real-time frequency-to-time mapping based on spectrally-discrete chromatic dispersion," *Optics Express*, vol. 25, pp. 16660-16671, 2017.

[17] C. Wang and J. Yao, "Microwave and millimeter-wave arbitrary waveform generation and processing using fibre-optics-based techniques," in *Broadband Network & Multimedia Technology, 2009. IC-BNMT '09. 2nd IEEE International Conference on*, pp. 909-912, 2009.

[18] H. Chi and J. Yao, "All-Fibre Chirped Microwave Pulses Generation Based on Spectral Shaping and Wavelength-to-Time Conversion," *in IEEE Transactions on Microwave Theory and Techniques*, vol. 55, no. 9, pp. 1958-1963, Sept. 2007.

[19] A. Dezfooliyan and A. M. Weiner, "Photonic synthesis of high fidelity microwave arbitrary waveforms using near field frequency to time mapping," *Optics Express*, vol. 21, pp. 22974-22987, 2013.

[20] Y. Xu, Z. Shi, H. Chi, X. Jin, S. Zheng, X. Zhang, "Relaxed dispersion requirement in the generation of chirped RF signals based on frequency-to-time mapping," *Optics Communications*, vol. 331, 2014

[21] V. Company, J. Lancis, and P. Andrés, "Incoherent frequency-to-time mapping: application to incoherent pulse shaping," Journal of the Optical Society of America, vol. 24, pp. 888-894, 2007.

[22] B. Jalali and M. H. Asghari, "The Anamorphic Stretch Transform: Putting the Squeeze on “Big Data," *Optics and Photonics News,* vol. 25, pp. 24-31, 2014.

[23] E. Sejdić, I. Djurović, J. Jiang, "Time-frequency feature representation using energy concentration: An overview of recent advances," *Digital Signal Processing*, vol. 19, no. 1, pp. 153–183, 2009.

[24] I. S. Lin, J. D. McKinney and A. M. Weiner, "Photonic synthesis of broadband microwave arbitrary waveforms applicable to ultra-wideband communication," *Microwave and Wireless Components Letters, IEEE,* vol. 15, pp. 226-228, 2005.

[25] E. Lucas, J. D. Jost, K. Beha, M. Lezius, R. Holzwarth and T. J. Kippenberg, "Low-noise microwave generation with optical microresonators," *2017 Conference on Lasers and Electro-Optics Europe & European Quantum Electronics Conference (CLEO/Europe-EQEC)*, pp. 1-1, Munich, 2017.

[26] Z. Weifeng, Z. Jiejun, and Y. Jianping, "Largely chirped microwave waveform generation using a silicon-based on-chip optical spectral shaper," in *Microwave Photonics (MWP) and the 2014 9th Asia-Pacific Microwave Photonics Conference (APMP), 2014 International Topical Meeting on*, pp. 51-53, 2014.

[27] C. Gu, D. Zhang, Y. Chang and S. C. Chen, "Digital micromirror device-based ultrafast pulse shaping for femtosecond laser," *Optics Letters,* vol. 40, pp. 2870-2873, 2015.

[28] J. Yao, "Photonic generation of microwave arbitrary waveforms," *Optics Communications*, vol. 284, no. 15, pp. 3723-3736, 2011.

[29] W. Chao and Y. Jianping, "Simultaneous Optical Spectral Shaping and Wavelength-to-Time Mapping for Photonic Microwave Arbitrary Waveform Generation," *Photonics Technology Letters, IEEE,* vol. 21, pp. 793-795, 2009.

[30] J. Capmany, C. L. G. Li and J. Yao, "Microwave Photonics: Current challenges towards widepread application," *Optics Express*, vol. 31, pp. 22862-22867, 2013.

[31] M. Kahn *et al.*, "Ultrabroad-bandwidth arbitrary radiofrequency waveform generation with a silicon photonic chip-based spectral shaper," *Nature Photonics* vol. 4, pp. 117–122, 2010.

[32] C. Wang and J. Yao, "Fibre Bragg gratings for microwave photonics subsystems," *Optics Express,* vol. 21, pp. 22868-22884, 2013.

[33] L. Ming and Y. Jianping, "Photonic Generation of Continuously Tunable Chirped Microwave Waveforms Based on a Temporal Interferometer Incorporating an Optically Pumped Linearly Chirped Fibre Bragg Grating," *Microwave Theory and Techniques, IEEE Transactions on,* vol. 59, pp. 3531-3537, 2011.

[34] C. Wang and J. Yao, "Chirped microwave pulse generation based on optical spectral shaping and wavelength-to-time mapping using a sagnac loop mirror incorporating a chirped fibre bragg grating," *Journal of Lightwave Technology,* vol. 27, no. 16, pp. 3336-3341, 2009.

[35] C. Wang and J. Yao, "Photonic Generation of Chirped Microwave Pulses Using Superimposed Chirped Fiber Bragg Gratings," *IEEE Photonics Technology Letters*, vol. 20, no. 11, pp. 882-884, 2008.

[36] L. Wangzhe and Y. Jianping, "Microwave and Terahertz Generation Based on Photonically Assisted Microwave Frequency Twelvetupling With Large Tunability," *Photonics Journal, IEEE,* vol. 2, pp. 954-959, 2010.

[37] L. Ming, W. Chao, L. Wangzhe, and Y. Jianping, "An Unbalanced Temporal Pulse-Shaping System for Chirped Microwave Waveform Generation," *IEEE Transactions on Microwave Theory and Techniques,* vol. 58, pp. 2968-2975, 2010.

[38] A. J. Fitzgerald, B. E. Cole and and P. F. Taday, "Nondestructive analysis of tablet coating thicknesses using terahertz pulsed imaging," *Journal of Pharmaceutical Sciences,* vol. 94, pp. 177-183, 2005.

[39] L. X. Zhang, J. Stiens, A. Elhawil, and R. Vounckx, "Multispectral illumination and image processing techniques for active millimeter concealed object detection," *Applied Optics,* vol. 14, pp. 6357 - 6365, 2008.

[40] Zhu, Yong-Kai et al. "A review of optical NDT technologies." *Sensors (Basel, Switzerland)* vol. 11, no. 8, pp. 7773-98, 2011.

[41] L. Oomen and W. J. P. A. Verbeek, "A real-time optical profile sensor for robot arc welding, " *Proceedings SPIE*, no. 449, pp. 62–71, 1984.

[42] J. A. Beraldin, M. Rioux, F. Blais, J. Domey, and L. Cournoyer, "Registered range and intensity imaging at 10-mega samples per second," *Optics Engineering*, vol. 31, no. 1, pp. 88–94, 1992.

[43] Fujimoto J.G., Pitris C., Boppart S.A., Brezinski M.E., "Optical coherence tomography: an emerging technology for biomedical imaging and optical biopsy," *Neoplasia*, vol. 2, pp. 9–25, 2000.

[44] J. M. Schmitt, "Optical coherence tomography (OCT): a review," *Selected Topics in Quantum Electronics, IEEE Journal of,* vol. 5, pp. 1205-1215, 1999.

[45] C. Ibarra-Castanedo and X. Maldague, "Pulsed Phase thermography reviewed," *Quantitative Infrared thermography Journal,* vol. 1, pp. 47 - 70, 2004.

[46] C. Hellier, *Handbook of Non-Destructive Evaluation*, 1st ed.: McGraw Hill, 2003.

[47] S. Shitov, V. Koshelets, S. Kovtonyuk, A. Ermakov and A. Baryshev "Ultra low noise sis-receivers for MM-Wave radio astronomy," *Cryogenics*, vol. 32, no. 1, pp. 497 – 500, 1992.

[48] O. Luukkonen, S. I. Maslovski and S. A. Tretyakov, "A Stepwise Nicolson–Ross–Weir-Based Material Parameter Extraction Method," in *IEEE Antennas and Wireless Propagation Letters*, vol. 10, pp. 1295-1298, 2011.

[49] A. Pourkazemi, J. H. Stiens, M. Becquaert and M. Vandewal, "Transient Radar Method: Novel Illumination and Blind Electromagnetic/Geometrical Parameter Extraction Technique for Multilayer Structures," in *IEEE Transactions on Microwave Theory and Techniques*, vol. 65, no. 6, pp. 2171-2184, June 2017.

[50] A. Popov, I. Prokopovich, V. Kopeikin and D. Edemskii, "Synthetic aperture approach to microwave holographic image improvement," *Proceedings of the International Conference Days on Diffraction 2014*, St. Petersburg, pp. 192-197, 2014.

[51] H. Hasegawa, "Improvement of range spatial resolution of medical ultrasound imaging by element-domain signal processing," *Japanese Journal of Applied Physics*, vol. 56, no. 7S1, 2017.

[52] M. Li, J. Hayward, "Ultrasound Nondestructive Evaluation (NDE) Imaging with Transducer Arrays and Adaptive Processing," *Sensors*, vol. 12, no. 1, pp. 42-54, 2012.

[53] Y. Wang, J. Gong, B. Dong, W. Bi, and A. Wang, "A quasi-distributed sensing network with time-division-multiplexed fiber bragg gratings," *IEEE Photonics Technology Letters*, Vol. 23, pp. 70–72, 2011.

[54] A. Shimamoto and K. Tanaka, "Geometrical analysis of an optical fiber bundle displacement sensor," *Applied Optics,* vol. 35, no. 34, pp. 6767–6774, 1996.

[55] University of Kent, School of Engineering Sciences and Technology 2014, Photonics Enabled High Throughput TeraHertz Coherence Tomography, viewed 21 May 2018, <https://www.eda.kent.ac.uk/>.

CHAPTER 3

PHOTONIC TIME-STRETCH ENABLED HIGH THROUGHPUT DISTRIBUTED FBG SENSORS

3.1 Introduction

The previous chapter provides a review of fundamental theoretical principles governing optical pulse propagation in a dispersive medium, the photonic Time-Stretch principle enabling wavelength to time mapping and STFT as an analysis tool.

In this chapter, a novel scheme demonstrating high-throughput dynamic strain sensing along the length of a chirped fibre Bragg grating (CFBG) has been shown. A theoretical description of fibre Bragg gratings (FBG) and chirped gratings including their application in strain and temperature sensing is discussed. A review of conventional approaches achieving strain interrogation is presented. The work performed in this chapter is a continuation and improvisation upon state-of-the-art microwave photonics solutions adopted for physical strain sensing. This chapter aims to highlight the advantages achieved by the strain sensing scheme implemented.

FBG fabrication and inherent characteristics allowing it to be used for strain sensing are discussed in section 3.2. Investigation of fabrication techniques for production of FBG and CFBG was not an objective of this research, but an overview is outlined to familiarise the reader with the capability to fabricate gratings for strain sensing applications. An overview of fibre grating based microwave and MM-Wave generation is provided in section 3.3. A critical review of previous methods allowing FBG based strain sensing is analysed and the need for a novel scheme proposed in section 3.4. Further on, the proposed novel architecture is described in detail in section 3.5. In section 3.6, the experimental procedure is outlined, and finally the measurement results and summary provided.

3.2 FBG Fabrication

A fibre Bragg grating (FBG) can be fabricated by changing the refractive index along a certain length of optical fibre in a periodic manner [1, 2]. Refractive index modulation in an FBG is achieved by exposing the fibre core to intense ultraviolet interference pattern [3, 4]. Figure 3.1 (a) depicts a typical FBG profile and the corresponding input-output spectral relationship.

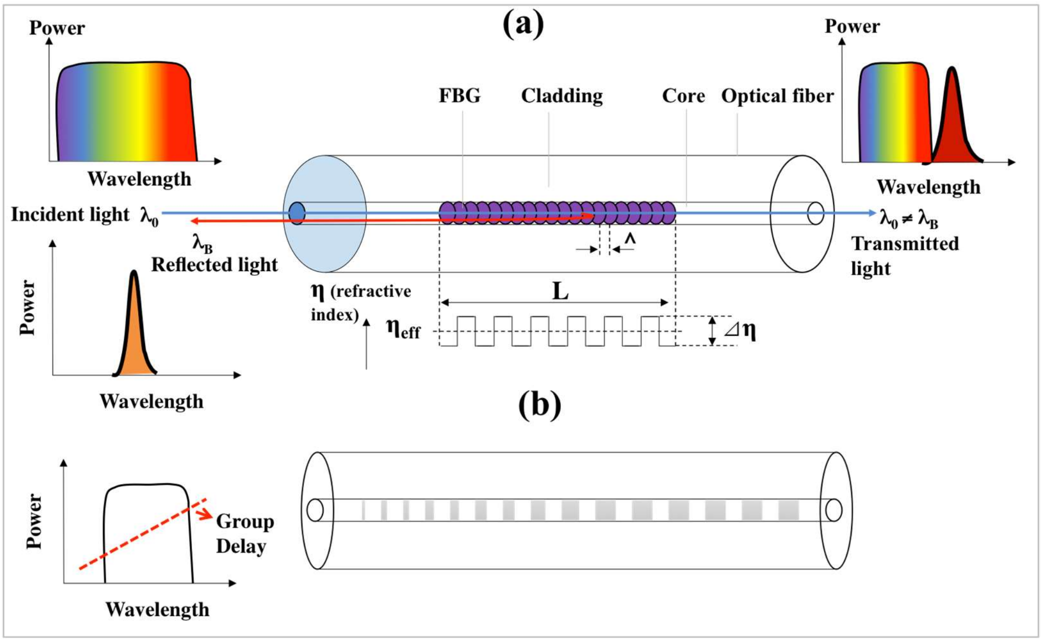

Figure 3.1 Refractive index profile, transmission and or reflection spectrum for (a) Fibre Bragg Grating (b) Linearly Chirped Fibre Bragg Grating.

Similarly, gratings can also be fabricated to achieve a non-uniform chirped grating period allowing broadband reflection wherein reflection spectrum or rather the reflected wavelength can be related to specific positions along the grating length [7 – 10]. Figure 3.1 (b) depicts the profile of a chirped Fibre Bragg grating. A large dispersion is also a unique trait exhibited by a chirped FBG (CFBG).

The holography based masking [1] method enables the creation of a standing wave within the core of a Germanium doped fibre. The characteristic properties of Germanium doped fibre when exposed to visible light in the 480 – 500 nm spectrum carve an intensity dependent refractive index profile. Another widely used technique, known as phase masking relies on lithography based mask etching to create a diffraction grating that disperses incoming UV light forming a fringe pattern upon the exposed fibre to effect refractive index modulation [3]. Similarly, a number of techniques are in practice to fabricate chirped fibre Bragg gratings where the refractive index period should increase or decrease in a linear manner. Reported methods investigate chirped fibre Bragg grating fabrication by employing fibre bending techniques, a predetermined strain gradient or temperature gradient applied upon the fibre length when exposed to UV light [1, 6 - 8], interference of different wavefronts, chirped phase mask fabrication [5].

3.3 Photonic Generation of Microwave and MM-Wave based on Fibre Bragg Gratings

Modifying an optical fibre to behave as an FBG enables it to be used in a diverse range of applications, including communications, optical sensing and recently in a lot of microwave photonic applications involving signal processing and photonic arbitrary waveform generation [9]. Tailoring the spectral response of an FBG allows a means of spectrally shaping incident spectrum and enabling dispersion induced wavelength to time mapping [10] of ultrashort pulses thus allowing another solution to an all fibre based photonic microwave generation scheme [11, 12].

Capitalizing upon the unique properties exhibited by fabricating fibre gratings such as immunity to electromagnetic interference (EMI), high resistance to chemical corrosion, lightweight and ease in signal transmission [9], many techniques realising the potential of CFBGs in Photonics-based microwave generation have been extensively investigated. The method demonstrated in [11] shows an FBG designed to have a refractive index with a chirped Free Spectral Range by superposing two linearly chirped fibre Bragg gratings with a small longitudinal offset. The Free Spectral Range carved by the spectral properties of the grating are translated to the temporal waveform at the output using the Dispersion induced Frequency to Time mapping concept. A cavity length proportional to resonance wavelength enabling chirped spectrum shaping is achieved. Superimposing two LCFBGs with identical chirp rates leads to optical resonances due to the existence of a Fabry Perot cavity formed by superposition of two CFBGs at different wavelengths. Since distributed Fabry Perot cavity has a constant cavity length, reflection spectrum would have a fixed FSR. Superimposing two FBGs with varying rates of chirp results in distributed Fabry Perot cavity length proportional to resonance wavelength. Thus a spectral response with varying FSR is obtained. Shaped spectrum is further on mapped to the time domain.

An extension of the proposed technique has also been further utilised to generate photonic microwave pulses by integrating a linearly chirped fibre Bragg grating in a Sagnac loop mirror configuration and using the frequency to time mapping to create chirped microwave pulses [12]. Photonics assisted microwave and MM-Wave generation is extensively discussed in Chapter 2: focusing on dispersive Fourier transformation based microwave and MM-Wave pulse generation schemes. The utility of fibre gratings in achieving photonic microwave generation is highlighted. In the next section, we focus on the role of fibre Bragg grating as strain sensors and present a novel strain detection scheme attaining real-time strain monitoring capability along the length of the chirped fibre grating [13, 14].

3.4 Fibre Bragg Gratings for Strain Sensing

Important physical parameters that determine material properties require exact measurement of refractive index, metrological dimensions and other chemical and biomedical parameters. The use of sensors in obtaining strain and temperature information is an essential requirement in various applications including civil engineering, structural health monitoring which includes government infrastructure, airports, railways, bridges and tunnels. The inspection of aircraft diagnostics, engine part production and in structural maintenance [15 - 17].

Optical fibre Bragg grating (FBG) sensors allow easy integration into carbon and glass reinforced fibre composites that are extensively used nowadays in modern aeroplane and wind turbine structures. Also, the ability of fibre gratings to be employed in versatile conditions ranging from cryogenic temperatures to dangerous and chemically harsh and abrasive environment allow them to be utilised in a wide range of sensitive applications. Thus, a theoretical and mathematical basis for fibre grating sensing is required. Effective refractive index for CFBG can be expressed as [18, 19]:

$$\eta_{eff}(z) = \eta_{eff} + \Delta\eta_{eff}(z)\left(1 + v\cos\left(\frac{2\pi z}{\Lambda_o} + \phi(z)\right)\right) \tag{3.1}$$

Where v is fringe visibility and Λ_0 is the minimum grating period at minimum strain. $\phi(z)$ is the phase of chirped grating. Chirp profile for LCFBG can be expressed as:

$$\Lambda(z) = \Lambda_0 + cz \ ; \ c = \frac{d\Lambda}{dz} \tag{3.2}$$

Reflected spectrum, $R(\lambda)$ is a function of strain distribution along the grating, Strain modifies $\Lambda(z)$ and $\eta(z)$.

The Bragg wavelength can be calculated as follows [19]:

$$\lambda_B = 2\eta_{eff}\Lambda \tag{3.3}$$

Where Λ is the grating period and n_{eff} is the effective refractive index.

A chirp in the period of a chirped grating fibre Bragg grating of length L_g, can be related to the chirped bandwidth $\Delta\lambda_{chirp}$ as follows:

$$\Delta\lambda_{chirp} = L_g \Lambda \tag{3.4}$$

Reflection from a chirped grating is dependent on wavelength, light entering a positively chirped grating (increasing period from input end) suffers a delay τ upon reflection:

$$\tau(\lambda) = \frac{\lambda_B - \lambda}{\Delta\lambda_{chirp}} \frac{2L_g}{v_g} \tag{3.5}$$

Where v_g is the average group velocity of light in the fibre.

A change in strain and or temperature effects both the refractive index n_{eff} and the grating period Λ .

$$\frac{\Delta\lambda_B}{\lambda_B} = (1-\rho_o)\varepsilon + (\alpha_\Lambda + \alpha_\eta)\Delta T \tag{3.6}$$

ρ_o is the strain optic coefficient ε is the corresponding strain α_Λ is thermal expansion coefficient and α_η is the thermo-optic coefficient with ΔT being the corresponding temperature change. Therefore most FBG sensors are wavelength modulated. Reflected spectrum is not only shifted but undergoes a shape change. The shift in local Bragg wavelength subjected to localised strain gradient can be expressed as:

$$\Delta\lambda_B(z) = \left[\frac{\partial\Lambda}{\partial\varepsilon} + \frac{\partial\eta_{eff}}{\partial\varepsilon}\right]\lambda_B(z)\Delta\varepsilon \tag{3.7}$$

The main optical sensor framework is based on the inherent Bragg wavelength deviation. FBG sensor interrogation schemes map the change in Bragg wavelength to overall strain and or temperature change. Literature review presented in this thesis will focus on strain sensing as a high throughput intragrating strain sensing mechanism is proposed in the experimental work outlined section 3.5.

3.4.1. Quasi Distributed Fibre Bragg Grating Sensing

FBG sensor array interrogation using passively mode-locked fibre laser is implemented in a number of research laboratories [20, 21]. FBG sensors have been multiplexed using an array of FBGs to obtain strain and temperature distributions at discrete locations along a structure to provide quasi-distributed sensing [22, 23]. This enables sensing capability over several km of fiber and is essential for studying dynamic phenomena such as crack formation at critical junctures along the structure the grating is mounted on. The small size and light-weight FBG architecture enable embedded sensor configuration, integration into concrete materials allowing monitoring of dams, tunnels and smart structures of the future. FBG interrogation schemes have demonstrated great success as of late, novel techniques acquiring ultrahigh sub-pm resolution can be realised [24–26]. Particular applications pertaining to real-time measurement in industrial and scientific sector require high temporal resolution interrogation schemes. For instance, an ultrafast FBG interrogation system is quintessential for analysing dynamic phenomena including chemical analytics such as real-time corrosion rate monitoring in pre-stressed mild steel structures, monitoring rapid vibrating objects such as aircraft engine diagnostics and large infrastructure such as dams, bridges and oil or gas pipeline.

Utilising Fourier domain mode-locked swept laser [27] has enabled interrogation speeds of up to 100 kHz, quasi-distributed sensing is achieved by multiplexing gratings allowing both static and dynamic pressure to be measured [28 - 30].

An electronic tracking system for multiplexed FBG sensors has also been implemented. Light from ELED illuminates one or more gratings at different Bragg wavelengths through a coupler. An AOTF filters the reflected light and detected by a trans-impedance receiver. AOTF acts as a band-pass filter by using the acousto-optic effect to diffract and shift the frequency of light using sound waves. A piezoelectric transducer is attached to a material such as glass. Oscillating electrical signal drives the transducer to vibrate which creates sound waves in material; phases of compression and expansion changing material refractive index. Incoming light scatters off, and interference occurs similar to Bragg diffraction. AOTF select and transmit a single wavelength from the incoming light. The wavelength of light chosen is a function of the frequency of RF signal applied to AOTF crystal.

DR Solli and K. Goda have most recently proposed a real-time spectroscopy technique [31, 32] empowering FBG sensor cross-examination by prompting ultrafast and single-shot estimation at speeds of several MHz [33, 34]. This is accomplished by dispersion-induced frequency-to-time-mapping, translating the spectral profile to its temporal analogue [10, 25, 32], which can be captured in real-time using a single high-speed photodetector. In addition, research efforts have been made to improve the interrogation resolution and signal-to-noise ratio [35], and to conquer the fundamental compromise between the interrogation speed and resolution [36] in real-time spectroscopy based interrogation systems. The sensing techniques employed have attained a fair amount of success in estimating dynamic extremes of materials.

Nevertheless, the already announced rapid FBG sensor cross-examination frameworks all miss the mark in the interrogation of strain along the length of the fibre: they can just quantify the average strain or temperature change over the length of the FBG sensor [26, 37]. While semi-distributed strain detection can be executed by multiplexing many discrete FBG sensors, high spatial resolution, fully distributed estimation of strain and temperature over a short measurement length along an FBG is required in high-resolution, dynamic structure health monitoring, such as crack formation and or porosity induced tensile strength determination of material medium. To sum up, quasi-distributed sensing employs FBG sensor arrays situated at key areas along a structure to delineate temperature or strain along the grating. The method, however, gives only a mean of the measured difference along the length of every grating by monitoring the peak reflected Bragg wavelength of every grating sensor [13, 14]. For this reason, it is undesirable for applications where a continuous profile of the measurand, as a feature of position along the grating length, with micrometre and millimetre spatial resolution is needed (e.g. to pinpoint hot spots or locate cracks). The approach works well for large structures wherein spatial resolution isn't always a concern, however, is not appropriate when high spatial resolution is required such as investigating the stress and or temperature gradient at excessive-strain points, structural debonding and regions susceptible to crack formation [41, 44].

3.4.2. Fully Distributed Intra Fibre Bragg Grating Sensing

A linearly chirped fibre Bragg grating (LCFBG) is a promising contender for fully distributed sensing on account of its more extended grating length and more broad reflection bandwidth contrasted with typical uniform FBGs. The local Bragg wavelength of the LCFBG relates explicitly the distributed sensing data along the grating length.

$$\Delta\lambda_B(z) = \lambda_B(z)\left(1-\rho_o\right)\varepsilon(z) \tag{3.8}$$

where ρ_e is the strain-optic coefficient of the optical fibre and $\varepsilon(z)$ is the local strain which modifies the local Bragg wavelength $\lambda_B(z)$ at the specific position z. State-of-the-art interrogation schemes are highlighted in this section.

When a linearly CFBG is subjected to axial strain, there is a re-distribution of the period as well as a variation in the refractive index due to the photo-elastic effect. The photoelastic effect refers to strain dependent material dielectric constant modification due to birefringence when fibre is subjected to strain. If strain field is uniform whole of the chirped Bandwidth (BW) is simply shifted to the longer wavelength region with increasing strain. Thus, non-uniform strain applied to an FBG has the effect of increasing/decreasing chirp in the FBG. Non-uniform or differential strain will shift the Bragg wavelength, and the amount of shift is related to the average strain, while the degree of broadening is related to strain gradient applied. The overall change to the reflection spectrum imparted by every component of the BW of a chirped FBG when it is strained is translated to a significant group delay and thus large optical path length change.

Distributed sensing of pressure over a few centimetres [38, 39] has been demonstrated. An array of CFBGs of nearly equal reflectance is positioned along the length of a long fibre with each grating behaving as a sensing point. The sensor operates by monitoring the central wavelength shift of each sub-grating. When a transverse load or pressure is applied to the grating, the central wavelength of the affected/shifted sub-grating gives the location of the load, and the magnitude of the load can be calculated from the wavelength shift. Even 10 cm long weak fibre Bragg gratings, implying gratings with a lower reflection coefficient are utilised for distributed reflection spectrum measurement [40] with a spatial resolution of 2 mm. The requirement for a broadband tunable laser source hampers the measurement speed, as it is dependent on the tuning speed of the laser employed. Fast tuning laser source with high wavelength resolution is required. Similarly, modulating the refractive index along core of a fibre optic along several metres and kilometres to meet the specific sensing criteria makes the measurement system complicated and expensive. Direct spectrum measurement [41] is simple and straightforward as the local strain changes cause spectral dips around particular wavelengths corresponding to unique position of CFBG, however, spatial resolution is reduced and spectral acquisition is limited in measurement speed. A fibre loop ring-down (FLRD) spectroscopy has been proposed to interrogate LCFBG sensors with 2 mm spatial resolution and 1 kHz temporal resolution [37, 42]. A light pulse coupled into a fibre loop experiences internal fibre transmission losses. Output signal observed by a PD follows an exponential decay. The time required for light intensity to decrease to *1/e* of the initial light intensity is known as ring down time. External perturbation such as pressure, temperature or stress results in an additional loss which causes a change in the ring down time. FLRD requires lower laser power, allows multiple sensor units to be multiplexed, and offers higher reconfigurability. Attenuation of the light intensity maps cavity loss to the measured decay time in FLRD spectroscopy. An Acousto-optic modulator (AOM) is used to modulate a monochromatic light source; LCFBG is integrated into the system architecture via a circulator. The resonant wavelength of an LCFBG is directly proportional to the position along the grating length, the total time for light to complete one cycle, *T*, wherein intensity drops to *1/e* of its original value can be calculated as follows:

$$T = \frac{\eta_{fiber} L}{c} \tag{3.9}$$

If the optical pulse train makes *n* ring down trips, the decay in signal attenuation can be related to the corresponding time difference $\Delta T\ _n = n \times \Delta T$. The average round-trip time can be calculated more accurately in this way, resulting in higher spatial resolution.

Spatial resolution of 300 µm has been achieved using time domain low-coherence reflectometry (LCR) [43]. As demonstrated by *Volanthan et. al*, a broadband source illuminates a single mode fibre Michelson interferometer. The reference arm contains a broadband mirror and variable delay whereas the interrogation arm contains the sensor grating. The exact position in which the grating desires to be interrogated can be established by matching the reference arm and sample arm. A tunable filter is utilised to select the interrogation wavelength. A VCO controls the wavelength of the filter. Interference pattern is recorded at the detector when the filter wavelength and interrogation wavelength match. A PZT modulates the reference path length over a few microns to serve several interference fringes. When the Bragg wavelength and filter wavelength are equal, the visibility of the interference pattern is maximum. In essence, distance is obtained from the variable delay, the wavelength is deduced from the wavelength of the tunable filter and reflectivity is measured from the amplitude of the interference fringes [43]. Strain profile is obtained by subtracting the unstrained wavelength profile of the grating from the measured wavelength profiles and dividing by unstrained wavelength profile and photo-elastic coefficient of fibre. However, mechanical movement of the reference arm limits the measurement speed, and the signal-to-noise ratio is thus reduced due to the use of a low-coherence optical source. Distributed strain measurement with the spatial resolution of 4 mm has been demonstrated using Linearly Chirped Fibre Bragg Gratings (LCFBG) and optical frequency-domain reflectometry (OFDR) [44]. No mechanical movement is required, but the interrogation speed is limited by the laser wavelength sweeping and falls below kHz range. Rayleigh and Brillouin based distributed fiber optic sensors have been developed to monitor distributed temperature and strain information for decades [49, 50]. Though they have the advantage of commercial availability, long detection range, however, the complex and expensive system configuration with sophisticated opto-electronic detection capability hamper their utility. In this thesis, a novel interrogation technique for fully-distributed LCFBG sensors that achieve simultaneous high temporal and spatial resolution based on optical time-stretch frequency-domain reflectometry (OTS-FDR) is proposed. The utility of intragrating sensing allowing temperature independent, high spatial resolution strain sensing at local hot spots (regions of interest) has been outlined. A unique proposal allowing intragrating strain sensing for extraction of non-uniform strain gradient using Mode Locked Lasers (MLL) is demonstrated. The proposed scheme achieves a high strain resolution coupled with a high spatial resolution thanks to the ultrafast data acquisition.

3.5 Distributed Fibre Grating Sensor Based on Optical Time-Stretch Frequency Domain Reflectometry

The utility of fully distributed sensing can be realized in structural health monitoring wherein techniques involve obtaining continuous profile of strain and or temperature over entire grating length to effectively map distribution of these parameters near attachment points, cracks or stress concentrations. The results of this chapter form the basis for range sensing, temperature and strain discrimination distributed strain and temperature sensing, crack location in composite materials and pressure sensors for monitoring non-uniform pressure gradient. A passively mode-locked laser is used to generate highly coherent ultrashort optical pulses with a wide optical spectrum as shown in Figure 3.2. The optical pulse is first stretched through a dispersion compensating fibre (DCF) and then sent to the Michelson interferometer. An optical time-stretch frequency domain reflectometry (OTSFDR) is therefore formed, and the spectral interferogram is mapped to a temporal interference pattern thanks to dispersion-induced frequency-to-time mapping also referred to as Dispersive Fourier Transform. In the OTSFDR scheme, the principal frequency, f_{RF} of the mapped temporal waveform is determined through the preliminary time difference set τ, and overall chromatic dispersion of the DCF $\ddot{\Phi}$.

$$f_{RF} = \frac{\tau}{\ddot{\Phi}} \tag{3.10}$$

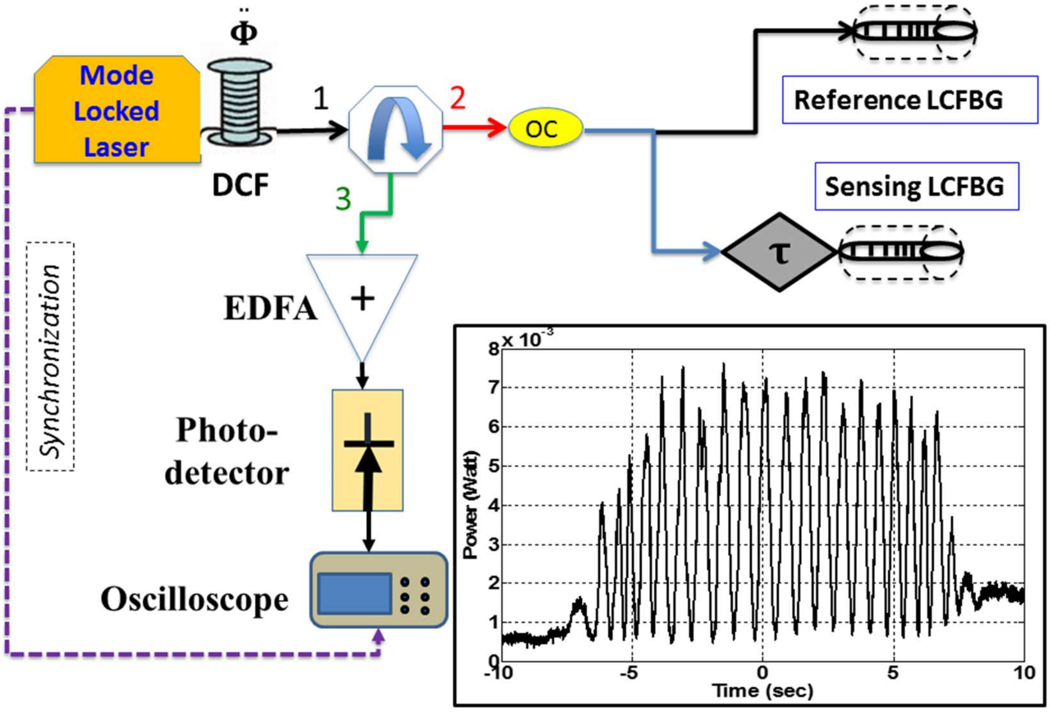

Figure 3.2 The proposed ultrafast and high spatial resolution LCFBG interrogation system based on optical Time-Stretch frequency domain reflectometry (OTS-FDR). Inset: the measured initial temporal interference waveform with no strain applied. EDFA: erbium-doped fibre amplifier, DCF: dispersion compensating fibre, OC: optical coupler, LCFBG: linearly chirped fibre Bragg grating.

When a local strain $\varepsilon(z)$ is applied to the sensing LCFBG with a chirp rate *C (nm/cm)*, the change of local Bragg wavelength $\Delta\lambda_B(z)$ introduces a time delay change, $\Delta\tau$, given by [45]

$$\Delta\tau = \left(\frac{2\Delta\lambda_B}{C}\right)\frac{\eta_{eff}}{c} \tag{3.11}$$

Where c is the speed of light and n_{eff} is the effective refractive index of the fibre Bragg grating. This extra-temporal shift $\Delta\tau$ is added to the overall time delay between two pulses in interferometer arms and leads to the change of instantaneous RF frequency, f_{RF}, in the temporal interference waveform.

The proposed cross-examination approach can be clarified intuitively by taking a gander at the difference in grating chirp due to the applied strain. Figure 3.3 (a) delineates the impact of uniform strain upon the sensing LCFBG, resulting in a redistribution of the period while maintaining the same chirp rate. Beating the two time delayed and stretched optical pulses at a PD yields a temporal waveform with a constant RF frequency across the pulse duration, as shown in Figure 3.3(b). The change of RF frequency compared to the strain-free case can be used to detect the uniform strain applied.

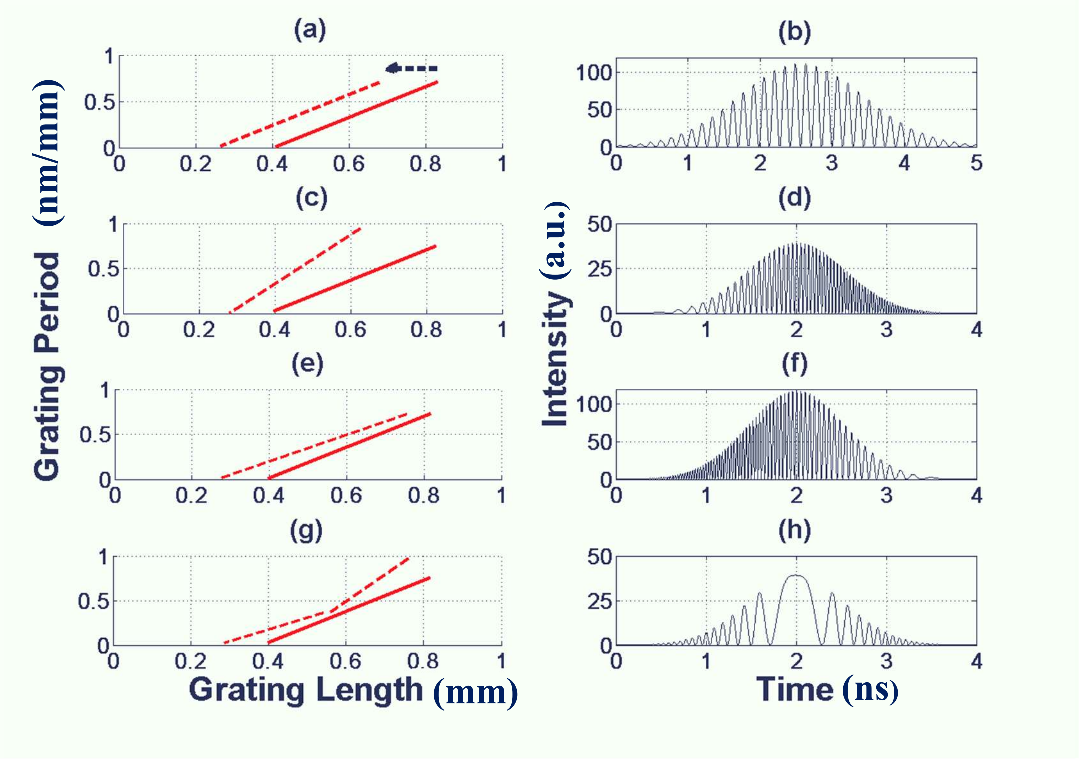

Figure 3.3 Comparison between redistribution of local Bragg wavelength in sensing grating (dashed lines) with respect to reference grating (solid lines) for uniform (a) and non-uniform strains (c), (e) and (g) applied. Figures (b), (d), (f) and (h) show the resulting temporal waveforms.

When non-uniform strain gradient is applied to the sensing LCFBG, its chirp rate will be changed differently with respect to the reference grating according to the local strain, resulting in chirped waveforms with a monotonic increase or decrease in instantaneous RF frequency [24], as shown in Figs. 3.3 (c-f). On the other hand, a nonlinear strain gradient, wherein a part of the grating is non-uniformly stretched, and the other part is non-uniformly compressed, produces a beating waveform with its frequency chirp rate being swapped, as can be observed in Figs. 3.3(g) and (h).

3.6 Experimental Results

To confirm the utility of the proposed idea, a proof-of-concept experimental procedure based on the setup shown in Figure 3.2 is performed. A passively mode-locked fibre laser (Calmar MENDOCINO FPL) is employed as the optical source to generate a transform-limited Gaussian pulse train with a repetition rate of 50 MHz. The ultrashort optical pulse has a full-width at half-maximum (FWHM) pulse width of 800 fs, a 3-dB spectral bandwidth of 16 nm and a central wavelength of 1550 nm.

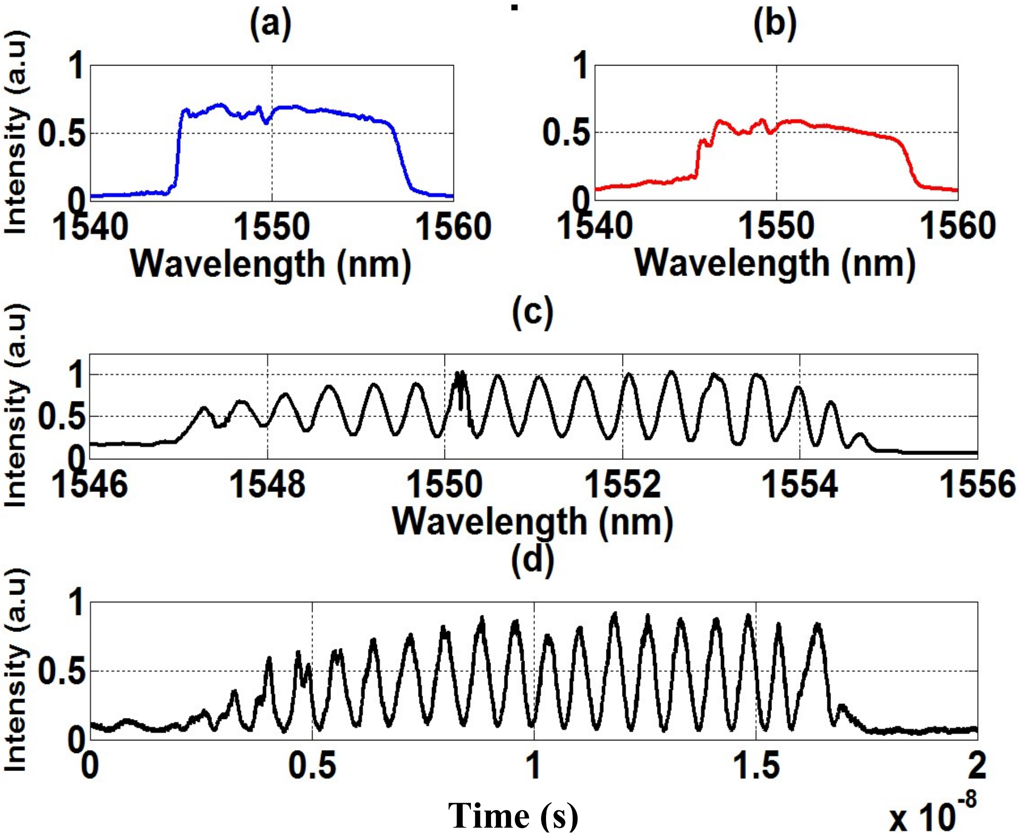

Figure 3.4 The measured basic OTS-FDR performance with no strain applied. (a) Reflection spectrum from the reference LCFBG, (b) reflection spectrum from the sensing grating, (c) spectral interferogram, (d) temporal interference waveform verifying the dispersion-induced wavelength-to-time mapping.

Two 2.5 cm long LCFBGs with an identical centre wavelength of 1551.5 nm and 3-dB bandwidth of 7 nm are employed as the sensing and reference gratings. A VODL is inserted in the sensing arm of the interferometer to control the initial time delay difference between two arms. A DCF with total group velocity dispersion (GVD) of $\ddot{\Phi}=11520$ ps^2 is used for optical time-stretch process. The mapped temporal interference waveform is detected by a 53 GHz photodetector and recorded using a high-speed sampling oscilloscope (Agilent 86100A).

Figure 3.4 demonstrates the calibration phase OTS-FDR execution when no strain is applied. A uniform frequency microwave pulse with frequency determined by the initial time delay is recorded. Figure 3.4 (a) and (b) portray the reflected spectra of the reference and detecting LCFBGs, individually. The reflection spectra are obtained by removing the optical coupler (OC) depicted in Figure 3.2 and fixing each grating individually at port 2 of the circulator. The spectrum is collected using an Optical Spectrum Analyser (OSA) at the output of the Erbium Doped Fibre Amplifier (EDFA). A spectral interferogram is framed from interference between the reflected spectra from the sample and reference LCFBGs, as shown in Figure 3.4 (c). The temporal waveform after optical Time-Stretch is depicted in Figure 3.4 (d), which suggests that under the far-field Fraunhofer condition, the dispersion incited wavelength-to-time mapping is successfully achieved. Note that as the DCF is characterised by a negative GVD, the longer wavelength will have a shorter time delay (travelling faster).

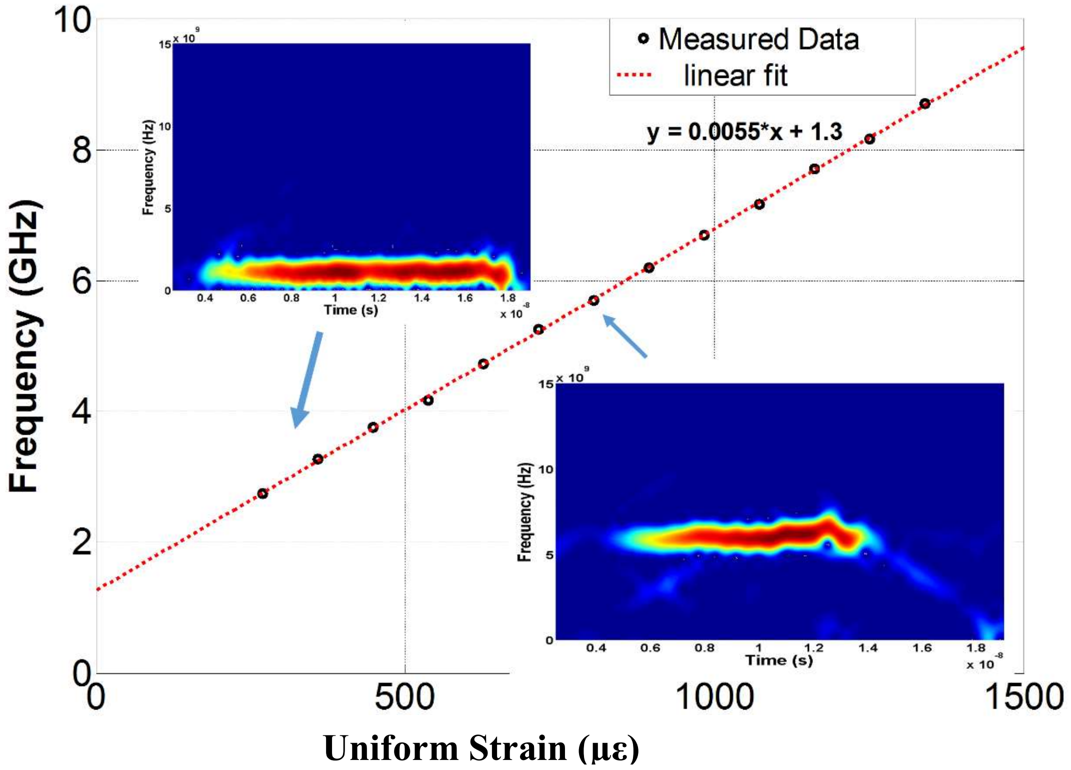

Figure 3.5 Characterisation of the interrogation system by applying various uniform strains. Insets show spectrograms of the temporal interference patterns at uniform strain values of 180 and 625 με, respectively. A linear fitting result is also shown in solid red line.

To characterise the interrogation system's response, the sensing LCFBG was first consistently extended with uniformly increasing applied strain, which generates single-tone temporal waveforms with exclusive uniform RF frequencies. Figure 3.5

shows the measured RF frequency as a function of the applied uniform strains. Spectrograms of two recorded waveforms are computed utilising Short Time Fourier Transform (STFT) investigation and illustrated as insets in Figure 3.5 for uniform strain estimations of 180 and 625 με, individually. It is additionally verified that the instantaneous frequency over time is relatively steady over the entire waveform. From straight fitting of the deliberate information, a frequency change to combined strain ratio of 5.5 MHz/με is obtained. Keeping in mind the end goal, to exhibit the capacity of our cross-examination method to monitor fully distributed strain, more analyses have been done to apply non-uniform extension and pressure along the detecting LCFBG with a uniform strain slope. We stick the grating onto a versatile and adaptable substrate. At first, the substrate is bowed to an illustrative shape. In this manner, the detecting LCFBG glued on to the surface of the substrate will experience the ill effects of non-uniform strain execution. As the longer wavelength part of the grating is towards the centre of the parabolic form substrate, it will likely be stretched more than the shorter wavelength component. The grating period inside the detecting LCFBG is remodified as delineated in Figure 3.3 (c). Figure 3.6 (a) demonstrates the produced microwave waveform with a negative chirp, as confirmed by its spectrogram appeared in Figure 3.6 (b).

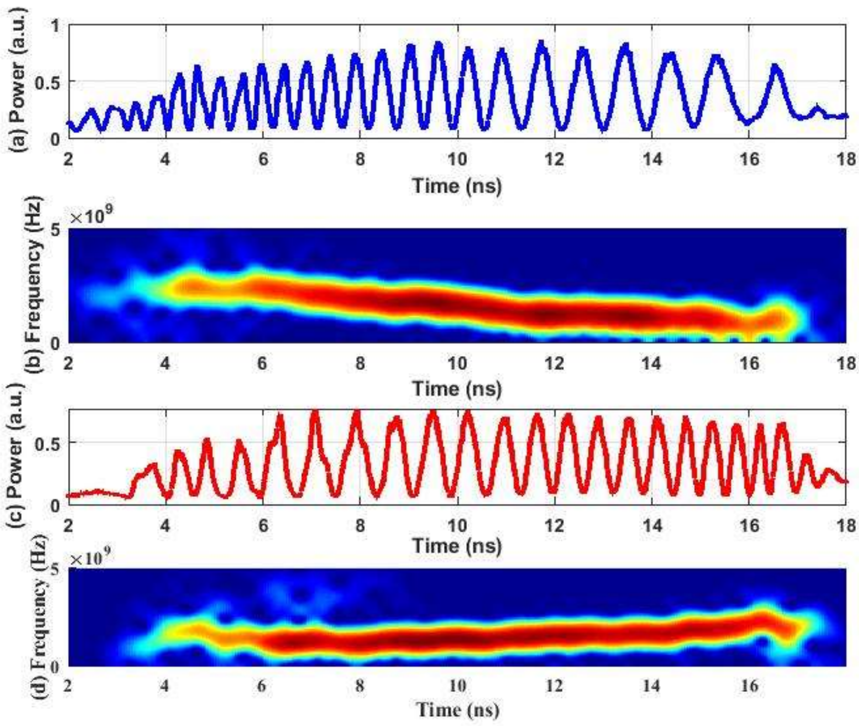

.

Figure 3.6 Demonstration of nonuniform strain sensing. The measured temporal waveforms (a, c) and their spectrograms (b, d) for non-uniform expansion and compression of the sensing LCFBG, respectively

In a second case, the substrate is bent to an inverse parabolic shape. Due to the applied nonuniform compression along the sensing LCFBG with more substantial wavelength part under more compression, a positively chirped temporal waveform is obtained as shown in Figure 3.6 (c) and its spectrogram depicting instantaneous RF frequency is shown in Figure 3.6 (d). The change in instantaneous RF frequency at a specific moment of time mirrors the appropriated nonuniform strain and can be mapped to the spatial area along the length of the LCFBG. The x-axis denotes time in ns for all 4 graphs. The vertical axis in spectogram represents frequency. The amplitude of a particular frequency at a particular time is represented by the color, with dark blues corresponding to low amplitudes and brighter colors up through red corresponding to stronger amplitudes.

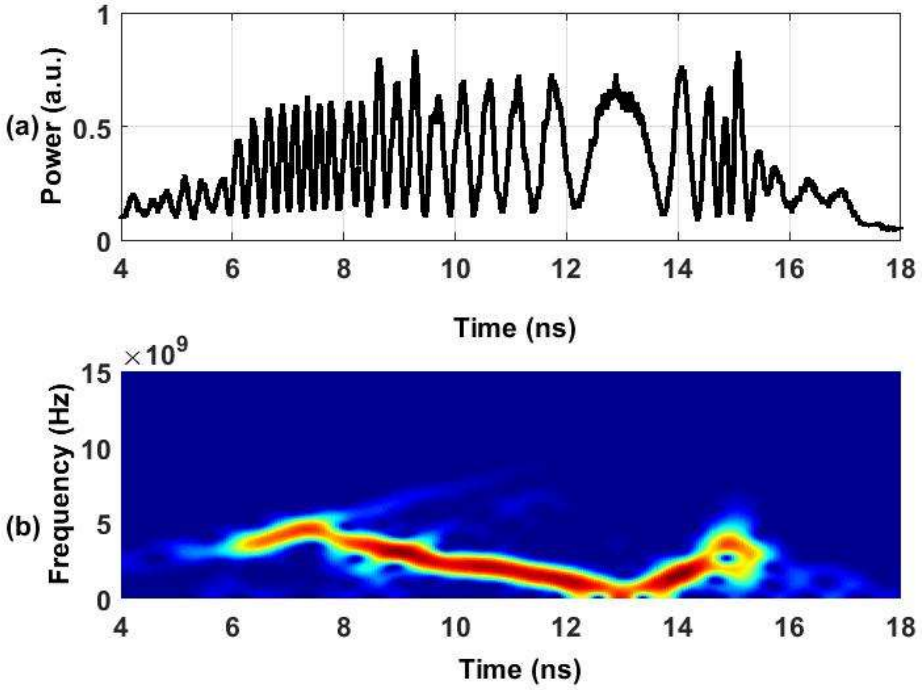

Figure 3.7 Demonstration of changing strain gradient by applying S-shape bending. (a) The measured temporal interference waveform and (b) its spectrogram showing different frequency sweeping rates.

In order to additionally show the impact of non-linear strain gradient, the substrate is bent to an S-shape, enabling part of the grating period to be non-uniformly stretched and the other part expanded. Such a strain profile brings about an adjustment in the grating chirp rate of the sensing LCFBG, as delineated in Figure 3.3 (g). This differential local enlargement and contraction of the grating period can be translated to the local chirp in frequency sweep inside the beating temporal waveform, as illustrated in Figure 3.3 (h). An experiment has been carried out to verify this idea. Figure 3.7 depicts the measured temporal beating waveform and its corresponding spectrogram under the implemented non-uniform stress gradient. Longer Bragg wavelength part of the grating is under non-uniform strain, prompting negative chirp rate of RF frequency amid the main (left) portion of the waveform. An adjustment in the chirp rates indicates the spatial location, from which the rest of the piece of the grating is under non-uniform pressure. The moment in time denoting a shift in chirp rates can be mapped to the corresponding spatial location.

The 5.5 MHz/με sensitivity also determines the strain resolution of the proposed interrogation scheme. The frequency resolution is defined as the sampling frequency (67.5 GS/s) divided by the number of raw data points (1350) which in my experiment is 50 MHz. Mapping the 5.5 MHz/με sensitivity to the minimum frequency change that can be measured results in a strain resolution of 9.1 με. Similarly, the sampling rate of the digitizer limits the spectrum resolution [32] as follows:

$$\partial\lambda_{res} = \left(fDz\right)^{-1} \tag{3.12}$$

where f is the sampling rate frequency, D is the dispersion of the fiber in (ps/nm.km) and z is the length of fibre employed for DFT. This results in a wavelength resolution of 0.01 nm. The 7 nm Bragg spectrum of the LCFBG is fabricated along a grating length of 25 mm, the minimum wavelength resolution can be mapped to a minimum spatial resolution of 31.5 μm along the grating length.

Crack detection: The high strain sensitivity and high spatial and temporal resolution of the proposed interrogation scheme provide adequate inspiration to investigate the ability of LCFBGs to recognise breaks or separations along the substrate onto which the sensor grating is mounted. Keeping in mind the end goal, to exhibit this angle, we penetrated two openings with distance across of 2 mm isolated by 10 mm along the inside hub of the substrate and stuck the detecting LCFBG over the substrate crossing the gaps. A non-uniform expansion of the whole sensing grating was performed. The two short sections of the LCFBG that fell into the hole areas acted as dividing points and two sides of each point are subjected to different stain change. Based on the theory of OTS-FDR as explained above, a sudden instantaneous frequency change is expected at the specific instant time corresponding to each individual holes. Figure 3.8 (a) shows the recorded temporal beating waveform and a measure of the instantaneous RF frequency along time can be observed from Figure 3.8 (b). The two jumps in instantaneous frequency is a clear evidence that the two holes have been detected and their locations are determined from the instant time of the frequency hopping.

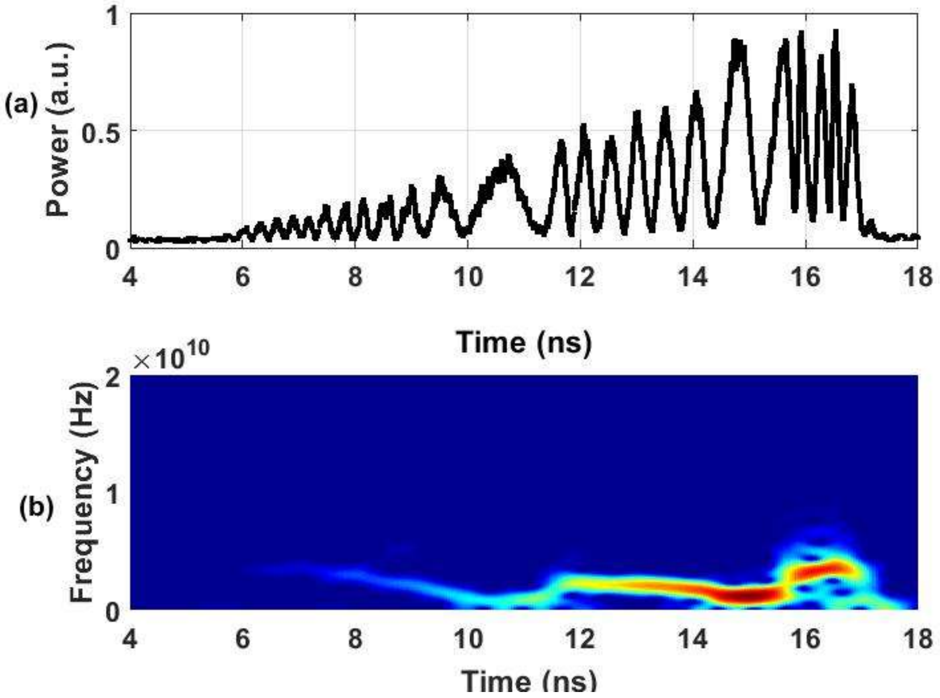

Figure 3.8 Demonstration of local crack detection. (a) The measured temporal interference waveform and (b) its spectrogram clearly showing two frequency hoppings which identifies the locations of the two holes.

Code in appendix A was used to perform Short Time Fourier Transform analysis on the raw data obtained.

3.7 Data-compressed signal detection

The capability of the novel CFBG based fully distributed sensing scheme is essentially limited by the sampling rate and bandwidth of back-end electronic digitiser. More importantly, this real-time FBG sensor interrogation system continuously generates a vast volume of data, which challenges even the most advanced electronic circuitry, data storage device, and digital signal processing units. The electronic bottleneck and big-data challenge in high-throughput FBG sensor interrogation systems can be addressed with the help of compressive sensing [46]. Signal information with a data length of N is measured M times iteratively (M < N), then it is transmitted, received and reconstructed using a recovery algorithm. A schematic of the proposed photonic compressive sensing technique in data-efficient interrogation system for high-throughput distributed FBG sensors is depicted in Figure 3.9.

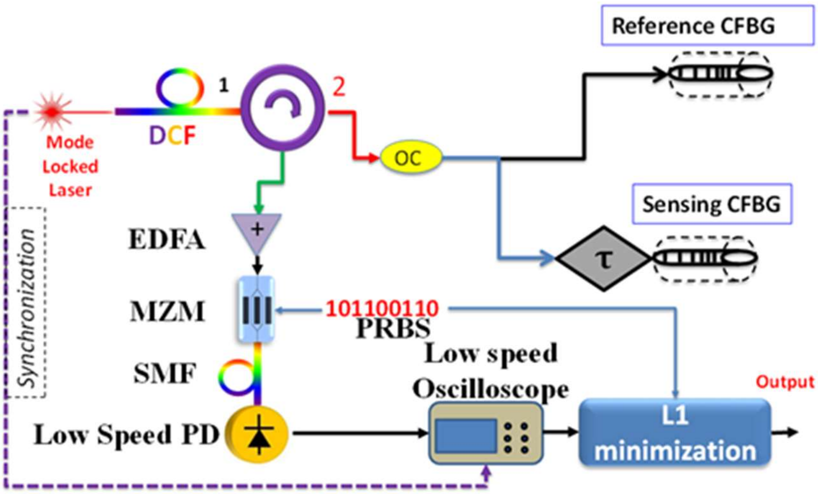

Figure 3.9 Schematic of proposed CS OTS-FBG system with traditional binary PRBS based random mixing. DCF: Dispersion Compensating Fibre, CFBG: Custom Fibre Bragg Grating, EDFA: Erbium Doped Fibre Amplifier, MZM: Mach-Zehnder Modulator, SMF: Single Mode Fibre, PRBS: Pseudo Binary Random Sequence, PD:Photo Detector.

Each chirped waveform carrying strain information is mixed with a set of pseudo-random bit sequences (PRBS) in the digital domain at a bit rate of 20 Gbps and fully compressed to form one element of the resultant measurements. The measurements can be down-sampled at 50 MHz, which not only reduces the bandwidth requirement for the photodetector and digitiser but also compresses the overall data size. With the knowledge of PRBS sequence and the measurements, the original chirped signal can be reconstructed from compressed data set using L1 minimisation [47]. As joint work, data compression in high-throughput Photonic Time-Stretch based CFBG strain sensing has been analysed and experimentally demonstrated using Compressive Sensing method. A data compression ratio of 62.5% has been obtained in high-throughput applied strain measurements with 1.51 MHz axial scan rate and a sampling rate of 50 MS/s.

An application example as shown in Figure 3.10 (a) where it can be observed that the wideband signal captured has 6 GHz as maximum frequency with 6 GHz bandwidth. The spectrogram is shown in Figure 3.10 (b) showing downward chirp from few GHz to MHz. A binary PRBS is generated with 20Gbps bit rate or 50ps bit period making the signal length N=400. Two such sequences each with length 400 are shown in Figure 3.10 (c) and corresponding electro-optically mixed signal is shown in Figure 3.10 (d). The sensing signal is mixed with m number of PRBS sequences each of length *N*, 400, and are optically integrated to represent a single measurement which can be captured at 50 MHz speed. The sensing signal can be reconstructed using L1 minimization algorithm. Solving the minimization problem

$$\hat{X} = \arg\min \|v\|_{l_1} \quad \text{subject to} \quad Av = Y \tag{3.13}$$

where $\|v\|_{l_1}$ indicates that the number of nonzero entries in vector **v**. **X** is a N × 1 matrix representing the input sparse information with a data length of N, **Y** is a m × 1 matrix denoting the measured results, m is the number of measurements, **A** is the measurement matrix, has a dimension of m × N, is defined as **A=DIR**, in which matrix **D** is a m × N matrix denoting a down sampling process, **I** is a N × N matrix indicating the low-pass filter response, **R** is a diagonal N × N matrix denoting a random sequence. Since information length is known and the transformation domain in which the information signal is sparse, can be reconstructed. The compression ratio is defined as *m/N*.

The proposed all-optical random pattern generation based FBG sensing works best if the patterns generated are stable and reproducible. Containing the optical phase and constant polarization is of crucial importance in this process. This can be mitigated if a compact and miniaturized setup with silicon photonics chip instead of discrete elements where the Mode locked laser and cascaded MZI setup can be reduced in foot print with SMF replaced with chirped FBG grating producing same dispersion as DCF used in this setup. Initial research focussed towards photonic integrated circuits has shown promising results [48].

With 250 measurements, a compression ratio of 62.5 %, the spectrogram is shown in Figure 3.11 (e). As can be observed from Figure 3.11 (e), the downward chirp can be easily recognized and the chirp slope determines the strain induced in the sensing FBG with respect to reference FBG.

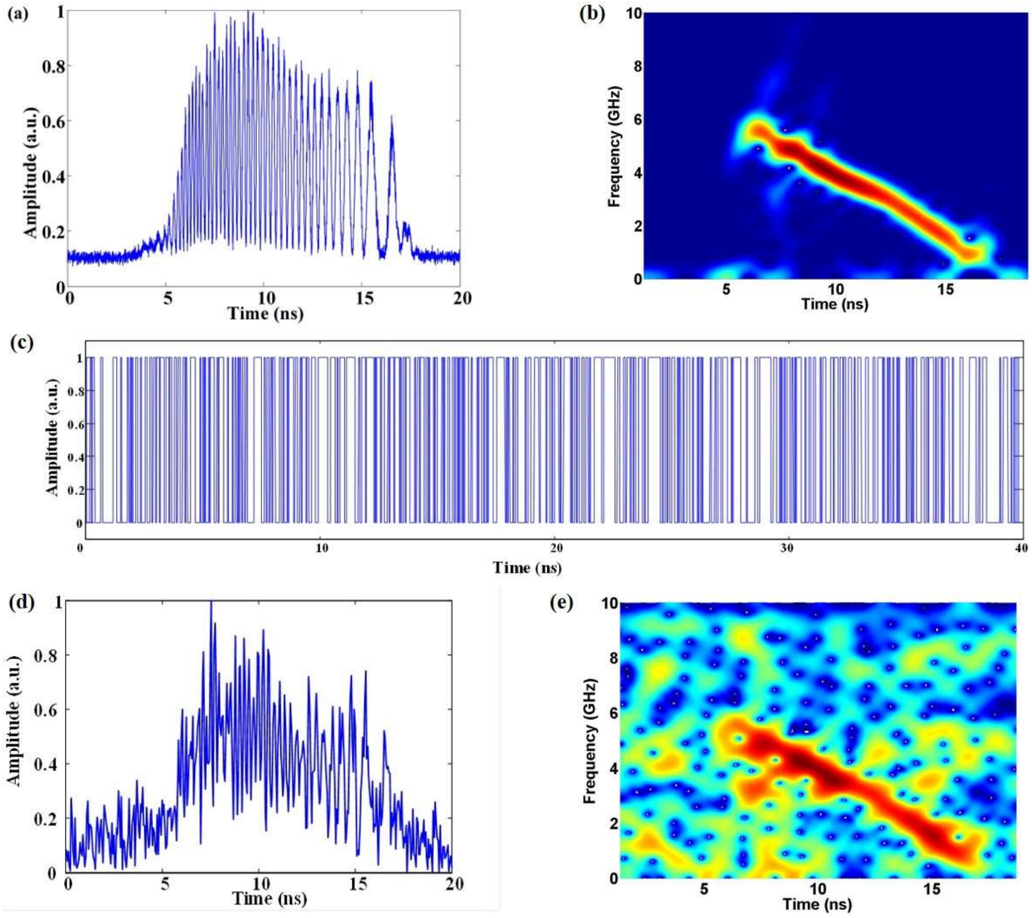

Figure 3.10 (a) Original time stretched sensing signal in time domain. (b) Spectrogram of the sensing signal showing linear frequency chirp (c) Two PRBS sequences used for mixing (d) Mixed signal with PRBS and sensing signal. Time domain reconstruction of sensing signal upon L1 reconstruction with 62.5% compression ratio (e) Spectrogram showing clear chirp profile.

3.8 Summary

The measurement of non-uniform local strain gradient sensing systems have application in monitoring structural damage where the form of the strain field is expected to change continuously. Real time structural dynamics near high-stress hot-spots such as contact points. Material properties such as stiffness and dynamic structural disbond can be actively studied. Since the same system concept can be applied to temperature sensing. This technique may suit applications wherein rapid monitoring of temperature distribution is required such as monitoring cancereous tissue during shock therapy. In this chapter, the concept of dispersion enabled frequency to time mapping has been utilised for translating spectral response of fibre grating sensors to the temporal domain that can be processed in real-time using state-of-the-art electronics based detection.

Proof of concept experiments and theoretical analysis demonstrating ultrafast and ultrahigh-resolution interrogation of chirped Fibre Bragg grating sensors response to variations in strain are investigated. The ability of chirped fibre Bragg gratings to obtain strain information continuously over its length when a non-uniform strain is applied to the grating is proposed. Two chirped fibre Bragg gratings, grating length 25 mm and grating bandwidth 7 nm are employed in a Michelson interferometer set up. One grating serves as the reference grating free from any strain whereas the sensing grating is subjected to both uniform and non-uniform strain. A tunable delay line is inserted in one of the paths. A mode-locked laser generates broadband coherent pulses directed to the Michelson interferometer structure. Reflected spectra from individual gratings are combined and mapped to time based on photonic dispersive Fourier transformation implementing a temporal interference pattern. Sensing information encoded in the spectrum is converted to a microwave pulse. Monitoring the instantaneous frequency along time for the generated microwave pulses enables non-uniform strain measurement at an ultrafast rate and ultrahigh-resolution. The concept was extended to crack location along the plastic ply supporting the chirped fibre Bragg grating.

In the following chapter, the proposed application concept is extended to explore non-contact measurement using mode-locked laser pulses as the probe beam employed in an interferometric architecture. Depth information is encoded in the Free Spectral Range (FSR) which is translated to time based on the photonic Time-Stretch principle. Ultimately, IR transparent samples can be geometrically characterised by analysing the instantaneous microwave frequency detected in time.

REFERENCES

[1] K. O. Hill, B. Malo, F. Bilodeau, D. C. Johnson, and J. Albert, "Bragg Gratings Fabricated in Monomode Photosensitive Optical-Fibre by UV Exposure through a Phase Mask," *Applied Physics Letter,* vol. 63, no. 3, pp. 424-424, 1993.

[2] K. O. Hill and G. Meltz, "Fibre Bragg grating technology fundamentals and overview," *IEEE J. Lightwave Technology,* vol. 15, no. 8, pp. 1263-1276, 1997.

[3] R. Kashyap, P. F. McKee, R. J. Campbell and D. L. Williams, "Novel method of producing all fibre photo induced chirped gratings," *Electronics Letters,* vol. 30, pp. 996-998, 1994.

[4] W. Yuan, A. Stefani and O. Bang, "Tunable Polymer Fibre Bragg Grating (FBG) Inscription: Fabrication of Dual-FBG Temperature Compensated Polymer Optical Fibre Strain Sensors," in *IEEE Photonics Technology Letters*, vol. 24, no. 5, pp. 401-403, 2012.

[5] M. C. Farries, K. Sugden, D.C. J. Reid , I. Bennion, A. Molony and M. J. Goodwin, “Very Broad reflection bandwidth (44nm) chirped fibre gratings and narrow bandpass filters produced by the use of an amplitude mask,” *Electronics Letters*, vol. 30, pp. 891-892, 1994.

[6] Sugden, I. Bennion, a. Moloney and N. J. Copner, "Chipred grating produced in photosensitive optical fibres by fibre deformation during exposure," *Electronics Letters,* vol. 30, pp. 440-441, 1994.

[7] Y. Painchaud, A. Chandonnet and J. Lauzon, "Chirped fibre gratings produced by tilting the fibre," *Electronics Letters,* vol. 31, pp. 171-172, 1995.

[8] Z. Wei, L. Qin, H. Li, Q. Wang, W. Zheng and Y. Zhang, "Fabrication of high quality chirped fibre Bragg grating by establishing strain gradient," *Optical and Quantum Electronics,* vol. 33, pp. 55-65, 2001.

[9] C. Wang, "Dispersive Fourier transformation for versatile microwave photonics applications," in *Photonics, Multidisciplinary Digital Publishing Institute*, 2014.

[10] M. A. Muriel, J. Azaña and A. Carballar, "Real-time fourier transformer based on fibre gratings," *Optics letters,* vol. 24, no. 1, pp. 1-3, 1999.

[11] C. Wang and J. Yao, "Photonic generation of chirped microwave pulses using superimposed chirped fibre Bragg gratings," *IEEE Photonics Technology Letters,* vol. 20, no. 11, pp. 882-884, June 2008.

[12] C. Wang and J. Yao, "Chirped microwave pulse generation based on optical spectral shaping and wavelength-to-time mapping using a sagnac loop mirror incorporating a chirped fibre bragg grating," *Journal of Lightwave Technology,* vol. 27, no. 16, pp. 3336-3341, 2009.

[13] Luciano Mescia and F. Prudenzano, "Advances on optical fibre sensors," *Fibres,* vol. 2, no. 1, pp. 1-23, 2014.

[14] A. D. Kersey, M. A. Davis, H. J. Patrick, M. LeBlanc, K. P. Koo, C. G. Askins, M. A. Putnam and E. J. Friebele, "Fibre grating sensors," *Journal of Lightwave Technology,* vol. 15, no. 8, pp. 1442-1463, August 1997.

[15] D. Kinet, P. Mégret, K. Goossen, L. Qiu, D. Heider, and C. Caucheteur, "Fibre Bragg Grating Sensors toward Structural Health Monitoring in Composite Materials: Challenges and Solutions," *Sensors,* vol. 14, pp. 7394, 2014.

[16] H. J. Bang, S. M. Jun and C. G. Kim, "Stabilized interrogation and multiplexing techniques for fibre Bragg grating vibration sensors," *Measurement Science and Technology,* vol. 16, no. 3, p. 813, 2005.

[17] W. Ecke, I. Latka, R. Willsch, A. Reutlinger and R. Graue, "Fibre optic sensor network for spacecraft health monitoring," *Measurement Science and Technology,* vol. 12, no. 7, p. 974, 2001.

[18] Y. Okabe, R. Tsuji and N. Takeda, "Application of chirped fibre Bragg grating sensors for identification of crack locations in composites," *Composites Part A: applied science and manufacturing,* vol. 35, no. 1, pp. 59-65, 2004.

[19] W. Liu, M. Li, C. Wang and J. Yao, "Real-time interrogation of a linearly chirped fibre Bragg grating sensor based on chirped pulse compression with improved resolution and signal-to-noise ratio," *Journal of Lightwave Technology,* vol. 29, no. 9, pp. 1239-1247, 2011.

[20] S. H. Yun, D. J. Richardson, and B.Y. Kim, “Interrogation of fibre grating sensor arrays with a wavelength-swept fibre laser”, *Optics Letters*, vol. 23 no. 11, pp. 843–845, 1998.

[21] M. L. Dennis, M. A. Putnam, J.U. Kang, T. E. Tsai, I. N. Duling and E. J. Friebele, "Grating sensor array demodulation by use of a passively mode-locked fibre laser," *Optics Letters,* vol. 22, no. 17, p. 1362–1364, 1997.

[22] A. D. Kersey, T. A. Berkoff and W. W. Morey, "Multiplexed fibre Bragg grating strain-sensor system with a fibre fabry–perot wavelength filter," *Optics Letters,* vol. 18, no. 16, pp. 1370-1372, August 1993.

[23] D. Chen, C. Shu and S. He, "Multiple fibre Bragg grating interrogation based on a spectrum-limited fourier domain mode-locking fibre laser," *Optics letters,* vol. 33, no. 13, pp. 1395-1397, 2008.

[24] J. Yao, "Microwave photonics for high-resolution and high-speed interrogation of fibre Bragg grating sensors," *Fibre and Integrated Optics,* vol. 34, no. 4, pp. 204-216, 2015.

[25] H. Y. Fu, H. L. Liu, X. Dong, H.Y. Tam, P. K. A. Wai, and C. Lu. "High-speed fibre Bragg grating sensor interrogation using dispersion compensation fibre," *Electronics Letters,* vol. 44, no. 10, pp. 618-619, 2008.

[26] C. Wang and J. Yao, "Ultrafast and ultrahigh-resolution interrogation of a fibre Bragg grating sensor based on interferometric temporal spectroscopy," *Journal of Lightwave Technology,* vol. 29, no. 19, pp. 2927-2933, 2011.

[27] E. J. Jung, C. S. Kim, M. Y. Jeong, M. K. Kim, M. Y. Jeon, W. Jung and Z. Chen, "Characterisation of fbg sensor interrogation based on an FDML wavelength swept laser," *Optics Express,* vol. 16, no. 21, pp. 16552-16560, 2008.

[28] C. R. Giles, "Lightwave applications of fibre Bragg gratings," *IEEE J. Lightwave Technology,* vol. 15, no. 8, pp. 1391-1404, 1997.

[29] J. Capmany, D. Pastor, B. Ortega, J. L. Cruz and M. V. Andres, "Applications of fibre Bragg gratings to microwave photonics (Invited paper)," *Fibre and Integrated Optics,* vol. 19, no. 4, pp. 483-494, 2000.

[30] L. Mohanty, L. M. Koh and S. C. Tjin, “Fiber Bragg grating microphone system” Applied Physics Letters, vol. 89, no. 16, pp. 161109, 2006.

[31] D. R. Solli, J Chou and B. Jalali, "Amplified wavelength–time transformation for real-time spectroscopy," *Nature Photonics,* vol. 2, no. 1, pp. 48-51, 2008.

[32] K Goda and B Jalali, "Dispersive Fourier transformation for fast continuous single shot measurements," *Nature Photonics,* vol. 7, no. 2, pp. 102-112, 2013.

[33] P. V. Kelkar, F. Coppinger, A. S. Bhushan and B. Jalali, "Time-domain optical sensing," *Electronics Letters,* vol. 35, no. 19, pp. 1661-1662, 1999.

[34] J. Chou, Y. Han and B. Jalali, "Time-wavelength spectroscopy for chemical sensing," *IEEE Photon Technologies Letters,* vol. 16, no. 4, pp. 1140-1142, 2004.

[35] G. Rodriguez, M. Jaime, F. Balakirev, C. H. Mielke, A. Azad, B. Marshall, B. M. L. Lone, B. Henson and L. Smilowitz, "Coherent pulse interrogation system for fibre Bragg grating sensing of strain and pressure in dynamic extremes of materials," *Optics express,* vol. 23, no. 11, pp. 14219-14233, 2015.

[36] J. Wang, Z. Liu, C. Ge, Y. Yu, Y. Zhang, X. D. Z. Li and K. S. Chiang, "Measurement of broadband fibre-grating transmission spectrum using tunable fibre-grating ring laser," in *Optical and Fibre Optical Sensor Systems, Proceedings SPIE 3555*, 1998.

[37] J. Gan, Y. Hao, Q. Ye, Z. Pan, H. Cai and Z. F. R. Qu, "High spatial resolution distributed strain sensor based on linear chirped fibre Bragg grating and fibre loop ring down spectroscopy," *Optics letters,* vol. 36, no. 6, pp. 879-881, 2011.

[38] K. Anubhuti, "Design and Study of Chirped Fibre Bragg Grating for Sensing of Hazardous Gases," *(2011) International Journal of Computer Aplications,* vol. 23, no. 9, pp. 40-43, 2011.

[39] S. Komatsuzaki, "Development of small-diameter optical fiber sensors and high-speed optical wavelength interrogator for damage detection in composite materials" *Proceedings SPIE*, 6167, pp. 54-61, 2006.

[40] A. L. Ricchiutu, D Barrera, S Sales, L. Thevanaz, J. Capmany, "Microwave Photonics filtering for interrogating long weak Fiber Bragg grating sensors,", *23rd International Conference on Optical Fibre Sensors*, 2014.

[41] Y. Shigeki, W. Jumpei, and S. Yoshihisa, "A monitoring technique for disbond area in carbon fibre–reinforced polymer bonded joints using embedded fibre Bragg grating sensors: Development and experimental validation," *Structural Health Monitoring,* vol. 16, pp. 185-201, 2017.

[42] R. S. Brown, I. Kozin, R. D. O. Z. Tong and H. P. Loock, "Fibre-loop ring-down spectroscopy," *The Journal of Chemical Physics,* vol. 117, no. 23, pp. 10444-10447, 2002.

[43] M. Volanthen, H. Geiger and J. P. Dakin, "Distributed grating sensors using low-coherence reflectometry," *Journal of Lightwave Technology,* vol. 15, no. 11, pp. 2076-2082, 1997.

[44] H. Murayama, H. Igawa, K. Kageyama, K. Ohta, I. Ohsawa, K. Uzawa, M. Kanai, T. Kasai and I. Yamaguchi, "Distributed strain measurement with high spatial resolution using fibre Bragg gratings and optical frequency domain reflectometry," in *Optical Fibre Sensors, OSA Technical Digest (CD) (Optical Society of America, 2006), paper ThE40*, 2006.

[45] Y. Barbarin, "Dynamic measurements of physical quantities in extreme environment using fibre Bragg grating," *2017 25th Optical Fibre Sensors Conference (OFS)*, Jeju, pp. 1-4, 2017.

[46] C. K. Mididoddi, G. Wang, and C. Wang, "Data Compressed Photonic Time-Stretch Optical Coherence Tomography", in *IEEE Photonics Conference (IPC)*, Waikoloa, Hawaii, USA, 2-6 Oct. 2016.

[47] C. K. Mididoddi, E. J. Ahmad and C. Wang, "Data-efficient high-throughput fibre Bragg grating sensors using photonic time-stretch compressive sensing", *Conference on Lasers and Electro-Optics Europe (CLEO-Europe)*, Munich, Germany, 25-29 June 2017.

[48] Z. Weifeng, Z. Jiejun, and Y. Jianping, "Largely chirped microwave waveform generation using a silicon-based on-chip optical spectral shaper," in *Microwave Photonics (MWP) and the 2014 9th Asia-Pacific Microwave Photonics Conference (APMP), 2014 International Topical Meeting on*, pp. 51-53, 2014.

[49] Y. Mizuno, W. Zou, Z. He, and K. Hotate, "Proposal of Brillouin optical correlation-domain reflectometry (BOCDR)," *Optics Express*, vol. 16, no. 16, pp. 12148–12153, 2008.

[50] J. HervÃas, A. L. Ricchiuti, W. Li, N. H. Zhu, C. R. FernÃandez-Pousa, S. Sales, M. Li and J. Capmany, "Microwave photonics for optical sensors," *IEEE Journal of Selected Topics in Quantum Electronics,* vol. 23, no. 2, pp. 327-339, March 2017.

CHAPTER 4

HIGH THROUGHPUT INTERFEROMETRY APPLIED TO DIMENSIONAL METROLOGY OF IR TRANSPARENT SAMPLES

4.1 Introduction

Chapter 3 presented the use of CFBG based strain interrogation scheme to obtain intra-grating, temperature independent, high-speed and high-resolution strain detection. Using this sensing technology enables the possibility of obtaining fibre-based real-time high-speed vibration measurement and structural health monitoring with high temporal resolution.

In this chapter, an extension of the proposed technique is implemented to obtain non-invasive, high-speed dimensional metrology of infrared transparent samples. Dimensional metrology implies quantification of size, position and displacement in space [1]. Michelson interferometer based photonic microwave pulse detection is carried out to capture sample thickness information encoded in the generated microwave frequency signal. A calibration scheme is proposed wherein the generated microwave frequency signal after the introduction of IR transparent sample in the measurement system is compared to a reference microwave pulse. The comparison and average frequency difference over time enable thickness measurement, and the instantaneous frequency over time reveals surface profile fluctuation and thus depth difference fluctuation and estimation over the spectral bandwidth scanning the surface profile. The aim is to demonstrate that the proposed microwave detection scheme can achieve high throughput measurement and the application concept can be improved upon and extended to benefit a myriad of real-time dynamic monitoring industry tools [2, 3]. Since a demonstration of IR transparent glass samples is presented, utility in thin film sensing is proposed. Measuring thin films such as photoresist directly on glass or plastic substrate without damaging the coating is common practice [4]. Similarly, Process control and Quality Assurance practices rely on inline non-contact dimensional metrology of plastics. Conveyer belts and axial scan rates need to be optimized to obtain maximum industrial throughput.

A novel, proof of concept experimental and theoretical analysis demonstrating ultrafast and ultrahigh-resolution infrared transparent plate thickness measurement technique is investigated. A photonic evaluation technique enabling dispersive Fourier transformation [5, 6], translating spectral interference into a scaled replica in the temporal domain is utilised to generate microwave pulses after photodetection. Dispersive ultrashort pulses from a mode-locked laser are employed in a Michelson interferometry set up. One arm acts as the reference arm, and an infrared transparent plate such as microscope slides of variable thickness are employed in the sample arm. A mode-locked laser generates broadband coherent pulses, which are directed to the Michelson interferometer structure. Reflected spectra from individual arms are combined and mapped to time based on photonic dispersive Fourier transformation implementing a temporal interference pattern. Plate thickness information encoded in the spectrum is converted into a time domain microwave pulse. Monitoring the instantaneous frequency along time for the generated microwave pulses with reference to a calibration phase microwave pulse enables plate thickness estimation at an ultrafast rate and high temporal resolution.

4.2 Problem Statement

Research presented was initiated after path length difference in a Michelson interferometer were identified as change in FSR and mapped to a microwave frequency at a photodetector using Mode-locked laser pulses and Dispersion compensating fibre mapping spectral interference to temporal profile. During experimentation, a mode locked laser was employed as the source and directed to a Michelson interferometer structure with a tunable time delay in one arm. The output interference signal was analysed at a photodetector. A dispersion compensating fibre maps the spectral intensity to its temporal replica. By measuring known perfect displacements, the goal was extended to demonstrate optical path length differences by measuring thickness of transparent samples introduced in one of the interferometer arms.

The capability of microwave photonics-based high-speed spectroscopic measurement and manipulation is the strongest motivation to develop a real-time non-contact dimensional metrology tool for development of novel solutions and unexplored future applications. Many researchers have utilised several methods for thin film sensing; dimensional metrology, surface profilometry and vibration analysis [7 – 10], however a complex signal processing requirement and hardware employed for advanced dimensional metrology applications limit high-speed solutions. In the advancement of optical systems, the metrology of the elements of optical components is basic, as any dimensional blunder in the state of the optical surface or the thickness of the optical component corrupts the planned performance of the overall optical system [11 - 13].

4.3 State-of-the-art in Non-Contact Dimensional Metrology

A number of industrial engineering applications are oriented towards surface inspection, surface characterisation, and dimensional metrology. Uncertainty in high precision manufacturing deems surface inspection technology for quality engineering and assurance practices very useful. Contact methods such as micrometre gauges for thickness measurement though have high resolution but are potentially destructive and may damage delicate components. Similarly, the thickness of the sample is usually not constant across the entire sample. Surface profiling, enabling evaluation of surface roughness and measure of flatness, biomedical; serial time-encoded amplified microscopy, allowing high throughput cancer cell detection in real-time, non-invasive inspection of paint on car and aeroplane bodies, packaging of electronics material and thin film sensing, and coherence tomography [14 - 17] require inline dynamic measurement system, that continuously inspects material thickness as it is processed. Single wavelength phase shifting interferometry has become the most common type of interferometry for surface thickness measurements. By introducing a time-varying phase shift between the reference and test wavefronts, the interferograms with difference reference phases can be captured sequentially [18]. Multiple wavelengths with relatively small wavelength differences are also employed to create a synthetic wavelength, the interference phase or phase spectrum of the synthetic wavelength calculated using phase shifted interferometry is related to the optical path length difference. Low coherence interferometry is also widely employed; broadband source directed to a Michelson interferometer with sample arm consisting of sample under test creates an interference pattern when path length difference matches coherence length of the source. This allows localisation of where the signal is coming from and thus depth estimation. Surface and thickness measurement of a transparent film using wavelength scanning interferometry [19] have achieved depth resolution as good as 5 µm with scan speed limited by tuning speed of the laser employed.

Surface metrology can be broadly divided into dimensional metrology and surface topography. Dimensional metrology is essentially the analysis of the holistic thickness of the sample under test whereas surface topography is a measure of the roughness and smoothness of the surface, the deviation in surface profile over length. High precision surface characterisation techniques for state-of-the-art engineered materials benefit from non-contact measurement schemes as high-cost is associated with manufacturing such products; for instance, microelectronic components fabricated are fragile and destructive techniques for surface inspection cannot be risked. Semiconductors and material engineering require thin film coating to provide specific capabilities. In addition, real-time, dynamic monitoring mechanism is crucial in packaging and quality assurance and inspection of for instance food item packaging on a large scale. A rapid advance in laser scanning technology implies that future quality engineering and assurance practices will rely heavily on contactless vibration sensing and surface roughness or flatness profiling. Thus, an ever-increasing need for the development of a real-time solution to non-invasively extract surface metrology information is felt. The exploration of techniques that can enable ultra-high precision surface metrology for state-of-the-art free-form lens surfaces in future mobile phones, tablets, miniaturised astronomical telescopes, eye glasses and LCDs.

Traditional laser ranging and vibration sensing techniques can generally be classified into time and spectral domain measurement [20 - 22]. An enhanced temporal resolution could lead to limited spatial resolution, and enhanced spatial resolution suffers from a narrow inquisition time [23]. Conventional non-contact measurement schemes rely heavily on spectroscopic techniques, limiting real-time measurement capability and thus considered as offline processes [24 - 26].

Microwave photonics encapsulates the border area between electronics and photonics and is an emerging field with substantial future industrial potential [27]. Novel techniques realising the generation of microwave signals based on optical techniques have been accomplished [28, 29] including the generation of microwave photonic pulses based on temporal interferometry [30]. However, applying the concept of photonic microwave measurement to extract geometrical parameters such as thickness and or refractive index of material under investigation from optical path length has not been investigated according to the best of my knowledge. The current system is limited in decoupling refractive index from sample thickness; one or the other should be known for either thickness or refractive index measurement. Thickness is a prerequisite for other optical properties (such as transmission, absorption and reflection) when characterizing components and materials.

4.4 Experimental Setup & Measurement Results

This section describes the experimental setup for the IR transparent sample thickness profiling. Measurements were repeated for samples ranging from thin film Mylar to glass slides and Mylar-glass and glass-glass combination. A calibration phase was set up to determine the initial microwave frequency, and subsequent signal frequencies generated referenced to the calibration signal. Post-processing enables surface thickness estimation.

A novel application concept enabling surface profiling and metrology using microwave photonic techniques that achieves simultaneous high temporal and spatial resolution, sample thickness measurement, based on translating spectrum information to the corresponding time domain waveform utilising the concept of frequency-to-time mapping and frequency-to-space mapping [31, 32] is proposed. High temporal resolution is assured due to high sampling rate of the digitizer, which also limits the spectral resolution related to the spatial resolution. The experimental setup consists of two identical reflective mirrors employed in a Michelson interferometer architecture. A short pulse with a broadband spectrum (8 nm at a drive current of 800 mA). from a femtosecond pulse laser is directed into an optical circulator. The output from Port 2 of the optical circulator is directed to a diffraction grating that disperses the light, which performs the one-to-one frequency-to-spatial mapping. The diffracted light is directed to a beam splitter that divides the diffracted beam into two paths. As an initial calibration step, a fixed time delay is introduced between the two arms in the Michelson interferometer and the corresponding spectral interference mapped to a temporal signal which is a microwave pulse with a uniform frequency determined by the initial time delay introduced between the two arms of the interferometer based on the principle of dispersive Fourier transformation [23]. In the second stage, the diffracted beam in one arm is directed to an IR transparent sample such as Glass (BK-7) or thin film plastic (mylar) fixed in the sample arm with different wavelengths mapped onto different positions in the x-dimension. The introduction of a sample in one of the arm leads to the addition of a phase factor due to material characteristics and thus an additional delay in the path of laser pulse traversing the interferometer structure. The broadband Wavelength-dependent free spectral range (FSR) is dependent upon the temporal separation between the two pulses recombining and collected at port 3 of the circulator. A schematic of the proposed measurement is depicted in Figure 4.1. In the proposed measurement scheme, the target spectral interferogram is mapped to a temporal interference waveform that can be captured in real-time using a high-speed single-pixel photo-detector. Therefore, ultrafast and single-shot measurement is achieved with measurement speed identical to the repetition rate of the pulsed laser. The distributed thickness information along the spot size of the diffracted beam is reconstructed from the instantaneous microwave frequency of the captured waveform by applying short-time Fourier transform (STFT) analysis. High-spatial resolution is also obtained thanks to high-speed data acquisition. Note that although a similar laser scanning setup has been used in a previous system [3, 8, 16], the application of extracting geometrical and dielectric properties information from infrared transparent thin plate samples by decoding the frequency of the microwave pulse has not been demonstrated. Here we achieve an ultrafast measurement scheme enabling peak to peak pulse delay difference through free space and IR transparent sample by applying time/space resolved STFT analysis to the generated microwave pulse. Ultrafast real-time measurement of glass slides (BK-7) of various thickness and thin films such as Mylar samples at a measurement speed of 50 MHz with a lateral resolution of 12.5 µm over a beam width or beam profile of 3.83 mm.

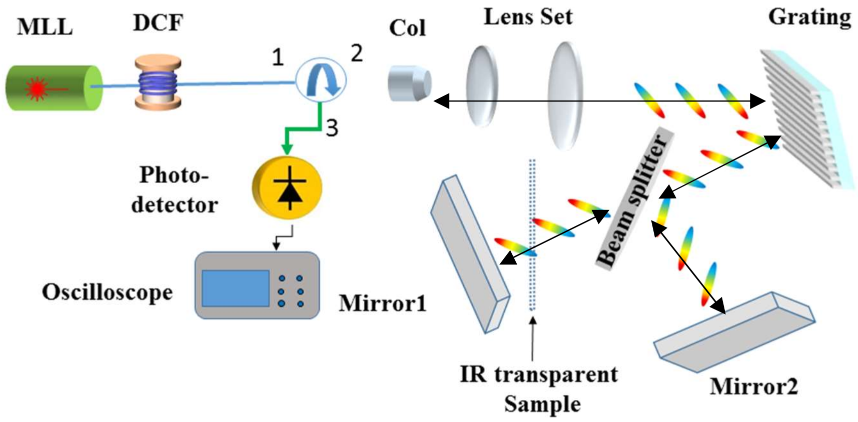

Figure 4.1 The proposed IR transparent samples geometrical and dielectric properties measurement scheme. Fibre to space and space to fibre coupling introduced and Michelson interferometry set up employed, spectral interference mapped to temporal waveform using dispersive Fourier transformation. MLL: mode-locked laser, DCF: -dispersive compensating fibre, Col: collimator.

In the set up depicted in Figure 4.1, a passive mode-locked laser (MLL) is used to generate highly-coherent ultrashort optical pulses with a broad optical spectrum (8nm at 800 mA drive current). The optical pulse is first stretched by a dispersion compensating fibre (DCF) and then sent to the Michelson interferometer. An optical time-stretch frequency domain reflectometry is thus formed, and the spectral interferogram is mapped to a temporal interference waveform thanks to dispersion-induced wavelength-to-time mapping, also known as dispersive Fourier transform. The central frequency of the mapped temporal waveform is determined by the initial time delay, τ and the overall chromatic dispersion $\ddot{\Phi}$ (in ps^2) of the DCF, which is given by

$$f_{RF} = \frac{\tau}{\ddot{\Phi}} \tag{4.1}$$

This constitutes the calibration phase where the signal frequency is determined from the initial parameters set. The temporal waveform and corresponding spectrogram and instantaneous frequency are obtained by applying the STFT. When a sample material such as glass slides (BK-7) of variable thickness or ultra-thin Mylar film are introduced in one of the interferometer arms, an additional time delay, $\Delta\tau$ due to change in speed of propagation of incident laser pulse within the medium is given by

$$\Delta\tau = \tau - \tau_0 = \frac{2d}{c/\eta} - \frac{2d}{c}$$
$$d = \frac{c\Delta\tau}{2(\eta - 1)} \tag{4.2}$$

Where τ_0 is the time delay between interferometer arms without any sample under test, τ is the time delay between interferometer arms with material sample in the sample arm, c is the speed of light in air, and η is the refractive index of material under test. This extra temporal shift $\Delta\tau$ is added to the overall time delay between two interferometer arms and leads to the change of instantaneous RF frequency, $\Delta f_{RF}(t)$ in the temporal interference waveform. The difference in RF frequency captured can be related to the optical path length of the material under investigation or the geometrical thickness of the sample if the refractive index is known.

To verify the utility of the proposed technique, a proof-of-concept experiment based on the setup shown in Figure 4.1 is performed. A passively mode-locked fibre laser (Calmar MENDOCINO FPL) is employed as the optical source to generate a transform-limited Gaussian pulse train with a repetition rate of 50 MHz. The ultrashort optical pulse has a full-width at half-maximum (FWHM) pulse width of 800 fs, a 3-dB spectral bandwidth of 6.1 nm and a central wavelength of 1551 nm. Two identical mirrors are employed in both the sensing and reference arms. An initial delay in the sensing arm of the interferometer to establish a reference point for plate thickness measurements is implemented. A DCF with total group velocity dispersion (GVD) of $\ddot{\Phi}$ = 5280 ps^2 is used for optical time-stretch process. The mapped temporal interference waveform is detected by a 45 GHz photodetector and recorded using a high-speed real-time oscilloscope.

A calibration phase signal, wherein no sample is placed in one of the interferometer arms, a predetermined time delay equivalent to approximately 47.2 ps is introduced, and a microwave single tone pulse train is obtained at the output. A schematic of the temporal signal at the output of a 45 GHz PD, analysed with a real-time oscilloscope is depicted in Figure 4.2.

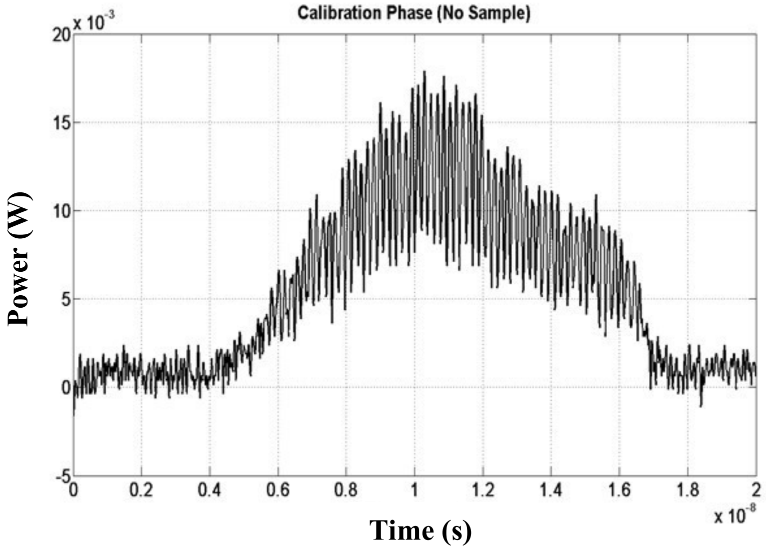

Figure 4.2 Measured basic system calibration response depicting generated microwave pulse when no sample is introduced in sample arm.

The instantaneous frequency and instantaneous phase of the output signal obtained from Hilbert transform of raw data are depicted in Figure 4.3.

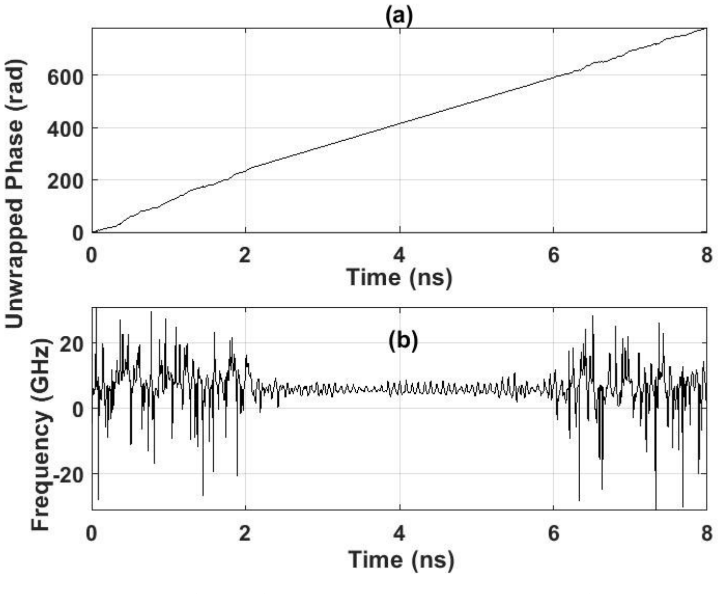

Figure 4.3 (a) Instantaneous Phase (b) Instantaneous frequency along time as derived from the Hilbert transform of the raw data.

Figure 4.4 depicts the corresponding interferogram for the calibration phase microwave signal obtained at the photodetector. The y-axis on the right relates the frequency recorded to the corresponding optical path length difference between interferometer arms.

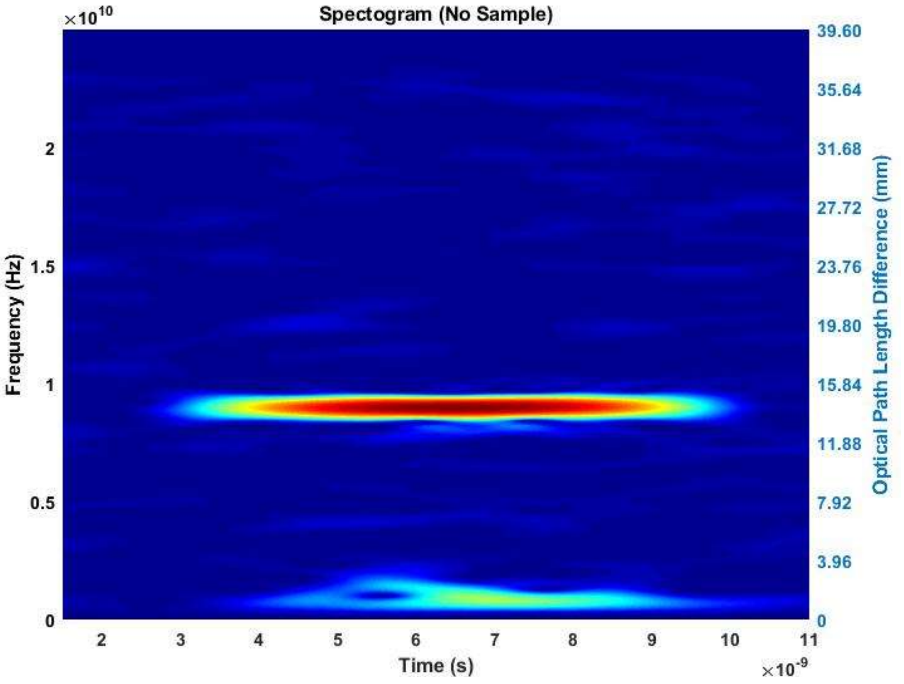

Figure 4.4 Spectogram. Visual representation of the spectrum of frequencies of calibration phase signal as it varies with time.

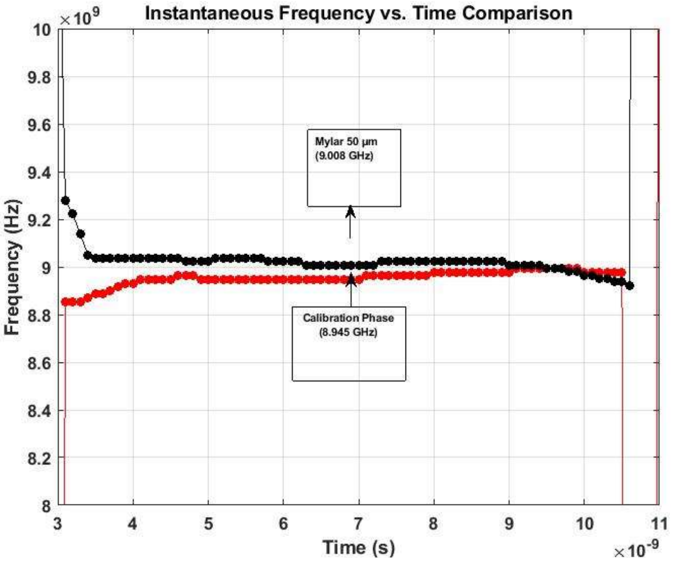

Figure 4.5 Instantaneous frequency comparison over time from spectrogram of calibration phase signal and 50 μm mylar sample. A change in optical path length of the interferometer with the introduction of a mylar sample in the interferometer can be estimated from the instantaneous change in microwave frequency of signal recorded at photodetector.

As a test case, 50 μm of mylar is introduced in the sample arm. A comparison of the instantaneous frequency versus time for the generated microwave signal is compared to the calibration phase as shown in Figure 4.5.

A frequency jump of 65 MHz matches very closely to theoretical prediction as highlighted in Equation 4.2. Figure 4.6 depicts the corresponding microwave signal generated when a mylar sample is introduced in the sample arm.

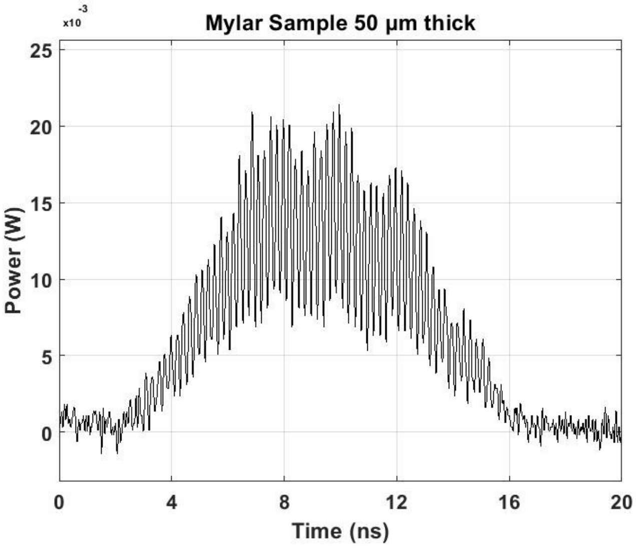

Figure 4.6 The measured system performance with mylar sample placed in one of the interferometer arms. The microwave pulse recorded at the photodetector when thin film Mylar (50 μm) sample is introduced is depicted.

Introduction of a thin film mylar sample results in another signal at the photodetector with a uniform instantaneous frequency as shown in Figure 4.7.

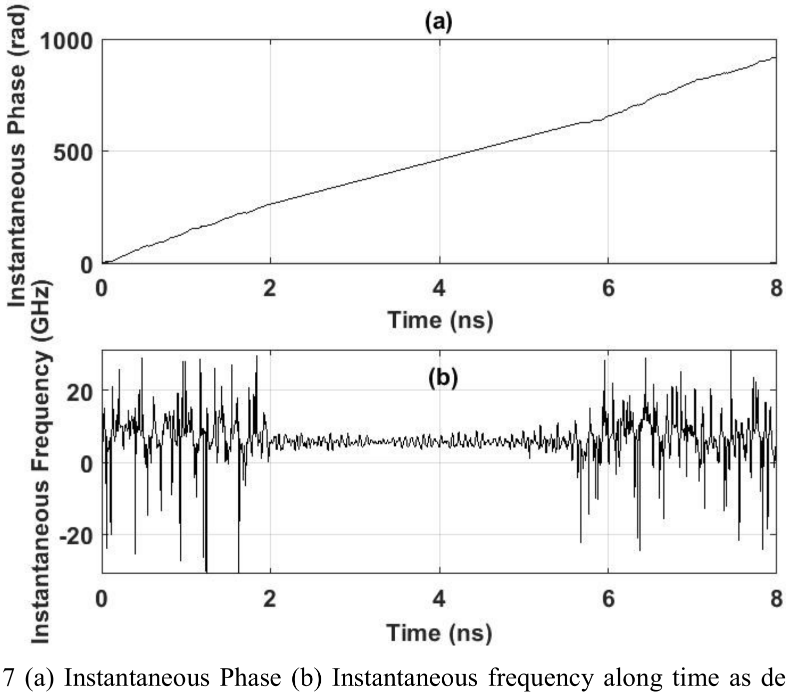

Figure 4.7 (a) Instantaneous Phase (b) Instantaneous frequency along time as derived from the Hilbert transform of the raw data.

Hilbert transform of the raw data and a measure of the instantaneous frequency based on derivative of instantaneous phase information reveal a frequency change in the output signal, the corresponding spectrogram is shown in Figure 4.8.

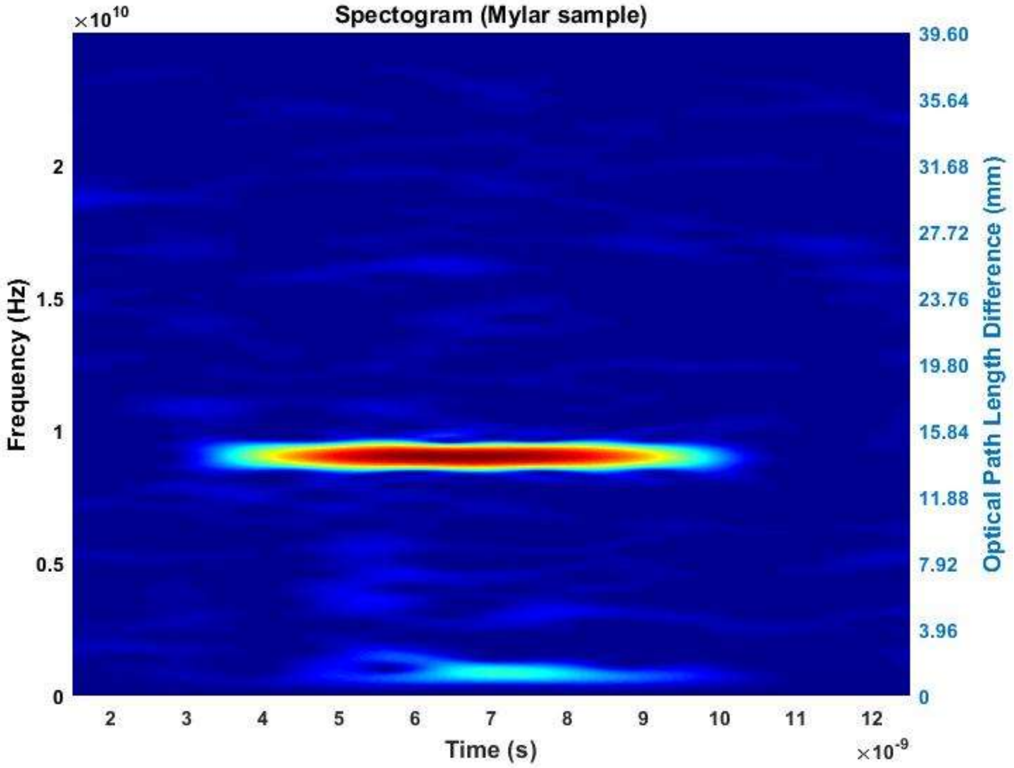

Figure 4.8 Spectrogram of microwave signal when mylar sample is introduced in one of the interferometer arms.

A. Thin Film and IR Transparent Plate Thickness Measurement

A frequency jump of 65 MHz observed in the generated microwave pulse for a 50 μm sample demonstrates high sensitivity of the technique enabling precise depth information to be encoded in a significant frequency deviation in the time domain. Similarly, experimental results are performed for transparent glass sample (BK-7) of various thicknesses. The instantaneous frequency and spectrogram of the acquired results are displayed in the following figures. Figure 4.9 depicts the instantaneous frequency along the microwave pulse for a glass slide of 0.96 mm thickness as 9.514 GHz. A linear trend representing direct proportionality between microwave signal frequency and glass plate thickness is observed.

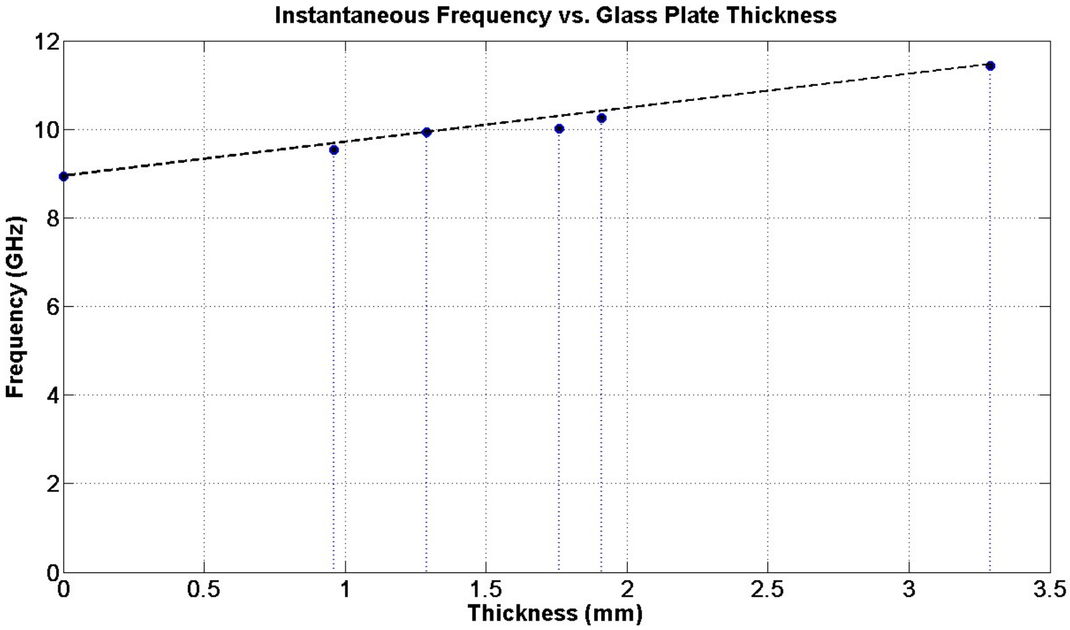

Figure 4.9 The Instantaneous frequency of microwave signal recorded as a function of BK-7 glass plate thickness.

Measurements were repeated for glass plate thickness of 1.76 mm, 1.91 mm and 3.29 mm and instantaneous frequency of 10.02 GHz, 10.25 GHz and 11.43 GHz were obtained respectively. Relating the immediate change in RF frequency to the instantaneous time delay between the pulses in the interferometer arms, an accurate measure of the sample depth can be obtained as outlined in the preceding section. A linear trend of 0.756 GHz/mm is observed for a material sample of refractive index 1.50 in the 1550 nm wavelength region. Based on the change in instantaneous frequency measured to the sample thickness relative to a calibration phase signal can allow the estimation of the optical path length, and thus the refractive index and or material thickness if one or the other is known. The MATLAB code in appendix A is used to perform the Short Time Fourier Transform analysis on the raw data obtained and the code in appendix B is used to calculate an ideal Gaussian envelope across the generated microwave signal and calculate the effective spectral width.

Table 4.1: Summarized measurement results for infrared transparent samples thickness estimation.

Sample	Frequency (GHz)	Mechanical Thickness (mm)	Calculated Thickness (mm)	%age Error
No Sample	8.943	0	-	
Mylar	9.008	0.050	0.0643	28.67 %
Glass slide	9.525	0.96	0.927	3.37 %
Glass slide	9.925	1.29	1.362	5.58 %
Glass slide	10.02	1.76	1.711	2.78 %
Glass slide	10.25	1.91	2.076	8.69 %
Glass slide	11.43	3.29	3.440	4.56 %
Glass partially covered with Mylar	For time period before mylar interface,10.02 GHz, for time period after mylar interface: 10.11 GHz	1.76 mm half and half 1.76 mm + 0.050 mm mylar sample	1.711 & 1.854	2.78 % & 5.10%
Single and Double Glass Layer partially covering each other	For time period covering single glass layer, 9.559 GHz, for time period covering double glass layer, 10.62 GHz	0.96 mm Half glass single layer and half double glass layer (0.96+1.29) mm	0.981 & 2.66	2.23% & 18.22%

Table 4.1 summarizes the experimental results obtained. A high percentage error is observed in the single and double glass layer partially covering each other. This is due to the added phase difference introduced due to an air wedge between the samples and in addition determining the exact refractive index for a multi-layered structure from which the thickness is estimated. Similarly, the refractive index of Mylar is assumed as 1.65 at 1550 nm, however a more precise measurement could improve the percentage error in the thickness measurement as frequency change determines optical path length difference. Microwave pulse generated when glass slide of thickness 0.96 mm is inserted in one of the interferometer arms is depicted in Figure 4.10.

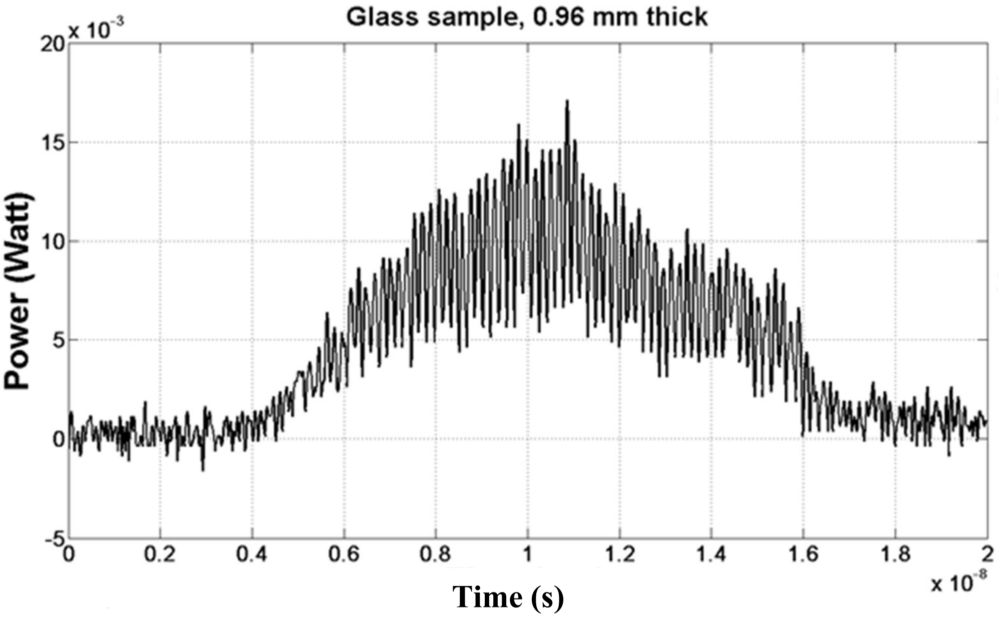

Figure 4.10 Microwave pulse generated when glass slide of thickness 0.96 mm is inserted in one of the interferometer arms.

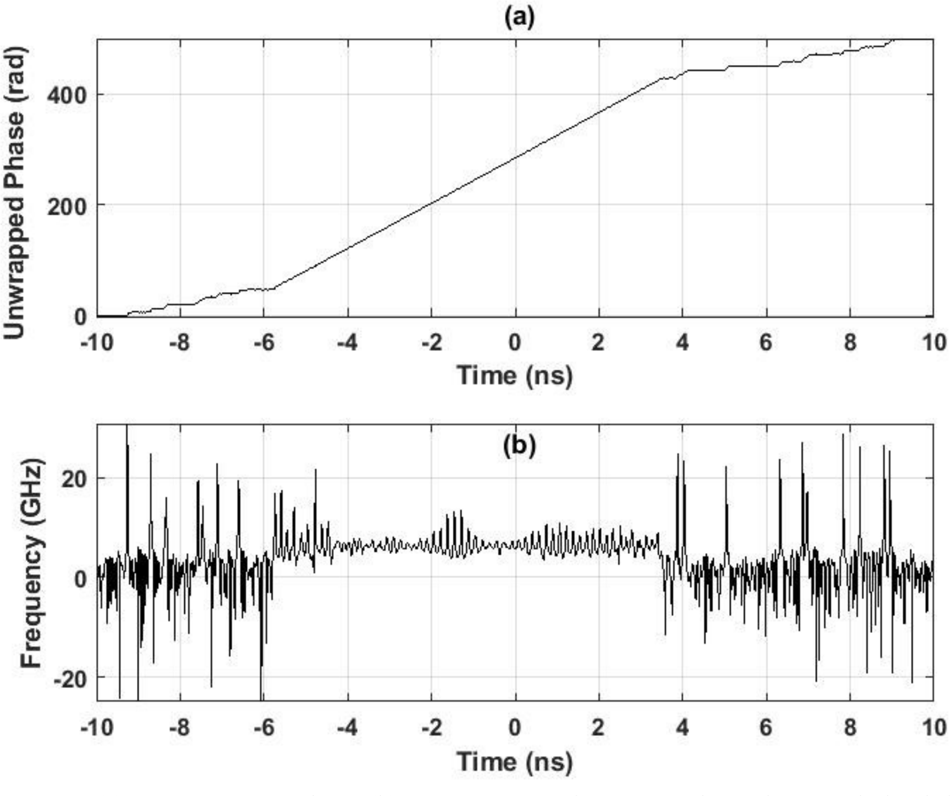

Figure 4.11 (a) Instantaneous Phase (b) Instantaneous frequency along time as derived from the Hilbert transform of the raw data.

The instantaneous phase and the derived instantaneous frequency versus time is depicted in Figure 4.11. Short time Fourier Transform of the signal reveals the instantaneous frequency fluctuation of the signal. The high sensitivity of frequency change to depth profile ratio also enables a measure of the surface form and therefore waviness. The spectrogram results are depicted in Figure 4.12 below:

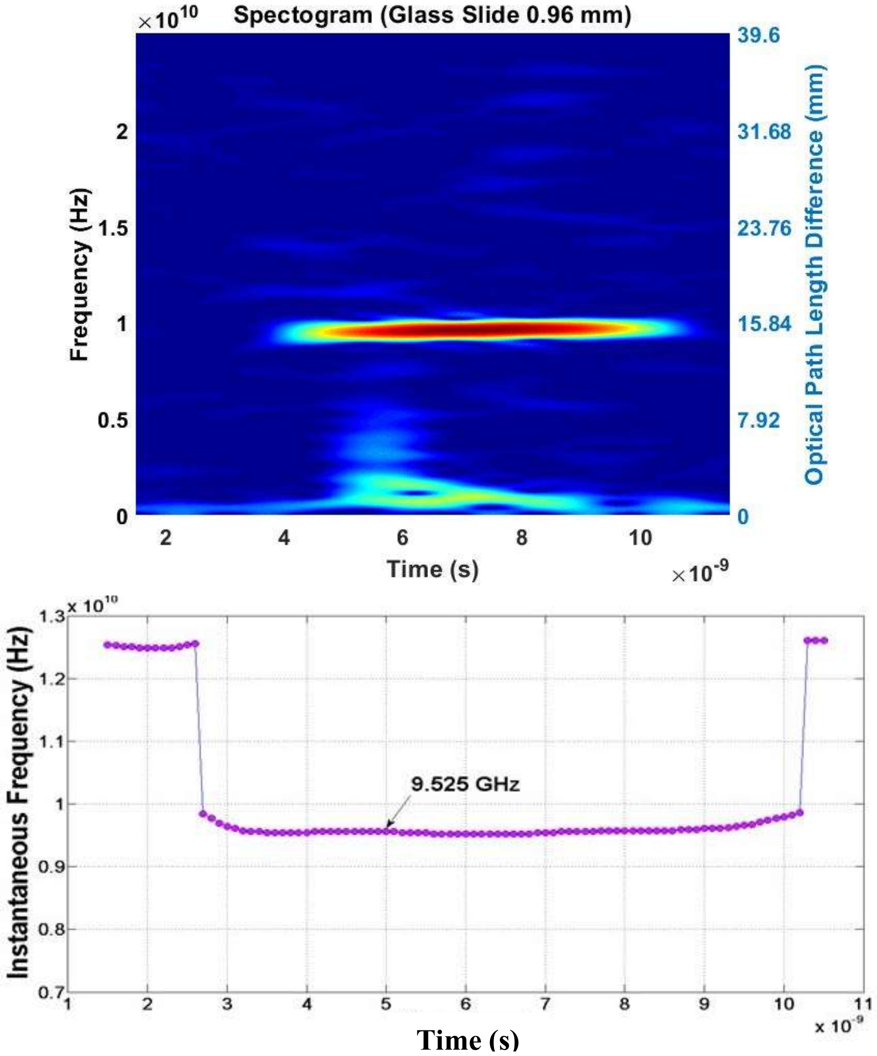

Figure 4.12 Corresponding spectrogram of microwave pulse generated when glass slide of thickness 0.96 mm is inserted in one of the interferometer arms.

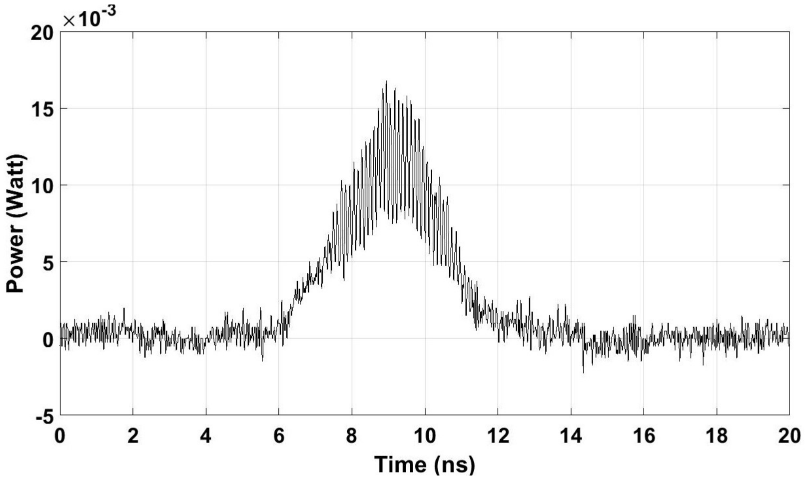

Figure 4.13 Generated microwave pulse generated when glass slide of thickness 1.29 mm is inserted in one of the interferometer arms.

Figures 4.13, 4.14 and 4.15 demonstrates the Short Time Fourier Transform analysis when 1.29 mm of BK-7 is placed in the sample arm.

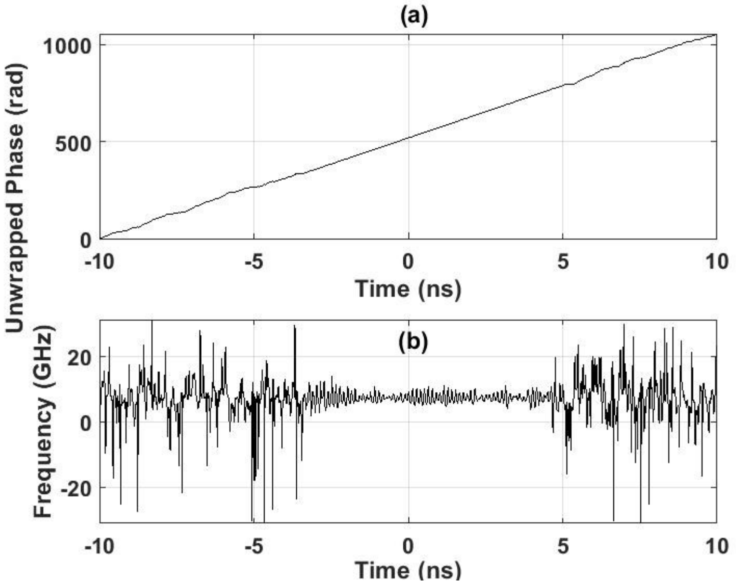

Figure 4.14 (a) Instantaneous phase (b) Instantaneous frequency of microwave pulse generated when glass slide of thickness 1.29 mm is inserted in one of the interferometer arms.

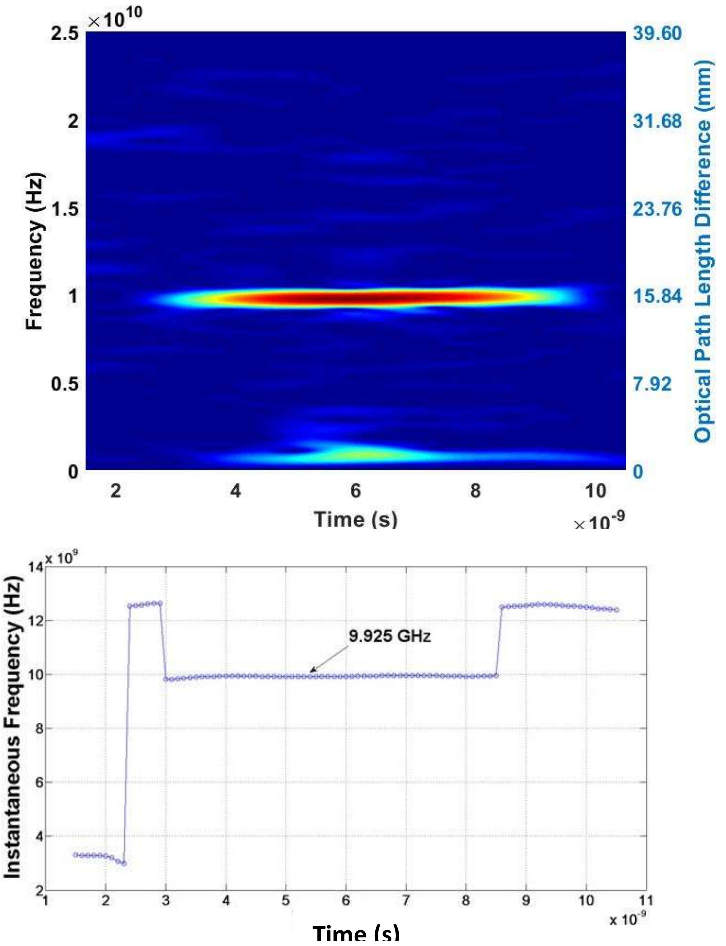

Figure 4.15 Corresponding spectrogram of microwave pulse generated when glass slide of thickness 1.29 mm is inserted in one of the interferometer arms.

B. Depth Difference Estimation

Experiments similar to those outlined in Section A were demonstrated for two glass slides placed on top of each other creating a slight air wedge between the two samples and measurement results obtained a corresponding uniform frequency deviation along time for the various slide combinations employed.

One of the innovative schemes planned constituted fixing a patch of Mylar sample on to the 0.96 mm thick glass slide to create a depth difference upon the incident IR spectrum. Figure 4.16 demonstrates the temporal waveform and the corresponding spectrogram. A phase jump is observed in the acquired temporal waveform which can be related to the point in space where the diffracted beam is incident upon the glass-Mylar interface.

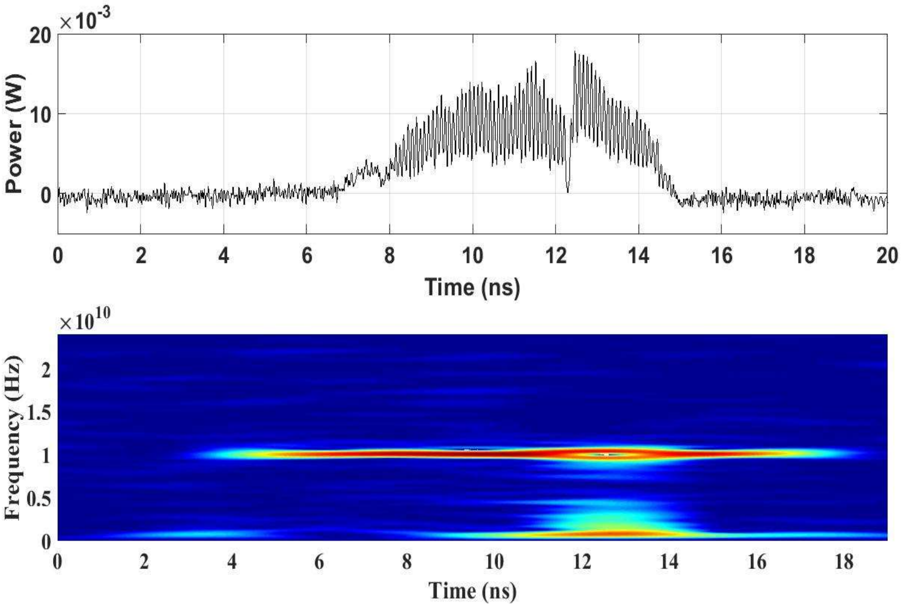

Figure 4.16 Demonstration of depth difference estimation when sample arm consists of a glass slide (0.96 mm) partially covered with Mylar to create depth difference. Incident beam is directed such that part of the spectrum is incident on the uniform thickness glass plate and part of the spectrum is incident on the glass Mylar interface.

Furthermore, to verify the utility of the experiment, an interface between 2 variable thickness and similar material, BK-7 glass plates were combined to create a depth difference upon the incident spectrum in the sample arm of the interferometer. An instantaneous jump along the frequency of the temporal pulse is observed. Spectrogram and instantaneous frequency results for glass slide combinations of 1.29 mm and 0.96 mm are depicted in Figure 4.17.

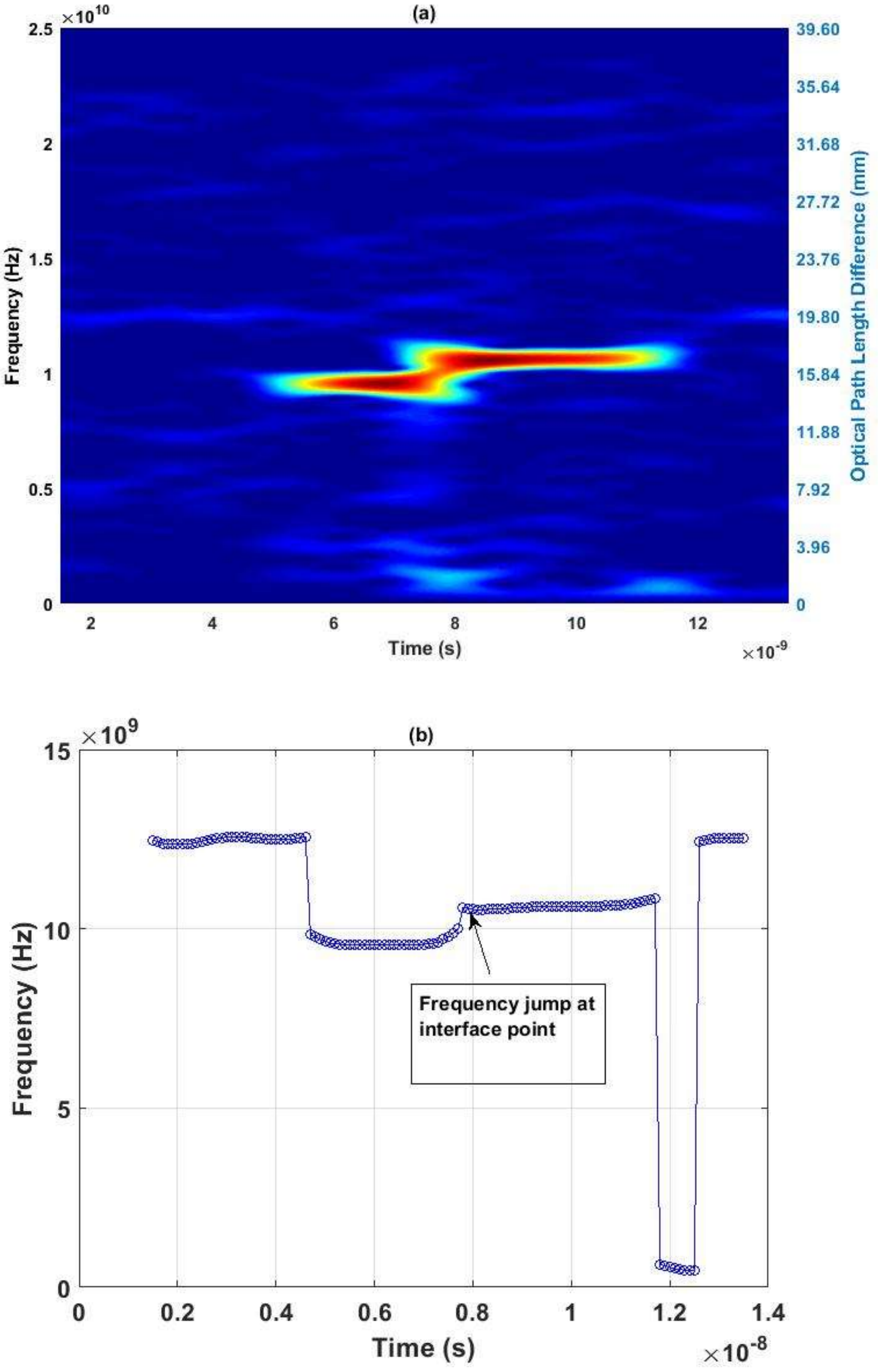

Figure 4.17 Glass slides 0.96 mm and 1.29 mm aligned to create a depth difference. (a) Spectogram, visual representation of spectrum of frequencies of the signal as it varies with time. The amplitude of a particular frequency at a particular time is represented by the color, with dark blues corresponding to low amplitudes and brighter colors up through red corresponding to progressively stronger amplitudes. (b) Instantaneous frequency along time as derived from spectrogram plot for generated microwave pulse depicts a local jump in instantaneous frequency at the break point between the two samples.

A frequency of 9.514 GHz is observed for the temporal signal to the left-hand side representing the incident spectrum upon the 0.96 mm glass slide, and a frequency of 10.59 GHz is observed at the right end of the microwave pulse representing spectral incidence at the 0.96 mm and 1.29 mm glass slide combination. Similar results were established for other glass combinations as well such as 1.29 mm and 1.76 mm; 3.29 mm and 0.96 mm., and the instantaneous change in frequency recorded was always proportional to the depth difference created. An estimate of the surface waviness or rather variation in depth across spectrum incident on sample can also be carried out by comparing the instantaneous frequency fluctuation over time. A frequency difference between sample spectrogram and calibration spectrogram is calculated. A measure of the surface flatness is established from the uniformity of frequency difference over time. Figure 4.18 demonstrates the frequency difference for 1.29 mm glass slide and reference signal.

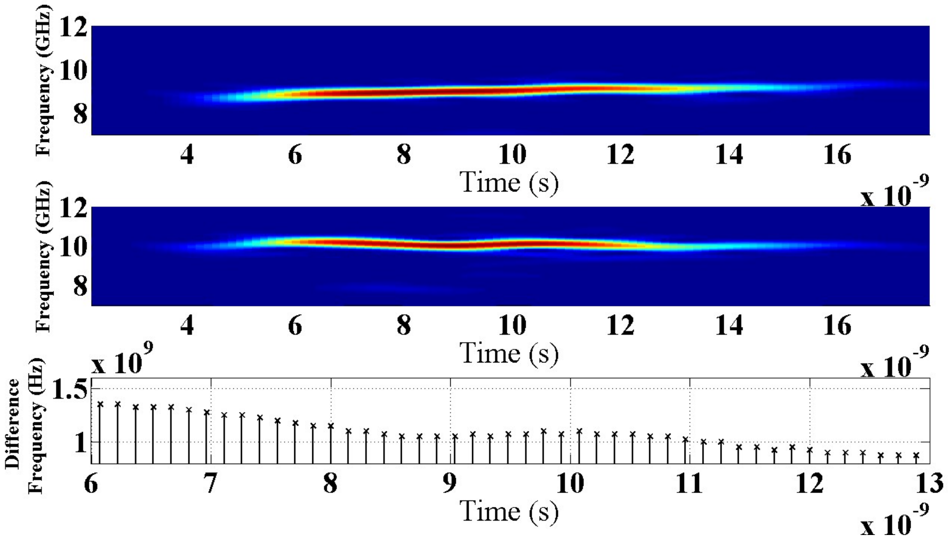

Figure 4.18 Frequency difference between reference signal and BK-7 sample with uneven surface profile.

4.5 Critical Discussion

In our proposed measurement system, the local depth profile along the diffracted spectrum can be mapped to its temporal analogue. Measuring the instantaneous frequency along time for the generated microwave pulse reveals information regarding the optical path length difference along one of the interferometer arms. The interference spectrum FSR is determined by the thickness and refractive index of the sample introduced in one of the interferometer arms. A dispersion compensating fibre maps the spectral interference pattern to a microwave frequency in the temporal profile. The optical path length difference information due to an IR transparent material sample can be used to calculate the depth of the sample under test when refractive index is known and at a scan rate of 50 MHz. However, the technique is limited in providing multi-layer material characterization. Repeatability and accuracy of the measured thickness are fairly consistent. A large percentage error in thickness measurement is observed for double glass layer combination. In addition, frequency dependent materials with complex spectral properties would be unsuitable for dimensional metrology application based on the underlying methodology as the optical Free Spectral Range (FSR) mapped to generated microwave frequency would be dependent on material absorption and scattering properties rather than depth estimation. Another limitation of the signal processing employed is also the inability to calculate permittivity and permeability of material under test. Non-contact sensing schemes rely on obtaining both geometrical and electromagnetic properties of sample under test.

Continuous measurement of surface displacement at high throughput over time can also be used for velocity and vibration measurement, as time derivative of distance or displacement. High spatial resolution of the proposed interrogation method is assured due to the fact that the temporal interference waveform can be captured using a high-speed PD and a fast analogue-to-digital converter. Therefore, the instantaneous RF frequency can be determined with very high temporal resolution. In this work, an equivalent temporal sampling rate of 100 GS/s was used to detect the interference waveforms, leading to a maximum temporal resolution of 10 ps in theory. Linear time-wavelength-space mapping of generated microwave pulse can be used to recover precisely depth difference point with high-resolution. Similarly, the spatial resolution, δ*z* is determined by the spectral resolution of measurement system (0.02 nm). The spectral resolution is determined as [3, 23]:

$$\partial\lambda_{res} = \left(fDz\right)^{-1}$$

where f is sampling frequency and Dz is the dispersion enabling DFT in (ps/nm). Since the diffracted beam of FWHM (6.1 nm) is mapped to a beam profile of 3.83 mm. The corresponding lateral resolution from the wavelength-time-space relation is thus estimated as 12.5 μm. Similarly, depth resolution is limited by sampling rate of electronic digitizer. Frequency change to depth ratio for glass of refractive index 1.50 is estimated at 746 MHz/mm; since the minimum frequency resolution which is the ratio of sampling frequency (100 GS/s) and number of data points (2000) results in a frequency of 50 MHz. The linear wavelength-time-space mapping corresponds to a spatial resolution of 42.5 μm. A minute change in thickness corresponds to a frequency change in the MHz range denoting high sensitivity. However, as STFT analysis is used to estimate the instantaneous RF frequency over time, the maximum temporal resolution (and hence the spatial resolution) is achieved with a sacrificed frequency resolution, which in turn leads to poor accuracy in ultra-thin depth measurement. A fundamental trade-off between frequency and temporal resolution in STFT analysis always exists.

4.6 Summary

We have proposed and experimentally demonstrated a novel measurement scheme for IR transparent samples utilising microwave photonic detection technique. Ultrafast real-time measurements are performed by scanning the IR spectrum of a mode-locked laser along a sample under test in a Michelson interferometer structure. The proposed method is verified by proof-of-concept experiments, in which measurements of uniform thickness and distributed thickness have been demonstrated. Thanks to its simultaneous ultrafast speed, high spatial resolution, and sensitive frequency to depth response, we believe the proposed technique is a promising measurement solution for accurate depth profile, optical path length and material or multi-layered material composition determination where ultrafast and ultrahigh spatial resolution measurement is required. In its present state, the components used for making up the system such as lens system, a beam splitter, laser, a photodetector and mechanical stage are bulky and costly. Microfabrication technology integrating all these components onto a Silicon and or Indium Phosphide platform could reduce the associated cost and make the system more practical for use in industrial applications.

REFERENCES

[1] T. J Quinn, "Practical realization of the definition of the metre, including recommended radiations of other optical frequency standards," *Metrologia*, vol. 40, pp. 103-133.

[2] S. Svanberg, "Laser remote sensing - From environmental to medical applications," in *2012 Asia Communications and Photonics Conference (ACP)*, Guangzhou, 2012.

[3] H. Chen, K. Goda, C. Wang and B. Jalali, "Ultrafast surface inspection using hybrid dispersion laser scanner," in *CLEO*, San Jose, CA, , 2013.

[4] A Pique, R.C.Y. Auyeung, R.C.Y, J. L. Stepnowski, D. W. Weir, C. B. Arnold, R. A. Mcgill, D. Chrise, "Laser processing of polymer thin for chemical sensor applications. Surface and Coatings Technology," vol. 163, pp. 293-299.

[5] C. Wang, "Dispersive Fourier transformation for versatile microwave photonics applications," *Photonics,* vol. 1, no. 4, pp. 586-612, 2014.

[6] C. Wang and J. Yao, "Photonic generation of chirped millimeter-wave pulses based on nonlinear frequency-to-time mapping in a nonlinearly chirped fibre bragg grating," *IEEE Transactions on Microwave Theory and Techniques,* vol. 56, no. 2, p. 542–553, 2008.

[7] C. J. Weng, B. R. Lu, P. Y. Cheng, C. H. Hwang and C. Y. Chen, "Measuring the thickness of transparent objects using a confocal displacement sensor," *2017 IEEE International Instrumentation and Measurement Technology Conference (I2MTC)*, pp. 1-5, Turin, 2017.

[8] P. V. Kelkar, F. Coppinger, A. S. Bhushan and B. Jalali, "Time-domain optical sensing," *Electron Letters,* vol. 35, no. 19, pp. 1661-1662, 1999.

[9] P. Lutzmann, B. Göhler, C. A. Hill and F. D. M. v. Putten, "Laser vibration sensing at Fraunhofer IOSB: review and applications," *Optical Engineering,* vol. 56, no. 3, 031215 (2016).

[10] J. M. Kilpatrick and V. Markov, "Matrix laser vibrometer for transient model imaging and rapid nondestructive testing," in *Eighth International Conference on Vibration Measurements by Laser Techniques: Advances and Applications,* 2008.

[11] B. Schwartz, "Mapping the world in 3D," *Nature Photonics,* vol. 4, p. 429–430, July 2010.

[12] B. Dai et al., "Ultrafast Three-Dimensional Imaging System Based on Phase-Shifting Method and Hybrid Dispersion Laser Scanning," *IEEE Photonics Journal,* vol. 7, no. 3, pp. 1-9, June 2015.

[13] S. Zhang, D. V. D. Weide and J. Oliver, "Superfast phase-shifting method for 3-D shape measurement," *Optics Express,* vol. 18, no. 9, pp. 9684-9689, 2010.

[14] W. J. Walecki, F. Szondy and et al., "Fast in-line surface topography metrology enabling stress calculation for solar cell manufacturing for throughput in excess of 2000 wafers per hour," *Measurement Science and Technology,* vol. 19, no. 2, 2008.

[15] K. Goda, A. Motafakker-Fard, K. K. Tsia and B. Jalali, "Serial Time Encoded Amplified Microscopy (STEAM) for high-throughput detection of rare cells," in *2010 IEEE Photonics Society Winter Topicals Meeting Series (WTM)*, Majorca, 2010.

[16] C. K. Mididoddi, F. Bai, G. Wang, J. Liu, S. Gibson and C. Wang, "High Throughput Photonic Time-Stretch Optical Coherence Tomography with Data Compression," *IEEE Photonics Journal,* vol. 9, no. 4, pp. 1-15, 2017.

[17] J. Chou, Y. Han and B. Jalali, "Time-wavelength spectroscopy for chemical sensing," *IEEE Photon Technologies Letters,* vol. 16, no. 4, pp. 1140-1142, 2004.

[18] Y. Wang, F. Xie, S. Ma, L. Dong, "Review of surface profile measurement techniques based on optical interferometry," *Optics and Lasers in Engineering*, Volume 93, pp. 164 – 170, 2017.

[19] F. Gao, H. Muhamedsalih and X. Jiang, "Surface and thickness measurement of a transparent film using wavelength scanning interferometry, " *Optics Express*, vol. 20, no. 19, 2012.

[20] F. Blais, "A review of 20 years of range sensor development," *Journal of Electronic Imaging*, vol. 13, pp. 231 – 240, 2004

[21] K. Harding, "Latest optical methods for industrial dimensional metrology," *Proceedings of SPIE 6000*, pp. 1-14, 2005

[22] D. R. Solli, J. Chou, and B. Jalali, “Amplified wavelength-time transformation for real-time spectroscopy,” *Nature Photon*ics, vol. 2, no. 1, pp. 48–51, 2008.

[23] K. Goda and B. Jalali, "Dispersive Fourier transformation for fast continuous single-shot measurements," *Nature Photonics,* vol. 7, no. 2, pp. 02-112, 2013.

[24] V. Srivatsan, R. Katz, D. Dutta, "Fixtureless sensor standoff control for high-precision dimensional inspection of free-form parts, " Journal of Manufacturing Science & Engineering, vol. 129, pp. 172 – 179, 2007

[25] S. Son, H. Park, K. Lee, "Automated laser scanning system for reverse engineering and inspection," *International Journal of Machine Tools Manufacturing,* vol. 42, pp. 889 – 897, 2007.

[26] P. Hlubina, D. Ciprian, R. Clebus, J. Luňáček, M. Lesnak, "White-light spectral interferometric technique used to measure thickness of thin films," *Proceedings of SPIE - The International Society for Optical Engineering,* 2007

[27] J. Capmany and D. Novak, "Microwave photonics combines 2 worlds," *Nature Photonics,* vol. 1, no. 6, p. 319–330, 2007.

[28] H. Chi and J. Yao, "All-fibre chirped microwave pulses generation based on spectral shaping and wavelength-to-time conversion," *IEEE Transactions on Microwave Theory and Techniques,* vol. 55, no. 9, p. 1958–1963, 2007.

[29] J. Chou, Y. Han, B. Jalali and S. Member, "Adaptive RF-Photonic Arbitrary Waveform Generator," *IEEE Photonics Technology Letters,* vol. 15, no. 4, p. 581–583, 2003.

[30] M. H. Asghari, Y. Park and J. Azana, "Complex-field measurement of ultrafast dynamic optical waveforms based on real-time spectral interferometry," *Optics Express,* vol. 18, pp. 16526–16538, 2010.

[31] M. Li and J. Yao, " Photonic generation of continuously tunable chirped microwave waveforms based on a temporal interferometer incorporating an optically pumped linearly chirped fibre Bragg grating," *IEEE Transactions on Microwave Theory and Techniques,* vol. 59, no. 12 part 2, pp. 3531-3537, 2011.

[32] M. A. Muriel, J. Azana and A. Carballar, "Real-time Fourier transformer based on fibre gratings," *Optics letters,* vol. 24, no. 1, pp. 1-3, 1999.

CHAPTER 5

CHIRPED PHOTONIC MICROWAVE AND MM-WAVE GENERATION APPLIED TO MM-WAVE COHERENCE TOMOGRAPHY

5.1 Introduction

The previous two chapters focussed on photonic microwave detection for obtaining spectrally encoded information in the temporal domain. The photonically generated microwave signals were demodulated to attain characteristic properties specific to strain applied upon chirped fibre Bragg gratings and surface metrology of IR transparent samples. In this chapter, photonic techniques realising the generation of high-speed frequency swept MM-Wave pulses is utilised as a potential source for high throughput frequency swept MM-Wave coherence tomography.

5.2 Problem Statement

The concept of photonic microwave and MM-Wave generation provides sufficient motivation to utilise the photonic generation of MM-Wave signals for free space applications. Since the photonics-based concept is capable of generating large bandwidth, short temporal duration and high chirp rate MM-Wave pulses at an ultrafast rate (~ 50 MHz), real time dynamic short range (few mm to 50 m) and long range (~ 300m to km) sensing can be explored. Technology focussed towards autonomous or driver-less vehicles rely on non-contact sensing for both short range and long-range distance scanning. An autonomous vehicle must be able to monitor other vehicles in its vicinity, maintain safe distance, similarly ability to identify terrain and self-navigate alien landscape in space exploration vehicles makes the concept of a high throughput millimetre wave source extremely useful.

The main focus of this chapter is the analysis of various possible implementations of the photonic techniques for chirped high frequency microwave and MM-Wave pulses. The implementation of a Photonics-Based swept source MM-Wave coherence tomography system is proposed. Pure MM-Wave non-contact sensing, as proof-of-concept is demonstrated. A comparison is made between the measured performance of the experimental results, and conventional RADAR, Time-of-Flight (TOF) concepts.

5.3 Swept Source Photonic MM-Wave Generation Schemes

The first sub-section begins with an outline of balanced and unbalanced Temporal Pulse Shaping (TPS) for generation of MM-Wave pulses. Firstly, the novelty I introduced by improving upon existing techniques to generate frequency up-converted chirped MM-Wave pulses with an enhanced Time-Bandwidth product and the associated limitations that led to the adaptation of differential dispersion based MM-Wave signal generation scheme for applied MM-Wave coherence tomography is demonstrated. Secondly, the differential dispersion based chirped MM-Wave pulse generation technique adopted and the results obtained are outlined. Simulations and experimental demonstration of chirped MM-Wave pulses verifies the utility of the proposed approach in acting as a potential source for MM-Wave coherence tomography.

5.3.1. Microwave Frequency Up-Conversion

Frequency up-conversion is the term used to identify the technique of frequency multiplication of a low frequency RF/microwave signal to a high frequency microwave and MM-Wave signal. In an optical frequency up-conversion scheme, low frequency signal is modulated onto an optical carrier, manipulating sideband and optical carrier strength of modulated signal by phase control in a complex Mach Zehnder Modulator (MZM) architecture. The optical signal is ultimately converted to a frequency up-converted microwave waveform at the photodetector. An MZM is an optical modulator used to modulate the amplitude of an optical input signal [1]. We utilise MZM as external modulators. MZMs rely on the Pockel's effect, by which an induced voltage across a crystal linearly changes the refractive index [2]. MZMs can reach extinction ratios exceeding 20 dB, and feature lower insertion loss than EAMs [3]. The extinction ratio is the difference between the fully off- and the fully on-state of the modulator or the ratio of the peak transmission power to the minimum transmission power. In general, as compared to direct modulation, external modulation offers better linearity, higher modulation frequencies (typically <20 GHz but 100 GHz has been demonstrated), higher output power, narrow spectral linewidth, and lower noise. These advantages mainly arise because the modulator and laser can be optimised separately: the laser for high power and low noise and the modulator for high-speed and efficiency [4 – 6]. We demonstrate a novel approach to generating microwave and MM-Wave pulses inspired from the concept of microwave frequency up-conversion. Dual Parallel-MZM are relatively expensive and the frequency up-conversion property of MZM's in cascade is utilised to generate chirped MM-Wave signals. In addition, all previous frequency swept up-conversion schemes demonstrate modulation upon a CW carrier leading to CW MM-Wave generation. Simulations in VPI demonstrate a cascaded MZM setup with ultra-short laser pulses to generate ultra-fast chirped MM-Wave pulses with an enhanced Time-Bandwidth product (TBWP).

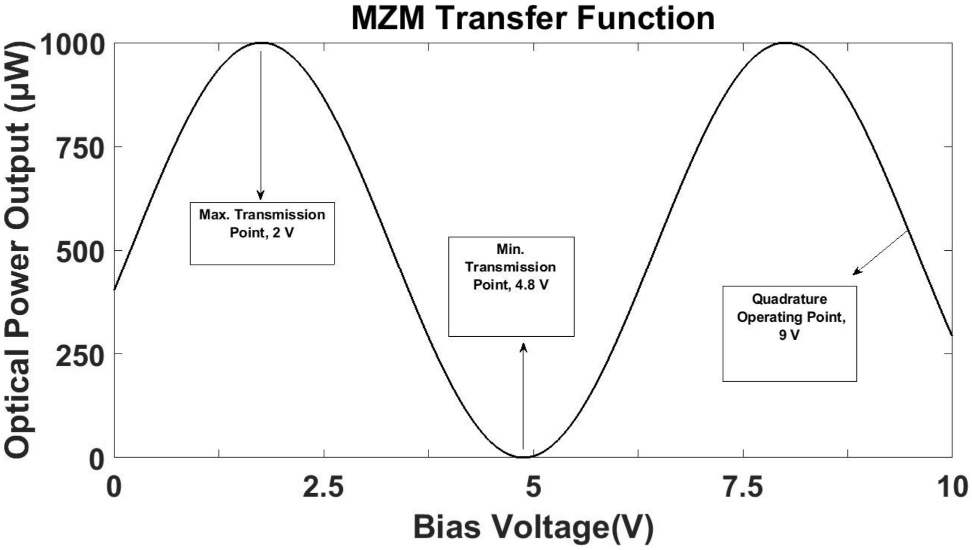

Figure 5.1 Experimental Bias characteristic of MZM. The optical power of output signal versus applied DC bias voltage at MZM was recorded at discrete voltage levels. A sine interpolation used to characterise the transfer function, and the ideal characteristics used to model MZM characteristics employed for simulations in VPI.

Figure 5.1 demonstrates the bias characteristics of a typical MZM; the change in output optical power with applied DC voltage is depicted. Figure 5.2 depicts an MZM with phase modulation in one arm controlled by the applied bias voltage.

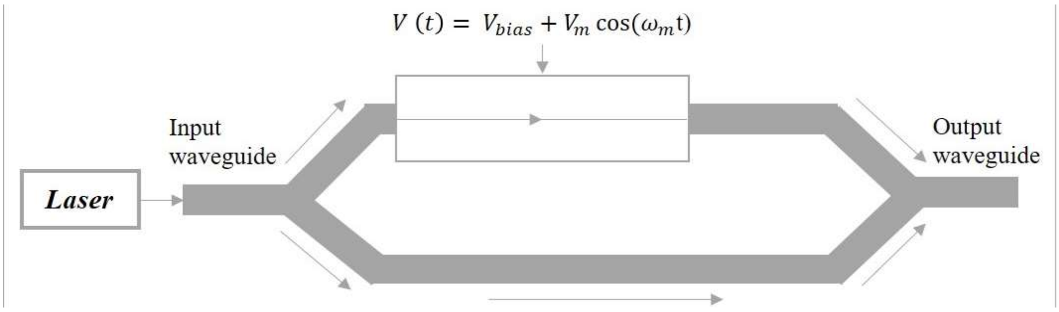

Figure 5.2 MZM architecture. Phase difference between both arms is introduced by an applied voltage *V(t)*.

An input optical pulse is divided between the two arms of the MZM. One of the MZM arms is driven by a modulating RF/microwave electrical signal. The electrical signal induces phase modulation in that arm of the MZM. The divided optical signal, phase modulated in one arm combine to form an intensity modulated output. Choosing the bias voltage, V_{bias}, and amplitude of microwave drive signal, V_m determines the operating point of MZM. The effect on a propagating optical signal is thus a voltage-dependent phase shift. An MZM employs one or two such phase shifters, configured in a Mach-Zehnder interferometer. The interference of the phase modulated signals at the output of the MZM results in an amplitude modulated signal. Using two phase shifters, driven with opposite phases, improves the efficiency of the modulation.

Mathematically, the electrical field at the output of an MZM [8 - 10] can be expressed as:

$$E_{out}(t) = E_o \cos\left[\frac{\phi[V(t)]}{2}\right].\cos(\omega_c t) \tag{5.1}$$

Where E_o and ω_c determine the amplitude and frequency of the input optical carrier. *V(t)* is the RF/microwave electrical driving signal and $\phi[V(t)]$ is the corresponding phase difference induced by the electrical drive signal, *V(t)*.

$$V(t) = V_{bias} + V_m \cos(\omega_m t) \tag{5.2}$$

where V_{bias} is the dc bias voltage, V_m and ω_m are the amplitude and angular frequency of the electrical drive signal. Optical carrier phase difference between the two interferometer arms induced by *V(t)* is expressed as:

$$\phi[V(t)] = \pi\left[\frac{V_{bias}}{V_{\pi}} + \frac{V_m}{V_{\pi}}.\cos(\omega_c t)\right] \qquad (5.3)$$

Inserting eq. 5.3 into eq. 5.1 yields the mathematical relationship shown in eq. 5.4, expressing the output field after an optical carrier passes through an MZM driven by an electrical sinusoidal electrical voltage, *V(t):*

$$\begin{aligned} E_{out}(t) = {} & E_o cos\left(\frac{\phi}{2}\right) J_o(\beta)\, cos(\omega_c t) + \; E_o cos(\phi/2) \\ & \times \left\{ \sum_{n=1}^{\infty} J_{2n}(\beta) [cos(\omega_c t - 2n\omega_m t + n\pi) + cos(\omega_c t + 2n\omega_m t - n\pi)] \right\} \\ & - \; Eosin(\phi/2) \\ & \times \left\{ \sum_{n=1}^{\infty} J_{2n-1}(\beta) \left[sin\left(\omega_c t - (2n-1)\omega_m t + n\pi - \frac{\pi}{2}\right) - sin\left(\omega_c t + (2n-1)\omega_m t \right.\right.\right. \\ & \left.\left.\left. - \, n\pi + \frac{\pi}{2}\right)\right]\right\} \qquad (5.4) \end{aligned}$$

Based on the above equation, selecting the maximum transmission point would require choosing ϕ as an even multiple of π (0,2π,4π…) resulting in the Bessel function solutions associated with cosine term only. This would result in suppression of all odd order sidebands. Similarly, choosing ϕ as an odd multiple of π (π,3π,5π…) would lead to biasing the MZM at the minimum transmission point resulting in the Bessel function solutions associated with sine term only. This would result in suppression of all even order sidebands along with the optical carrier [14, 15]. The quadrature point is the middle of the linear region where there exists maximum linearity as depicted in Figure 5.1. An MZM biased at the quadrature point would yield all sidebands along with carrier at the output. MZM is usually quadrature biased as it adds no even order distortion to the RF signal modulated onto the optical carrier.

When $\phi = \pi$, the signal at the output of an MZM can be expressed as follows:

$$E_{01}(t) = E_o J_1(\beta_1)\, sin((\omega_c - \omega_m)\, t - \theta_1) + \; E_o J_1(\beta_1)\, sin((\omega_c + \omega_m)\, t + \theta_1) \qquad (5.5)$$

Wherein θ_1 is the initial phase of the microwave electrical drive signal. After passing through a second MZM cascaded in series to the first, resulting E-field can be expressed as [16]:

$$\begin{aligned} &\mathrm{E_{02}(t)} \\ &= \mathrm{E_o J_1(\beta_1)} J_1(\beta_2) \times \{cos((\omega_\mathrm{c} - 2\omega_\mathrm{m})\,\mathrm{t} - \theta_1 - \theta_2) + \cos(\omega_c t - \theta_1 + \theta_2) \\ &+ \cos(\omega_\mathrm{c}\mathrm{t} + \theta_1 - \theta_2) + \mathrm{E_o J_1(\beta_1)}\, cos((\omega_\mathrm{c} + 2\omega_\mathrm{m})\,\mathrm{t} + \theta_1 \\ &+ \theta_2)\} \end{aligned} \tag{5.6}$$

If the phase condition $2\theta_1 - 2\theta_2 = (2k + 1)\pi$ is satisfied, equation 5.6 can be further simplified as:

$$\mathrm{E_{02}(t)} = \mathrm{E_o J_1(\beta_1)} J_1(\beta_2) \times \{cos((\omega_\mathrm{c} - 2\omega_\mathrm{m})\,\mathrm{t} - \theta_1 - \theta_2) + \mathrm{E_o J_1(\beta_1)}\, cos((\omega_\mathrm{c} + 2\omega_\mathrm{m})\,\mathrm{t} + \theta_1 + \theta_2)\} \tag{5.7}$$

As can be seen from Equation 5.7, the output optical signal at the second modulator, the phase condition suppresses the optical carrier and two sidebands obtained are twice the initial microwave frequency apart from the suppressed optical carrier. Beating the two optical sidebands would lead to the generation of a frequency quadrupled waveform [17].

Similar techniques utilising the phase correlation between spectral lines induced by an MZM leading to only selective side-bands with considerable strength can lead to the required frequency multiplied output waveform. One of the first demonstrations was proposed in [18] wherein the MZM is biased at the minimum transmission point (MITP) to suppress all even order harmonics leading to the first order sidebands having considerable strength and thus generating an output waveform that has twice the frequency of the driving RF signal. After that, an extension of the proposed solution has led to the generation of frequency quadrupled, frequency sextupled and even twelve-tupled waveforms [16 – 18] by using a combination of MITP and MATP architectures and in most cases using a filter or an optical interleaver to suppress the carrier. Though, capable of achieving frequency up-conversion, a limitation of conventional techniques lies in use of filtering to attain the desired frequency leading to some insertion loss and thus a lower Signal to Noise Ratio. A filter-less solution has been proposed by the use of a Dual Parallel MZM (DP-MZM) [19] wherein RF drive level is adjusted to suppress the carrier and yield required side-bands with considerable strength, leading to the generation of the required MM-Wave frequency.

Figure 5.3 (a) depicts a typical balanced temporal pulse shaping system inclusive of a pulsed laser source, an MZM and conjugate dispersive elements at input and output port of MZM respectively. The output from a balanced TPS can be recognised as the convolution of the input pulse with the modulating signal spectrum multiplied by a quadratic phase term.

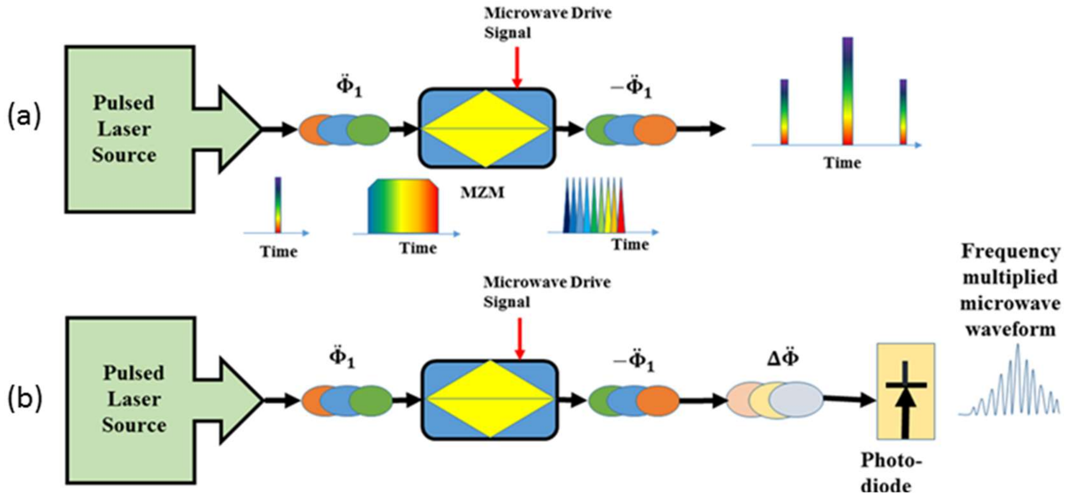

Figure 5.3 Setup utilised to explain the concept of (a) Balanced and (b) Unbalanced Temporal Pulse Shaping System. Simulations are performed in VPI to verify the proposed approach.

An optical pulse is first temporally stretched and spectrally dispersed after passing through the first dispersive element. The stretched pulse is modulated by a microwave signal driving the MZM biased at the minimum transmission point. After passing through the conjugate dispersive component, the stretched modulated pulse is compressed, and two scaled replicas of the Gaussian input pulse are obtained. The output is Fourier transform of microwave drive signal [20]. The two replicas are separated by a time separation, *T*, from the optical carrier which is directly proportional to the modulating frequency ω_m and dispersion of fibre $\ddot{\Phi}_1$ such that $T=\omega_m\ddot{\Phi}_1$.

In a UB-TPS framework, as depicted in Figure 5.3 (b), the two dispersive components at either end of the MZM have dispersion values chosen such that they are not the absolute equivalent as in a balanced TPS framework. This can be demonstrated as a standard TPS framework in addition to an extra dispersive component. The dispersion mismatch, or the value of the extra dispersive element is chosen such that the offset dispersion added maps the spectrum at the output of a balanced TPS system to its temporal profile obtained at the photo-detector. This technique accomplishes continuously tunable microwave frequency up-conversion dictated by the dispersion imbalance.

5.3.2. Unbalanced Temporal Pulse Shaping in a Cascaded Modulation Scheme

High-frequency microwave and MM-Wave pulse generation have been demonstrated by utilising an unbalanced temporal pulse shaping (UB-TPS) architecture using cascaded Mach-Zehnder modulators both biased at the minimum transmission point to enhance the frequency multiplication factor of the output signal [21, 22]. A low-frequency microwave electrical source, 2 GHz is used to drive both modulators. The microwave modulation frequency is upconverted to the MM-Wave frequency contained within a Gaussian envelope. With a dispersion imbalance of four times and two cascaded MZM's biased at the minimum transmission point, the generated MM-Wave signal is 16 times (4 x 2 x 2) the original microwave driving frequency.

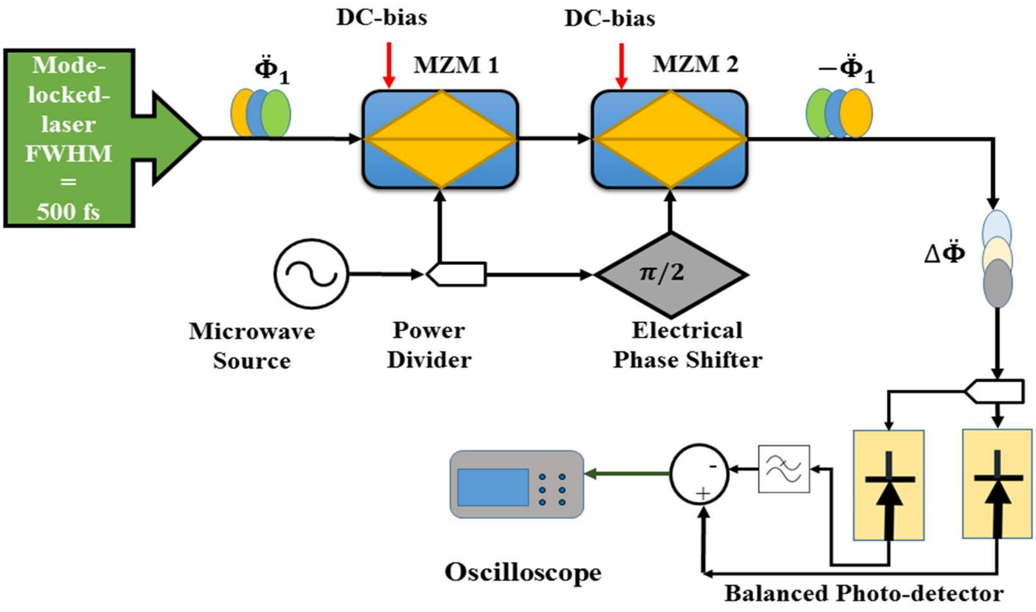

Figure 5.4 Unbalanced Temporal Pulse Shaping in a Cascaded Modulation Scheme. The proposed setup is implemented in VPI.

Utilising the frequency multiplication factor due to unbalanced dispersion in temporal pulse shaping systems and the frequency quadrupling effect achieved by cascading MZM's biased at minimum transmission, the generation of MM-Waves from microwave electrical signals is accomplished. The set up employed is depicted in Figure 5.4. Gaussian pulses of full-width half maximum, 500 fs, Bit-rate 50 MHz are generated by a mode-locked laser.

(a) Output at MZM 1

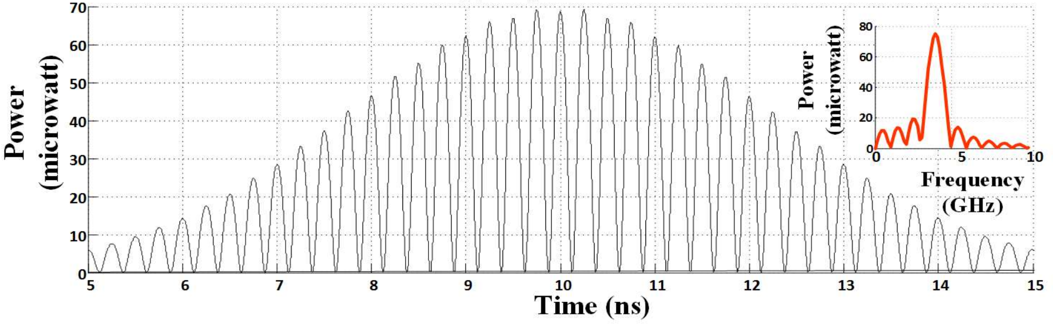

(b) Output at MZM 2

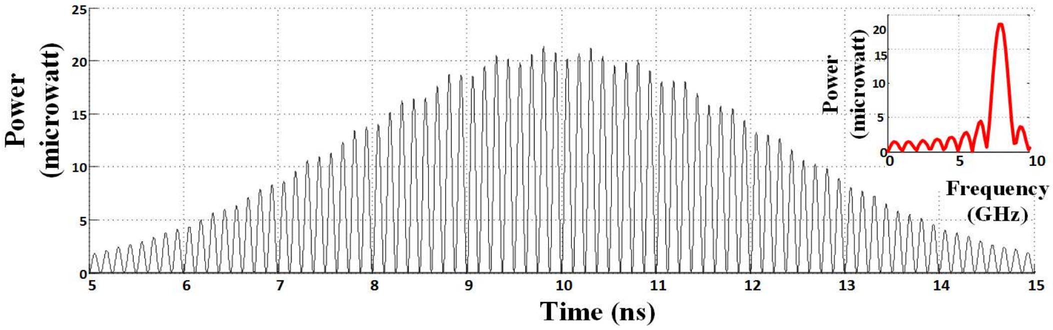

Figure 5.5 Simulation results for (a) Output at MZM 1 (b) Output at MZM 2.

The pulses pass through a dispersive element. The value of dispersion is chosen based on the Fraunhofer condition [23], enforcing wavelength to time mapping, 40 km of fibre in our demonstration.

The generated MM-Wave frequency contained within a Gaussian envelope can be expressed as:

$$\omega_{output} = \omega_m \cdot \left| 2 \times 2 \times \frac{\ddot{\Phi}}{\Delta \ddot{\Phi}} \right| \tag{5.8}$$

The dispersion imbalance ratio $\frac{\ddot{\Phi}}{\Delta\ddot{\Phi}}$ is 10 in the set up depicted in Figure 5.4. After passing through the final dispersive element, MM-Wave pulses contained within a

Gaussian envelope can be observed as shown in Figure 5.5. A zoomed-in view of the generated MM-Wave pulse is depicted as well. An MM-Wave pulse with a frequency of 80 GHz is obtained at the output as shown in Figure 5.6.

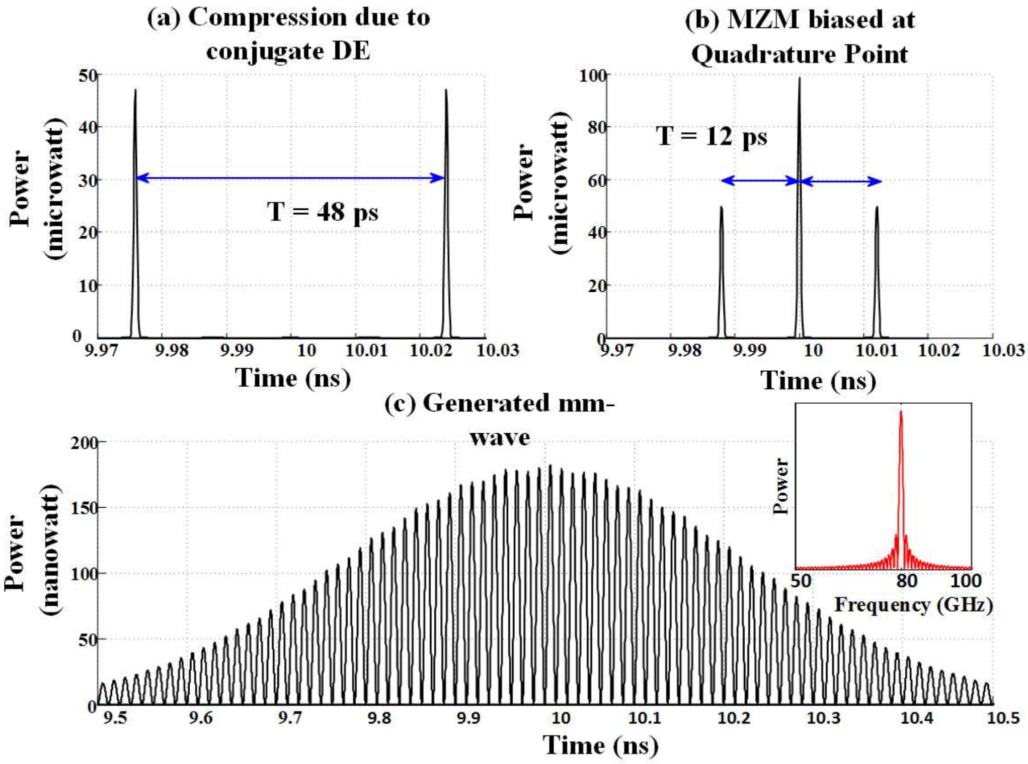
(a) Compression due to conjugate DE

(b) MZM biased at Quadrature Point

(c) Generated mm-wave

Figure 5.6 Simulation results for (a) Output at the balanced TPS system for MZM cascade biased at minimum transmission point (b) Output at the balanced TPS system for MZM biased at quadrature point (c) Generated MM-Wave pulse.

The frequency multiplication factor is observed to be 40, 2x due to the first MZM, and 2x due to the second MZM and 10x due to the dispersion imbalance.

The generation of MM-Wave pulses by employing a microwave electrical source to drive two cascaded MZM's in an unbalanced temporal pulse shaping set up is achieved. In order to enhance the frequency multiplication factor the MZM's are biased at the minimum transmission point. The effective frequency up-conversion from microwave to MM-Wave frequency is four times the dispersion imbalance. An improvisation upon the existing technology is demonstrated by generating frequency swept MM-Wave pulses as outlined in the following section.

5.3.3. Chirped Microwave Pulse Generation Based on Unbalanced Temporal Pulse Shaping (UB-TPS)

The proposed broadband frequency-swept MM-Wave source is based on direct frequency up-conversion of a low-frequency chirped microwave source using cascaded UB-TPS system, as shown in Figure 5.4. The approach is verified by numerical simulations performed using commercial software (VPItransmissionMaker) assuming main experimental system parameters as in [22]. A mode-locked laser generates ultrashort optical pulses with Gaussian shape and full-width half maximum (FWHM) pulse width of 500 fs. The optical pulses are pre-stretched by the first DE with dispersion value of 20 km long fibre. The stretched pulse serves as the optical carrier and is modulated by the microwave drive signal at two cascaded MZMs that are both biased at Minimum Transmission (MITP).

Here a positively chirped microwave signal drives both modulators. The instantaneous microwave frequency sweeps from 1 to 2.5 GHz in a span of 12 ns. To fulfil the phase matching condition in cascaded modulation, a broadband frequency-independent 90-degree microwave phase shifter is inserted between the two MZMs. The aim is to utilise the frequency up-conversion due to unbalanced dispersion in a TPS system and translating the chirp in the driving microwave frequency to the photonically generated MM-Wave pulse.

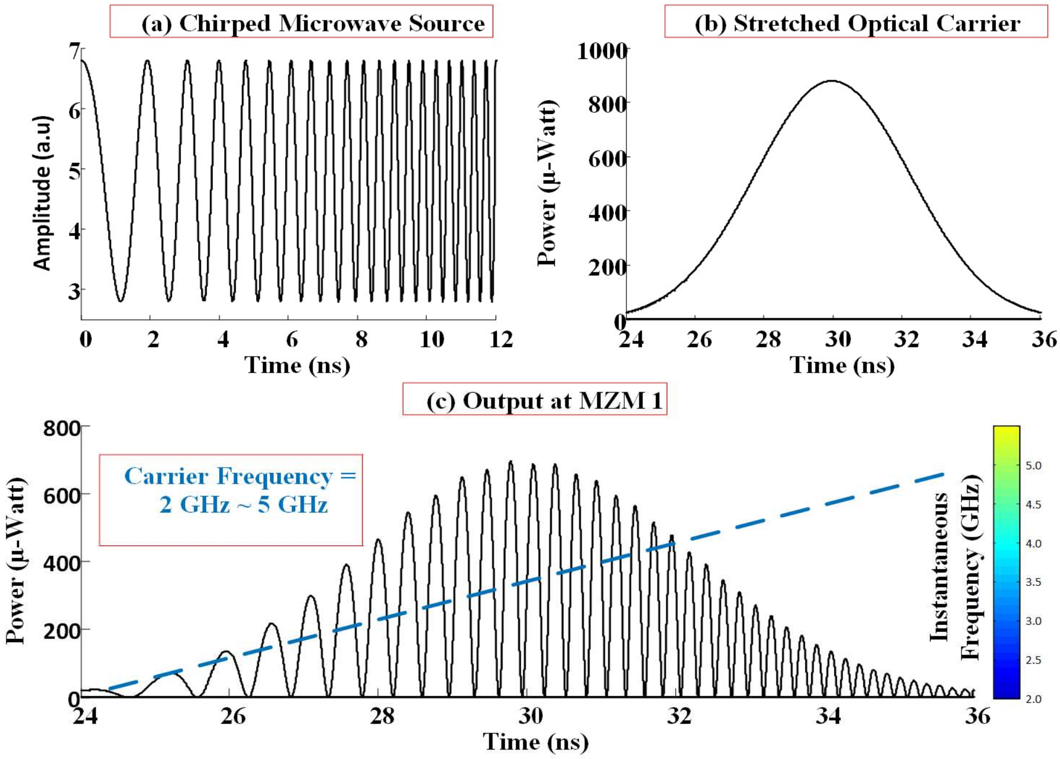

Figure 5.7 Simulation results for (a) Chirped microwave source (b) Stretched optical carrier (c) Output at MZM 1.

Figure 5.7(a) shows the chirped microwave source signal driving both MZMs and Figure 5.7(b) depicts the optical carrier over which the microwave signal is imposed on. The modulated optical pulse at the output of the first MZM is shown in Figure 5.7(c). Instantaneous modulation frequency ranges from 2 to 5 GHz. Frequency doubling due to the Double Side Band-Suppressed Carrier modulation is clearly demonstrated. The output of the second MZM is shown in Figure 5.8 (a) and MM-Wave signal obtained at PD after balanced photodetection is depicted in Figure 5.8(b). Balanced photodetection is employed not only to obtain DC-free waveform, cancel laser noise or common mode noise but also to improve the S/N ratio of the generated electrical output and thus enhance system efficiency. A 180° phase change between 2 signals at the PD; subtracting one signal from the other, signal level is doubled and phase independent noises are cancelled out. Essentially, the intensity difference between interferometer outputs cancels contributions not arising from interference between sample and reference arm. By eliminating the intensity baseline, one can use full dynamic range of the detection system and supress a large portion of intensity noise.

(a) Output at MZM 2

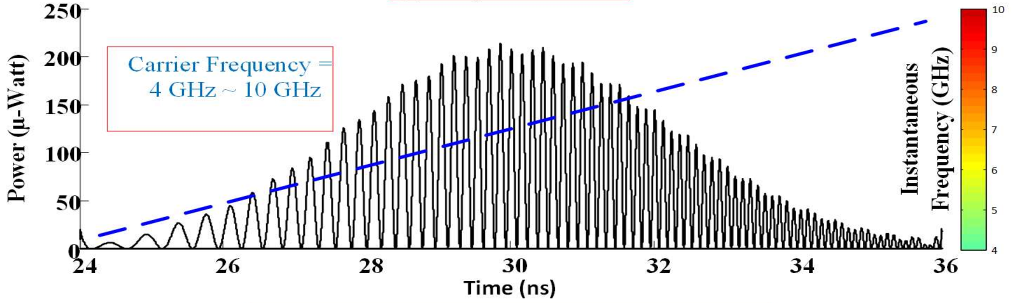

(b) Generated chirped mm/sub-mm wave pulse

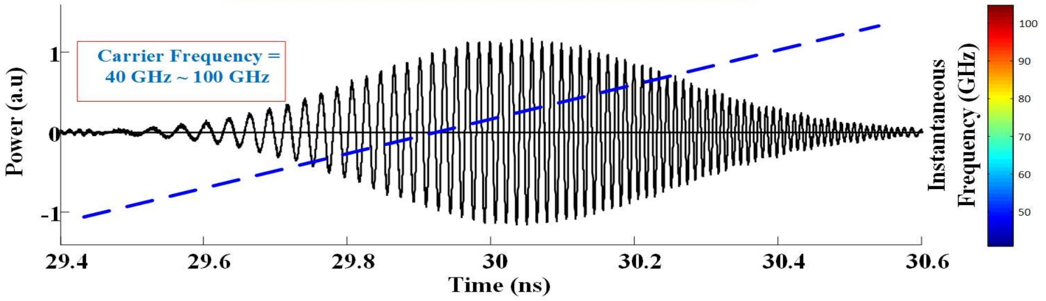

Figure 5.8 Simulation results for (a) Output at MZM 2 (b) chirped mm/sub-MM-Wave pulse output.

It is verified that cascaded modulation with proper bias and phase matching conditions offers a further 2-fold frequency multiplication.

The instantaneous modulation frequency is linearly spanning from 40 to 100 GHz. A total 40x frequency multiplication has been achieved, which agrees well with the theoretical prediction. Note that 2x multiplication comes from MITP biasing, another 2x is contributed by the cascaded modulation with proper biasing and phase matching conditions, and 10x is due to pulse compression in UB-TPS. Compared to the original microwave drive signal, an overall four-fold improvement on TBWP has been achieved on the generated frequency swept MM-Wave waveform. A novel photonic microwave frequency up-conversion scheme for generation of high-quality frequency swept MM-Wave pulses is proposed and demonstrated.

This is made possible based on unbalanced temporal optical pulse shaping in a cascaded modulation scheme. A chirped MM-Wave pulse with instantaneous frequency sweeping from 40 to 100 GHz has been generated owing to 40 times frequency up-conversion of a low-frequency chirped microwave drive signal. Both frequency multiplication ratio and TBWP of the generated MM-Wave pulse have been improved by four times compared to the conventional UB-TPS method [24 – 26].

One challenge in implementing the proposed technique is that a broadband frequency independent 90-degree microwave phase shifter is required so as to maintain the phase matching relationship as outlined in the preceding section. Conventional electronic phase shifters fall short in wideband operation. Fortunately, RF photonic phase shifters have shown superior performance, such as broader bandwidth and larger tunable range [27 - 29] and can be employed in the proposed system to provide the required wideband phase shift.

An RF photonic phase shifter may produce phase deviation from the desired value of 90°. The impact of non-ideal phase shift is investigated. A cascaded UB-TPS system with a continuous wave (CW) optical carrier centred at 193.1 THz is first studied. A single-tone microwave drive signal at 1.75 GHz is used to drive both MZMs. Power distributions among carrier and different sidebands indicate the performance of frequency multiplication. Spectral domain representations of the modulated signal by the cascaded MZMs under different phase deviations are shown in Figure 5.9.

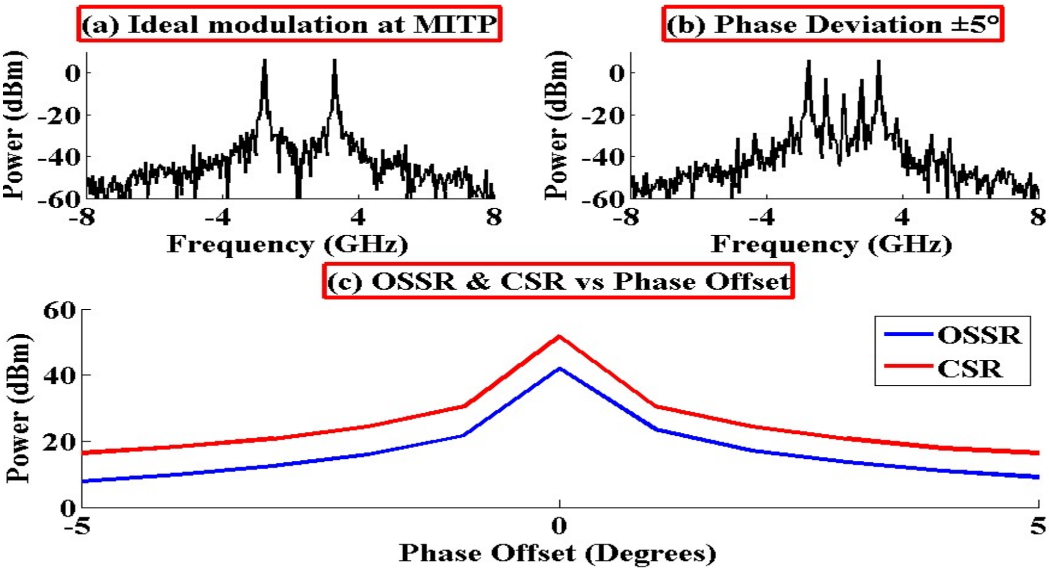

Figure 5.9 Simulation results for (a) Continuous-wave modulated at 1.75 GHz by cascaded MZMs biased at MITP. The optical carrier is supressed and first order sidebands have good strength (b) Non-ideal Phase offset of ±5° between microwave source driving both MZMs leads to carrier and adjacent sidebands gaining strength (c) OSSR and CSR vs Phase, a small deviation from the required phase condition leads to a deviation from the desired spectrum.

As shown in Figure 5.9(a), an ideal 90° microwave phase shift complete suppresses the optical carrier and additional sidebands, leading to good frequency quadrupling. However, a phase deviation of 5° results in the optical carrier gaining strength along with the first-order sidebands, as shown in Figure 5.9 (b). This will distort the frequency quadrupled signal as the harmonics interfere with the spectral purity of the modulated waveform. The Optical Sideband Suppression Ratio (OSSR) is calculated as follows:

$$OSSR = 20\log\frac{J_1(\beta_1)J_1(\beta_2)}{J_1(\beta_1)J_3(\beta_2)} \tag{5.9}$$

The OSSR represents the optical power of modulated signal sidebands relative to the carrier at various DC drive currents applied to MZM. To allow both OSSR and Carrier Suppression Ratio (CSR), which is the optical power of the carrier at various DC drive currents larger than 20 dB, a tolerable phase deviation is estimated to be ±1º. The impact of non-ideal phase shift on the generated frequency swept MM-Wave pulse is also investigated. Figure 5.10 shows the obtained MM-Wave pulses with non-ideal phase shifts. It can be seen that phase deviation of 5º will significantly distort the shape of generated waveform while the linear frequency chirp can be maintained.

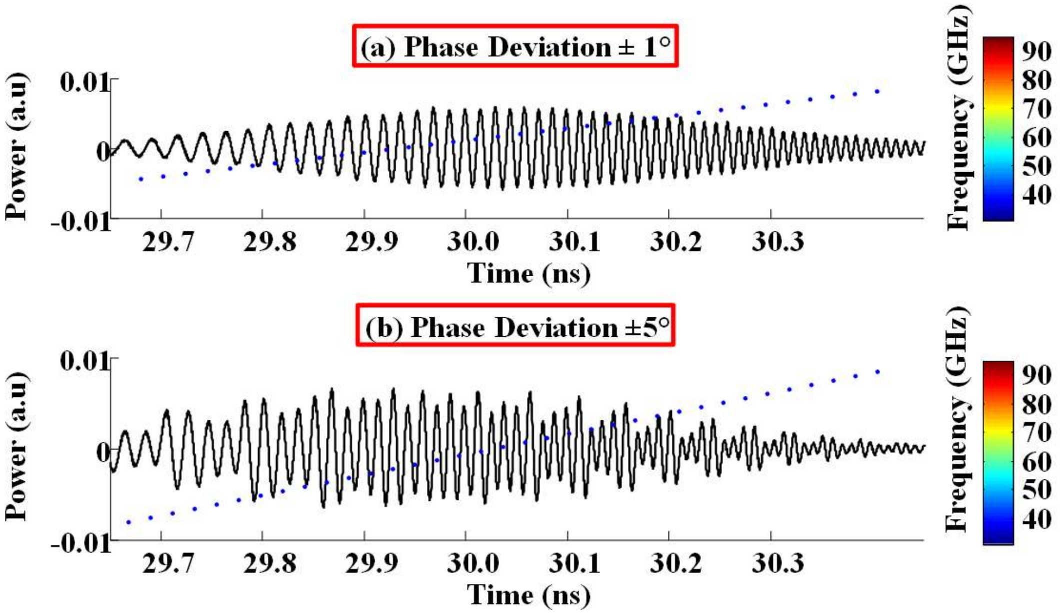

Figure 5.10 Simulation results for (a) Output at balanced PD for tolerable distortion (b) High distortion due to the large phase offset. The chirp rate is maintained for a phase mismatch of 2.5° however the signal is more distorted in time.

Recent research has improvised upon existing techniques even further by building custom-made MZM's with dual parallel and even complex configuration. Complete control over the phase terms in each arm allow-frequency up-conversion up to 8 times and beyond. However, MZMs suffer from reduced Wavelength-dependent absorption, limited modulation depth, and limited optical power handling capabilities.

An additional limitation of the technique outlined is that the use of dispersion compensation leads to pulse compression. A relatively narrow width pulse is obtained at the output. Unbalanced stretching to enhance temporal width can be achieved the output signal however would be more prone to dispersion losses in addition to losses contributed by the MZM's employed and thus low SNR. State-of-the-art MM-Wave envelope detectors have limited temporal response (~µm) wherein it is unable to capture ultrashort, fast transient signals (~ few ns) and therefore the use of cascaded MZM for chirped MM-Wave pulse generation has limited application in free space emission. Similarly, the use of bulky components such as two MZM, power sources driving MZM, optical mode-locked laser renders the system lossy, bulky, leading to poor long-term stability and ultimately expensive.

5.3.4. Differential Dispersion for Chirped Microwave Pulse Generation

An alternative approach for the generation of chirped MM-Wave pulses to be radiated in free space is proposed. Rather than active components, passive components are employed in bulk to reduce the system cost relatively and also enable a flexible chirped MM-Wave pulse generation scheme wherein chirp, signal width and central frequency can be easily tuned. An ultrashort pulse (0.8 ps) generated using a mode-locked laser at a bit rate of 50 MHz is directed towards an optical coupler. Dispersive fibres further stretch the optical pulse in each arm. The values of dispersion employed in both arms are different, $\ddot{\Phi}_{v1}$ and $\ddot{\Phi}_{v2}$ respectively. Beating two time delayed pulses at a photodetector wherein each pulse experiences a slightly different amount of dispersion yields an MM-Wave pulse with the central frequency determined by the time delay set between the two pulses and the chirp rate is determined by the dispersion difference in both arms. The frequency of the pulse duration at a moment in time t can be calculated from the following relationship [30]:

$$f = \left(\frac{\omega_1 - \omega_2 + \left(\frac{1}{\ddot{\Phi}_{v1}} - \frac{1}{\ddot{\Phi}_{v2}} \right) t}{2\pi} \right) \tag{5.10}$$

A train of MM-Wave pulses with a repetition rate dictated by the bit rate of the mode-locked laser, 50 MHz is generated. This determines the scan rate of the source when employed for non-contact sensing applications. The experimental setup is depicted in Figure 5.11. Usually, when the frequency of generated microwave signal is too high, the PD cannot respond to such a high-frequency. Thus, a limitation of the technique arises from the bandwidth of photodetector employed, and thereafter the antennae and waveguide employed for propagation and detection of the MM-Wave signal as well.

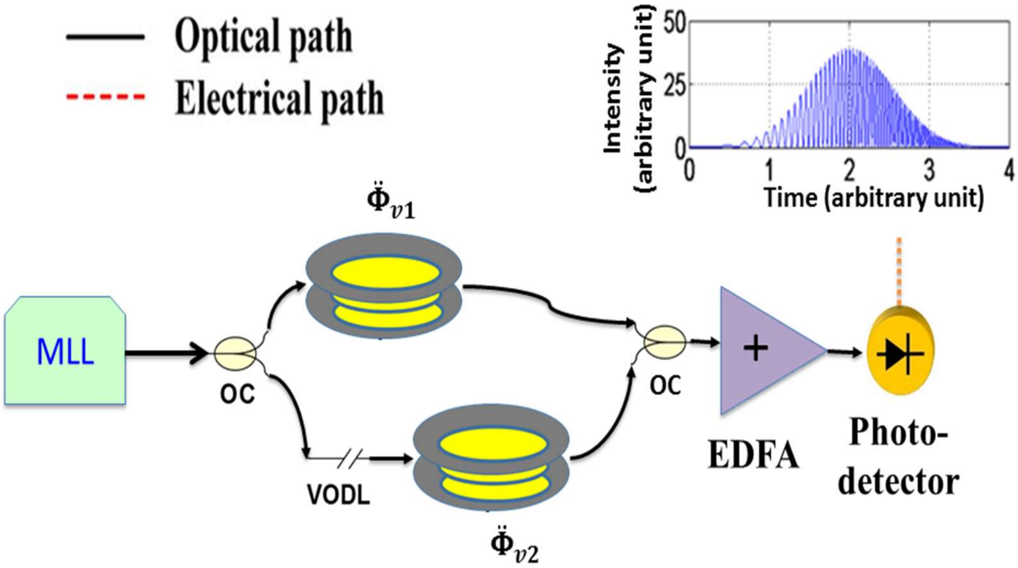

Fig 5.11 Schematic of experimental setup implemented for generation of chirped MM-Wave pulses. An ultra-short coherent broadband laser pulse train is directed to an optical coupler; the ultra-short pulse is temporally stretched in each arm by different amounts. A time delay difference between both arms determines the central frequency of the generated frequency swept pulse at the photodetector, whereas the absolute difference in dispersion determines the chirp rate.

An experimental demonstration of the proposed scheme has been verified, and the generated ultrafast swept source with both up and down chirp characteristics are depicted in Figure 5.12 (a) and (b) below. The dispersion imbalance and tunable delay are set to generate frequency swept microwave pulses with a positively chirped microwave signal, sweep rate 1.60 GHz/ns, fundamental frequency 18 GHz, and negatively chirped microwave signal with sweep rate -1.428 GHz/ns, central frequency 17 GHz respectively. The ultrafast mode-locked laser characteristics are translated to the repetition rate of generated frequency swept microwave signals and determined by the bit-rate of the laser, 50 MHz in my experiment. The experimental results for the recorded MM-Wave pulses are depicted in Figure 5.12. The flexibility of the photonic scheme for generating positively or negatively chirped MM-Wave signals and ease in adjusting required central MM-Wave frequency at the photodetector is achieved using the proposed concept.

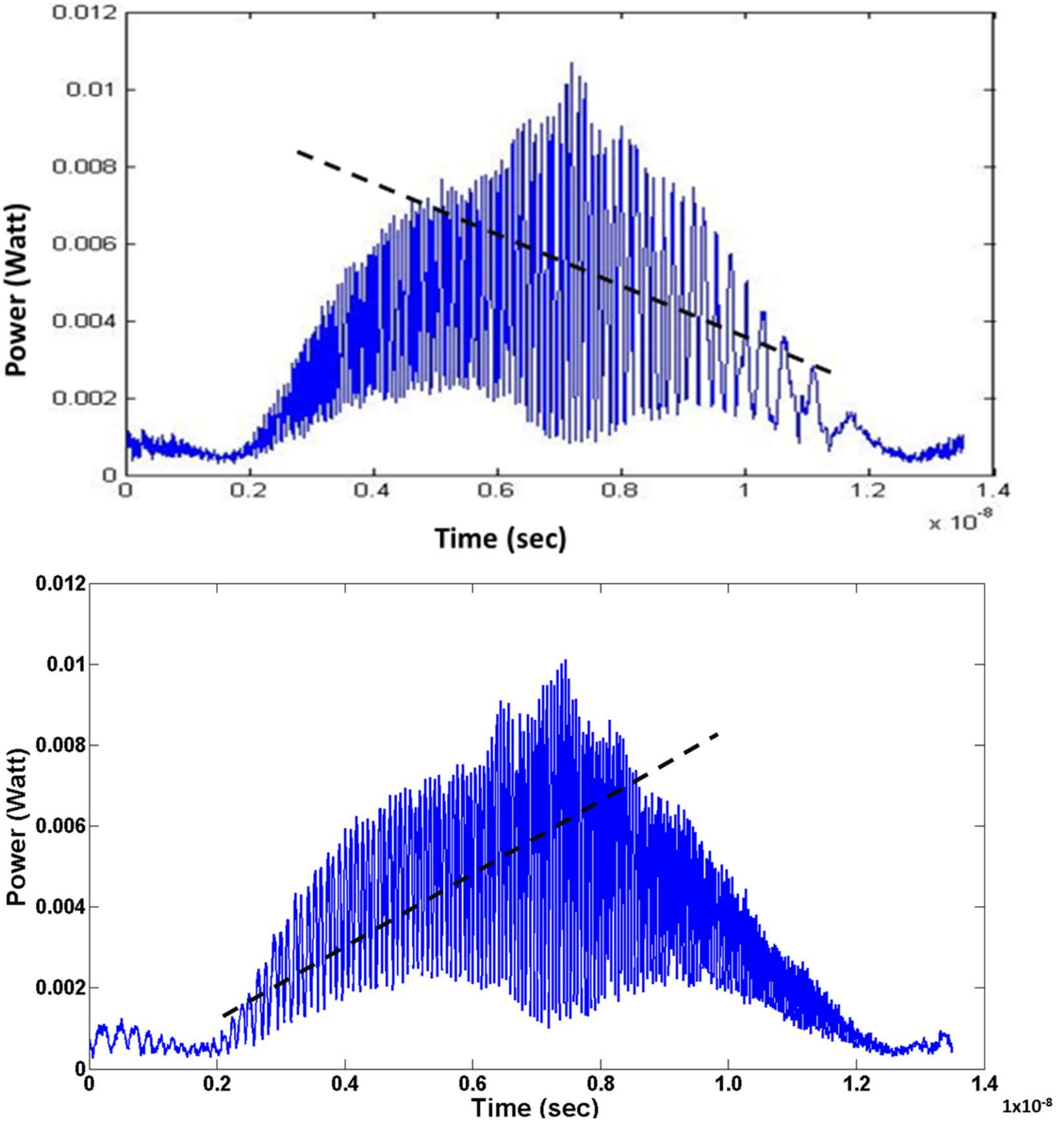

Fig 5.12 Measurement results demonstrating the capability of Photonic Time-Stretch enabled differential dispersion based ultrafast frequency swept microwave and MM-Wave generation. Slope is representing chirp direction. (a) 10 – 26 GHz (b) 26 – 8 GHz.

The central frequency is limited only by the bandwidth of photodetector employed. To verify the generation of even high-frequency signals, an optical correlator can be used to display the generated signal [31]. The ability of MM-Waves to penetrate non-conducting media make them ideal candidates for applications pertaining to security, automobile engineering, aeronautical engineering and civil engineering. Since electronics based microwave and MM-Wave generation schemes are limited in ability to generate ultrafast, frequency swept signals [32]; microwave photonics based interdisciplinary research lays the foundation for exploring high quality, novel microwave and MM-Wave sensors. The short temporal width attainable allows the possibility of achieving enhanced range resolution combined with an unprecedented axial scan rate.

As an application example of the high-speed, ultrafast frequency swept source characteristics, depth profiling based on V-band enabled coherence tomography is achieved. A quasi-optical setup attaining Michelson interferometer architecture for MM-Wave coherence tomography is realised in the next section.

5.4 MM-Wave Coherence Tomography

The ability of microwave photonics-based arbitrary waveform generation to generate frequency swept MM-Wave pulses at a repetition rate dictated by the bit rate of the laser provides sufficient motivation to explore its utility in dynamic non-contact sensing. Optical coherence tomography (OCT) is an imaging modality that takes advantage of the coherence properties of light to obtain micrometre-scale tomographic imaging of turbid media in a diverse range of applications. OCT attains imaging of turbid media by employing Michelson interferometer architecture. Interferometric methods rely on phase difference measurement between the reference and sample arms. The depth information can be computed very fast and very precisely. Usually the depth resolution is in the range of the wavelength of the used electromagnetic band [39]. We therefore investigate the OCT system concept applied to MM-Wave coherence tomography. Rather than using visible light as the source, MM-Waves can be employed for resolving depth profile of material samples.

Conventionally, swept source MM-Wave coherence tomography has limited scanning speed due to the fact that conventional MM-Wave source has slow sweeping rate (~ 100 kHz). Photonics-assisted solution based on heterodyne detection [36, 37] offers improved scanning speed but still limited by the tuning speed of a wavelength swept laser source. With the aid of a microwave photonic generation scheme as studied in section 5.3.4, an ultrafast frequency-swept MM-Wave source with fringe visibility determined by power in each interferometer arms and frequency sweep rate determined by dispersion imbalance leads to a unique source that enables high throughput MM-Wave coherence tomography. Since real-time dynamic sensing scenarios for autonomous cars and related technology are conceptualized, thus, MM-Wave source with fast sweep rate and pulse repetition rate is desired. In this section, pure MM-Wave coherence tomography is investigated which will pave the way towards high-throughput and ultrafast sensing and imaging in MM-Wave. Comparing the MM-Wave interferometry results to well-established Time-of-Flight (TOF) method concludes the section and the utility of the proposed photonics-based chirp MM-Wave source is also proposed for TOF and Frequency Modulated Continuous Wave RADAR systems.

5.4.1. Experimental setup and Results

In order to characterise such a system, we utilise an MVNA-based setup. In a Michelson interferometer structure, a 3 dB beam splitter working in the frequency band of interest is a key component. Firstly, an experimental calibration scheme for finding an accurate beam splitter in the V-band of the electromagnetic spectrum is realised. A simplified diagram of the quasi-optical set up characterising the sample material to be used as MM-Wave beam splitter is depicted in Figure 5.13.

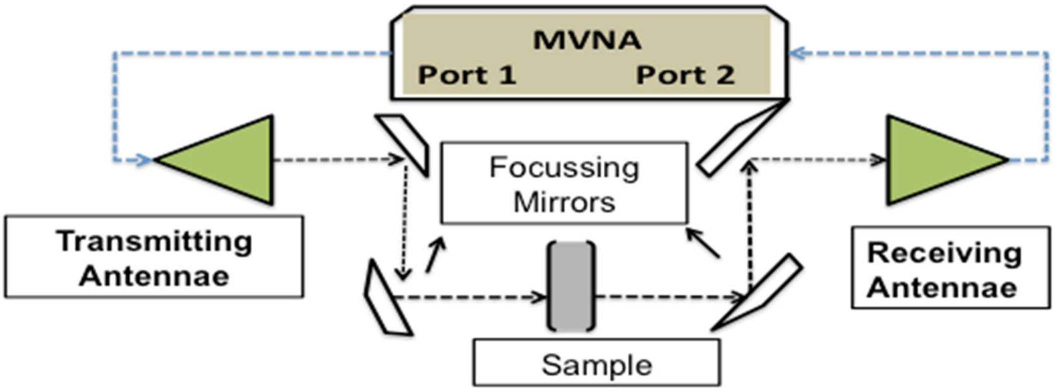

Figure 5.13 Quasi-Optical set-up for MM-Wave beam splitter characterisation. Incident MM-Wave signal is transmitted to the sample under test fixed at 45-degree angle to normal. The transmitted signal received at port 2. S-parameters relating sample transmission and reflection coefficient to incident spectrum can be thereon evaluated.

A mylar sheet sample of thickness 500 μm is characterised as a 50/50 beam splitter. Figure 5.13 depicts the setup employed for determining the transmission characteristics of the mylar sheet at a 45° incidence angle relative to reflection from a pure reflector; and pure transmission without any sample while recording S_{21} parameters through a quasi-optical system. The transmission scattering parameter, S_{11} and S_{21} is depicted in Figure 5.14. The resulting transmission parameters, S_{21} is a good indicator for the ability of the mylar substrate allowing equally partial transmission and reflection at 45 degrees angle relative to the incident beam. A 3 dB difference in through transmission and transmission through a mylar sample is observed.

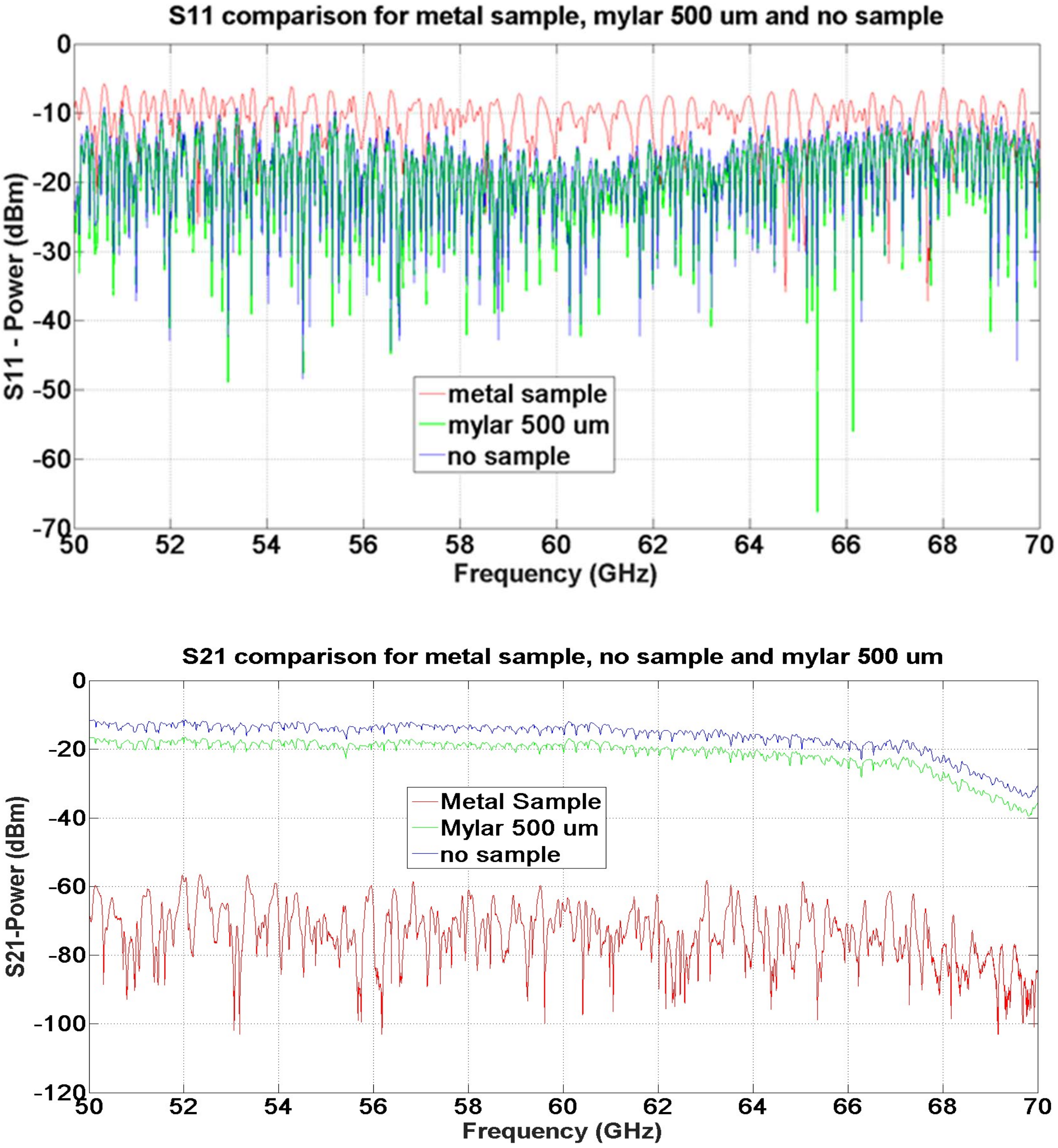

Figure 5.14 The corresponding transmission profile relative to a full metal reflector sample and transmission without any sample.

Simulations in G-solver also verify the ability of mylar to act as a 50/50 beam splitter in the V-band of the MM-Wave spectrum. A 3 dB beam splitter in the frequency band of interest is a key component since the power in each interferometer arms determines the visibility of the interference fringes. Further on, an implementation of the proof-of-concept is demonstrated using an MVNA source. A transmitting antenna emits the generated MM-Wave signal directed to a Michelson interferometer structure with focusing mirrors serving as the reflectors. Sweeping the MM-Wave signals across the V-band and recording the spectral interference pattern as depicted in Figure 5.15. In the figure shown, initially both arms are maintained at an equal path length. Modulation observed in interference spectrum could be attributed to a frequency dependent free space attenuation of the propagating V-band spectrum. Thus, the initial equal path length calibration serves as the baseline calibration, the measurement results with the Sample Under Test are divided by the recorded results of the calibration measurement.

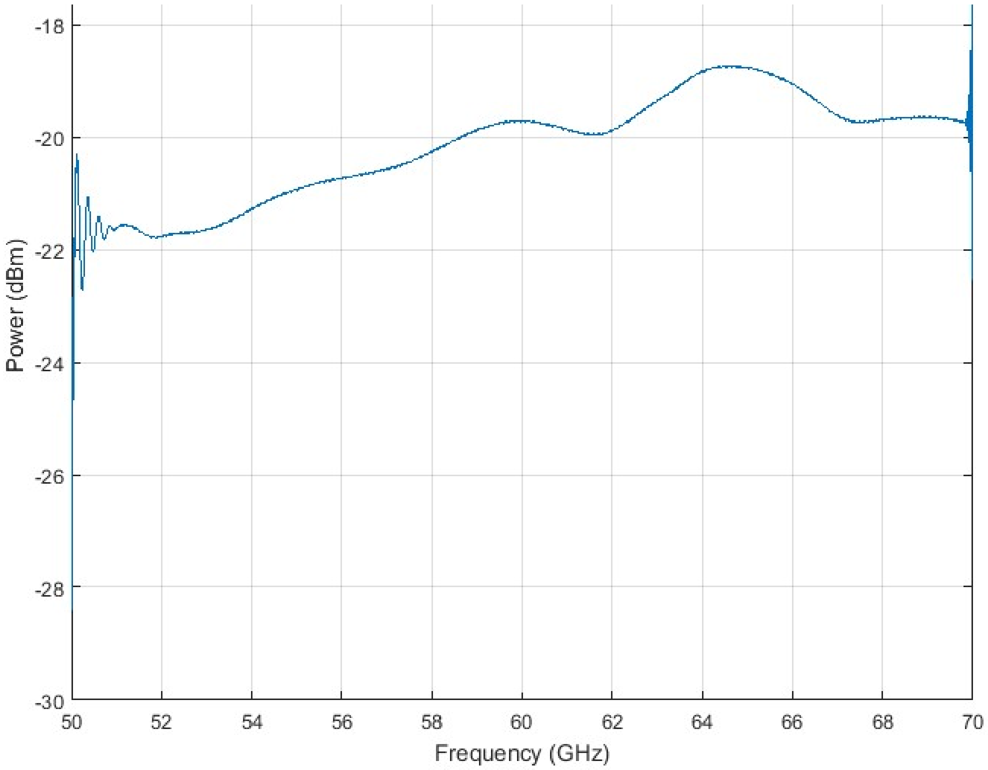

Figure 5.15 Interference Spectrum for sample arm and reference arm maintained at an equal path length difference.

Further-on, one of the arms termed as the sample arm is de-tuned with respect to the reference arm. An interference pattern obtained for relative path length difference,

ΔL of 15 mm is shown in Figure 5.16 and 5.17. An FSR of 10 GHz is obtained which match very well with theoretical prediction of $FSR = \frac{c}{2\Delta L}$. Some faster oscillation is observed as well on top of the main interference pattern. This is due to the relatively small path length difference allowing strong resonance frequency at ten times the path length difference.

Path length differences of 30 mm, 45 mm, 60 mm and 75 mm correspond to FSR of 5 GHz, 3.33 GHz, 2.5 GHz and 2 GHz respectively. A clear distinction in the FSR and power profile can be observed for various relative path lengths. An extreme comparison of FSR for variable path lengths of 15 mm and 90 mm (FSR = 1.67 GHz) are recorded and depicted for comparison as shown in Figure 5.16.

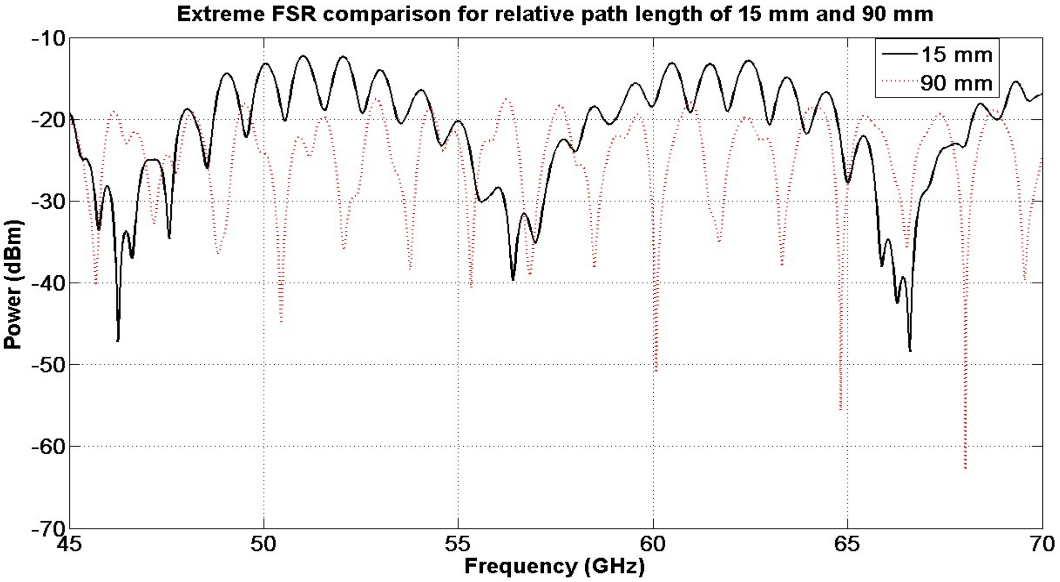

Figure 5.16 Interference Spectrum comparison for sample arm and reference arm maintained at path length difference of 15 mm and 90 mm respectively.

An FFT of the acquired raw data generates a line scan profile with the peak position denoting the path length difference between the reference and sample arm as shown in Figure 5.17. A path length difference between the sample and reference arms can be related to reflections from samples of variable thickness. A set of measurement for path length differences up to 150 mm were recorded.

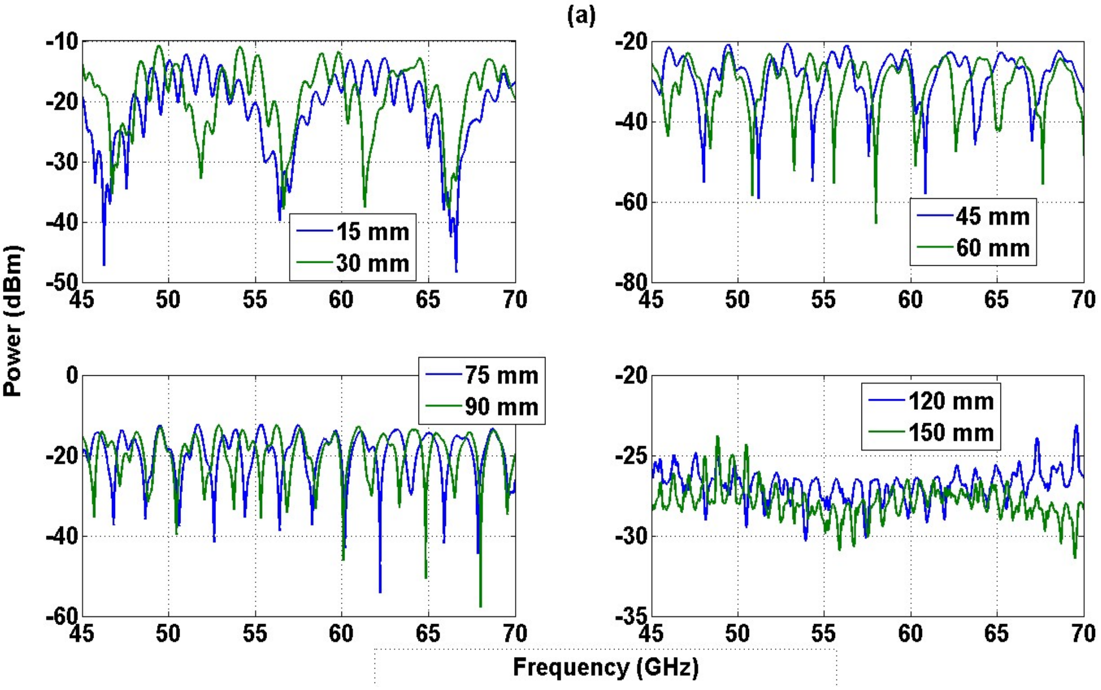

(b) Line scan profile obtained from IFFT of interference spectrum

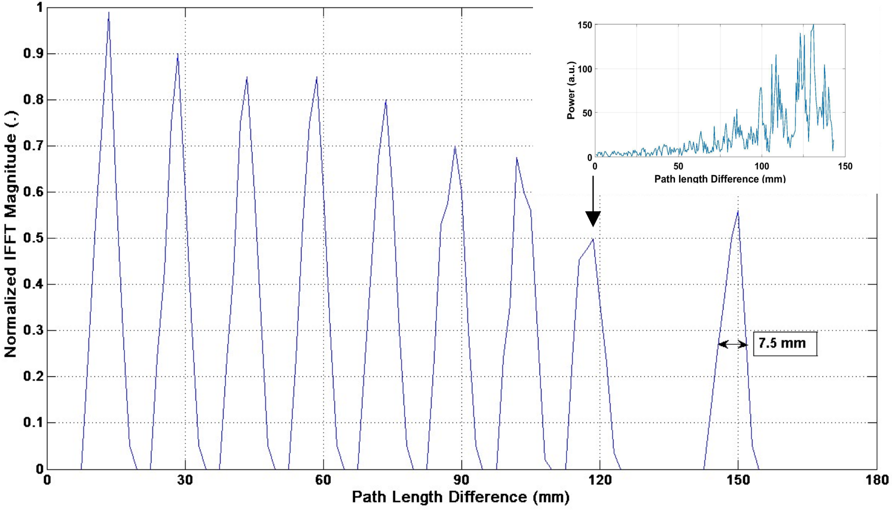

Figure 5.17 (a) Interference Spectrum Comparison for Optical Path Length Differences between reference and sample arm; (b) IFFT of interference spectra denoting a change in axial position. The noise is eliminated for better visual comparison, inset shows FFT of raw data for 120 mm path length difference. Peak with highest amplitude that corresponds to known path length difference is the corresponding axial line scan

The axial resolution is determined by calculating the width of the IFFT plot denoting pulse position. A decrease in the FSR obtained as a result of an increasing path length difference is clearly observed. The resolution is estimated as 7.5 mm. The FFT of interference spectrum at 150 mm has a higher magnitude as the incident power is not the same in all measurements. At 150 mm path length difference, the incident power is 0 dBm as compared to -5 dBm for the other test cases. Arbitrary units are used to show the ratio of

IFFT peak relative to IFFT peak obtained at equal path length. As a test case, interference spectrum for turbid media such as Teflon 50 mm thick placed in sample arm is recorded.

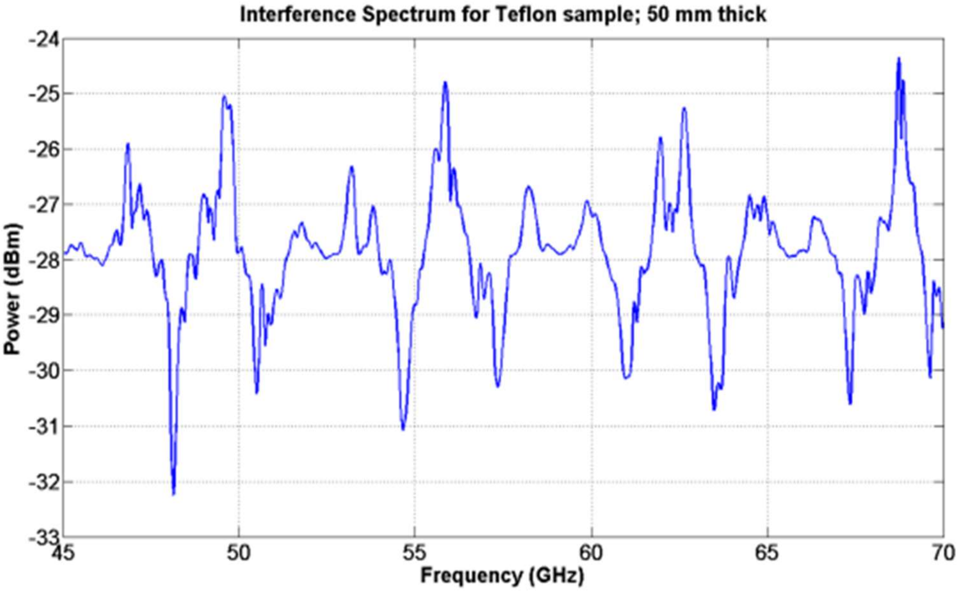

Figure 5.18 Interference Spectrum Comparison for 50 mm thick Teflon plate introduced in sample arm.

Since a Teflon sample is translucent to electromagnetic waves in the V-band; incident electromagnetic waves are partially transmitted and partially reflected at the sample interface. High scattering from the material sample and weak reflection adds phase noise to the signal captured. Noise instability, MM-Wave beam divergence and scattering from sharp corners lead to unexpected jump along the spectral profile. An IFFT of the interference spectrum depicts multiple scattering interfaces as shown in Figure 5.19. With increasing relative path length differences, transmission power drops as well. Problems related to specular scattering from targets resulting in fluctuation in target return amplitude. Multiple bounces generate noise in spectral phase. Since the experimental results in Figure 5.17 and 5.18 demonstrate a constant axial resolution of 7.5 mm, the peaks in Figure 5.19 are assumed to be peaks arising from the noise floor. The resulting return signal is thus buried in noise and a false depth profiling is observed [38]. Definitive results for material depth profiling has not been successfully achieved, however, the ability of the MM-Wave interferometer to encode displacement in path lengths is demonstrated. The fringe visibility decreases as well due to power imbalance between the two-interferometer arms.

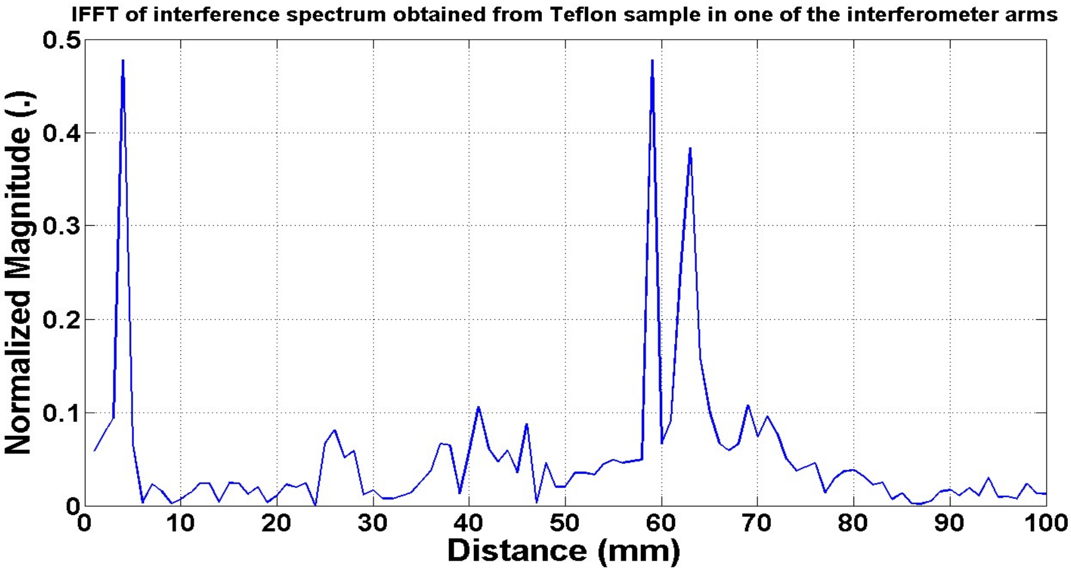

Figure 5.19 IFFT plot for a 50 mm thick Teflon plate introduced in sample arm.

5.4.2. Detection

Research to measure individual components, such as the source and detector performance, is essential to understand the combined effect of all of their associated limitations within a non-contact measurement system. An MM-Wave (V-band) envelope/amplitude detector (HFD15P) can be used for detecting the photonics based high-speed interfered MM-Wave pulse output. The high-frequency output from MM-Wave interferometer are picked up by the envelope detector and as the name implies only the signal envelope encoding the low-frequency interference pattern is detected by the amplitude detector. In order to characterise the temporal response of the amplitude detector, an MM-Wave signal is generated by heterodyne beating between two optical signals separated by the required MM-Wave frequency. One of the lasing wavelength is kept fixed, and the other lasing wavelengths is tuned across a particular frequency band to generate an MM-Wave signal with different carrier frequency. One of the lasing wavelengths is modulated with a low-frequency RF signal, and the envelope of modulated MM-Wave signal is detected by the MM-Wave amplitude detector. An electrical spectrum analyser is used to measure the spectrum of modulated MM-Wave signal. By sweeping the RF modulation frequency and measuring the detected RF spectrum, we can effectively characterise the response bandwidth of the MM-Wave amplitude detector. The setup is depicted in Figure 5.20.

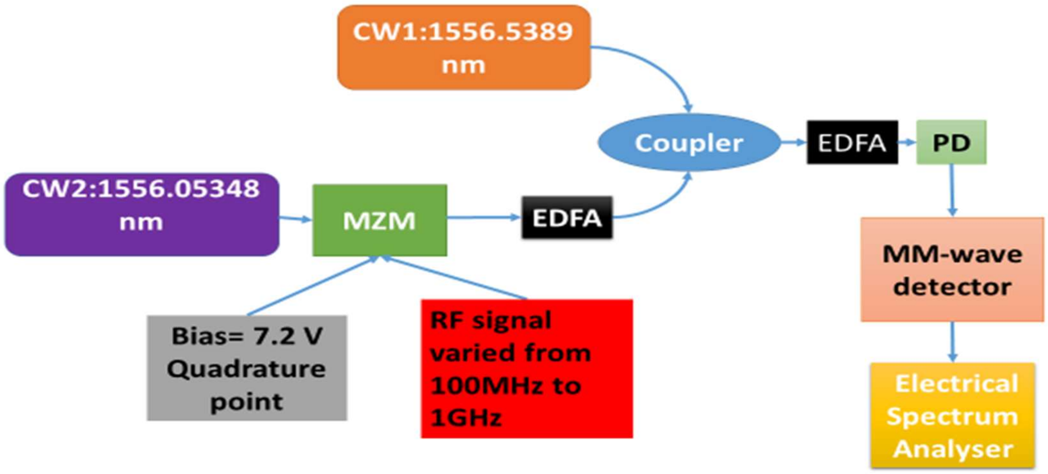

Figure 5.20 Experimental setup for characterising temporal response of potential state-of-the-art MM-Wave envelope detector.

The method basis proposed for MM-Wave CT promises to attain high throughput non-destructive evaluation of turbid media, however, the system size and system complexity renders the method costly and complicated. A measure of the electrical power versus frequency sweep is plotted in Figure 5.21. The 5 dB response bandwidth of the mm-wave envelop detection is 400 MHz. To work with the photonics-assisted high-throughput frequency swept mm-wave source, a new mm-wave envelope detection with much higher response bandwidth (>1 GHz) would be required.

The power output from a photodetector is extremely weak and thus measure of signal characteristics reveal an inability of the amplitude detector to measure high-speed and thus high-frequency amplitude modulation. The use of optical and MM-Wave amplifiers introduces a lot of non-linearity and thus corrupting the signal with high phase noise. Novel algorithms and improvement in state-of-the-art MM-Wave envelope detectors can address these challenges.

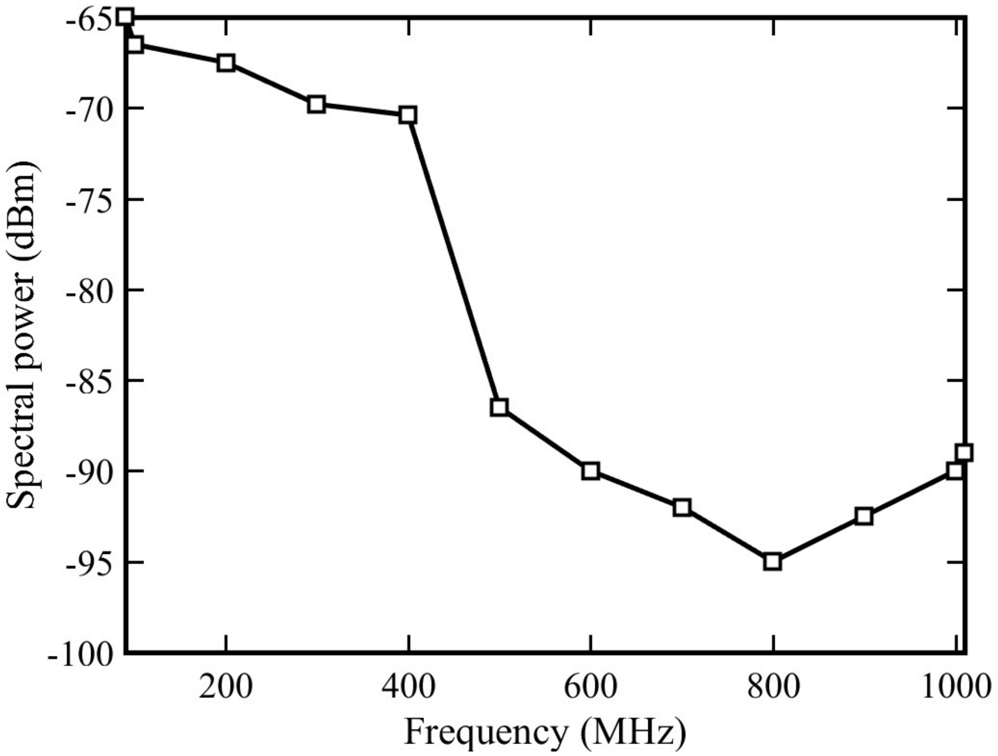

Figure 5.21 Measured transient characteristics of MM-Wave envelope detector.

It is important to point out that the primary goal of demonstrating pure MM-Wave coherence tomography is to demonstrate the feasibility of MM-Wave coherence tomography and its utility as a high throughput non-contact sensor. Short pulse, wide bandwidth and ultrafast frequency sweep characteristics of a photonic source can be utilised for high speed measurement. The high throughput photonics based MM-Wave coherence tomography proposition opens the gateway to high speed and high precision metrology.

5.5 Photonic MM-Wave Source for TOF & RADAR

The proposed photonics-based MM-Wave source could be utilised as a potential source for TOF and FMCW RADAR as well. The ultrashort temporal profile and broad bandwidth capability allows the utility of the source in a direct non-contact measurement scheme rather than an interferometric-based non-contact sensing scheme. An interferometric system is inherently limited due to its precise stability requirement; mechanical and thermal isolation is usually desired to obtain accurate results. In addition, interferometry-based investigations work best when sample under test has a smoother surface profile. A rough surface would yield scattering in different directions resulting in diminishing visibility of the interference signal recorded at the detector. Interferometric methods are best suited for high precision measurements of small objects in a scientific or industrial environment [39]. The Time-Of-Flight (TOF) and FMCW RADAR are measurement concepts that are extensively used in the MM-Wave and THz band. TOF and FMCW RADAR are utilised extensively for long range sensing in security and automotive applications. In TOF technique, a short broadband pulse is directed to a sample under test, the measured reflected or transmitted signal is analysed to calculate the associated amplitude reduction and phase delay. However, TOF measurement required emitted signal to have high instantaneous power resulting in a large and expensive system requirement. FMCW RADAR achieves similar results using much smaller incident power by emitting periodic pulses whose frequency varies linearly with time. The distance relative to the target is determined from the frequency difference between received and emitted signal. The range or depth resolution depends on the used bandwidth and roughness of sample under test, and varies between 0.4 mm and 3 mm [36]. The experimental results are not able to provide a definitive advantage of MM-Wave CT over ToF and FMCW RADAR, however the results do show promise for a similar system to be developed. Future work is needed to quantify the performance of a high throughput photonics-based source in MM-Wave non-contact sensing scheme.

5.6 Summary

In this chapter photonics-based microwave and MM-Wave generation for emission in free space is explored, improvised upon and experimentally demonstrated. The unique source is explored for its potential use as a high throughput Non-Contact Measurement System. Limitation in suitable wideband photodetector and broadband MM-Wave envelope detector render the system costly and complicated for practical use in the higher frequency and THz regime. The resolution obtained is limited by the total bandwidth employed and central frequency used. Similarly, real-time instruments for capturing ultrafast signals hampers state-of-the-art realisation. However, a proof-of-concept demonstration realises the potential use of the system as a real-time dynamic non-contact sensing tool.

REFERENCES

[1] L. Wangzhe and Y. Jianping, "Investigation of Photonically Assisted Microwave Frequency Multiplication Based on External Modulation," *Microwave Theory and Techniques, IEEE Transactions on*, vol. 58, pp. 3259-3268, 2010.

[2] Q. Guohua, Y. Jianping, J. Seregelyi, S. Paquet, and C. Belisle, "Generation and distribution of a wide-band continuously tunable millimeter-wave signal with an optical external modulation technique," *Microwave Theory and Techniques, IEEE Transactions on*, vol. 53, pp. 3090-3097, 2005.

[3] L. Chun-Ting, J. J. Chen, D. Sheng-Peng, P. Peng-Chun, and C. Sien, "Impact of Nonlinear Transfer Function and Imperfect Splitting Ratio of MZM on Optical Up-Conversion Employing Double Sideband With Carrier Suppression Modulation," *Lightwave Technology, Journal of*, vol. 26, pp. 2449-2459, 2008.

[4] C. Hao and Y. Jianping, "Frequency Quadrupling and Upconversion in a Radio Over Fibre Link," *Lightwave Technology, Journal of*, vol. 26, pp. 2706-2711, 2008.

[5] R. Ashrafi, M. R. Dizaji, L. R. Cortés, J. Zhang, J. Yao, J. Azaña and L. R. Chen, "Time-delay to intensity mapping based on a second-order optical integrator: application to optical arbitrary waveform generation," *Optics Express,* vol. 23, pp. 16209-1622, 2015.

[6] C. Hao, Z. Fei and Y. Jianping, "Photonic Generation of Microwave Signals Based on Pulse Shaping," *IEEE Photonics Technology Letters,* vol. 19, pp. 668-670, 2007.

[7] W. Chao and Y. Jianping, "Microwave and millimeter-wave arbitrary waveform generation and processing using fibre-optics-based techniques," in *Broadband Network & Multimedia Technology, IC-BNMT '09, 2nd IEEE International Conference on*, 2009.

[8] W. Chao and Y. Jianping, "Simultaneous Optical Spectral Shaping and Wavelength-to-Time Mapping for Photonic Microwave Arbitrary Waveform Generation," *IEEE Photonics Technology Letters,* vol. 21, pp. 793-795, 2009.

[9] W. Chao, L. Ming and Y. Jianping, "Continuously Tunable Photonic Microwave Frequency Multiplication by Use of an Unbalanced Temporal Pulse Shaping System," *IEEE Photonics Technology Letters,* vol. 22, pp. 1285-1287, 2010.

[10] W. Jia Haur, S. Aditya, L. Peng Huei, P. P. Shum, L. Huy Quoc and K. E. K. Lee, "Photonic generation of microwave pulses with wide frequency multiplication tuning range," in *Photonics Global Conference (PGC)*, 2012.

[11] Chou, Y. Han and B. Jalali, "Adaptive RF-photonic arbitrary waveform generator," in *Microwave Photonics, 2002. International Topical Meeting on*, 2002.

[12] A. Dezfooliyan and A. M. Weiner, "Photonic synthesis of high fidelity microwave arbitrary waveforms using near field frequency to time mapping," *Optics Express,* vol. 21, pp. 22974-22987, 2013.

[13] Z. Jiang, D. E. Leaird and A. M. Weiner, "Line-by-Line Pulse Shaping Control for Optical Arbitrary Waveform Generation," *in Conference on Lasers and Electro-Optics/Quantum Electronics and Laser Science Conference and Photonic Applications Systems Technologies*, Long Beach, California , 2006.

[14] A. Rashidinejad, D. E. Leaird and A. M. Weiner, "Ultrabroadband radio-frequency arbitrary waveform generation with high-speed phase and amplitude modulation capability," *Optics Express,* vol. 23, pp. 12265-12273, 2015.

[15] L. Wangzhe and Y. Jianping, "Microwave and Terahertz Generation Based on Photonically Assisted Microwave Frequency Twelvetupling With Large Tunability," *Photonics Journal, IEEE,* vol. 2, pp. 954-959, 2010.

[16] X. Chen, Z. Liu, C. Jiang, and D. Huang, "A Filterless Optical Millimeter-Wave Generation based on Frequency 16-tupling," in *Asia Communications and Photonics Conference 2013*, Beijing, 2013.

[17] L. Chun-Ting, S. Po-Tsung, J. J. Chen, X. Wen-Qiang, P. Peng-Chun, and C. Sien, "Optical Millimeter-Wave Signal Generation Using Frequency Quadrupling Technique and No Optical Filtering," *Photonics Technology Letters, IEEE*, vol. 20, pp. 1027-1029, 2008.

[18] C. Hao and Y. Jianping, "All-Fibre Chirped Microwave Pulses Generation Based on Spectral Shaping and Wavelength-to-Time Conversion," *Microwave Theory and Techniques, IEEE Transactions on,* vol. 55, pp. 1958-1963, 2007.

[19] L. Wei, L. Ming, W. Lixian, Z. H. Ning, “Photonic Generation of Binary Phase-Coded Microwave Signals With Large Frequency Tunability Using a Dual-Parallel Mach–Zehnder Modulator”, *Photonics Journal, IEEE*, 2013.

[20] I. S. Lin, J. D. McKinney and A. M. Weiner, "Photonic synthesis of broadband microwave arbitrary waveforms applicable to ultra-wideband communication," *IEEE Microwave and Wireless Components Letters,* vol. 15, pp. 226-228, 2005.

[21] J. Yao, "Photonic generation of microwave arbitrary waveforms," *Optics Communications,* vol. 284, pp. 3723-3736, 2011.

[22] L. Ming, W. Chao, L. Wangzhe and Y. Jianping, "An Unbalanced Temporal Pulse-Shaping System for Chirped Microwave Waveform Generation," *Microwave Theory and Techniques, IEEE Transactions on,* vol. 58, pp. 2968-2975, 2010.

[23] W. Chao and Y. Jianping, "Photonic Generation of Chirped Millimeter-Wave Pulses Based on Nonlinear Frequency-to-Time Mapping in a Nonlinearly Chirped Fibre Bragg Grating," *Microwave Theory and Techniques, IEEE Transactions on,* vol. 56, pp. 542-553, 2008.

[24] L. Ming and Y. Jianping, "Photonic Generation of Continuously Tunable Chirped Microwave Waveforms Based on a Temporal Interferometer Incorporating an Optically Pumped Linearly Chirped Fibre Bragg Grating," *Microwave Theory and Techniques, IEEE Transaction,* vol. 59, pp. 3531-3537, 2011.

[25] W. Li and J. Yao, "Generation of Linearly Chirped Microwave Waveform With an Increased Time-Bandwidth Product Based on a Tunable Optoelectronic Oscillator and a Recirculating Phase Modulation Loop," in *Journal of Lightwave Technology*, vol. 32, no. 20, pp. 3573-3579, 2014.

[26] M. Ming, M. Rochette and L. R. Chen, "Generating Chirped Microwave Pulses Using an Integrated Distributed Fabry Perot Cavity in Silicon-on-Insulator," *Photonics Journal, IEEE,* vol. 7, pp. 1-6, 2015.

[27] J. H. Wong, H. Q. Lam, S. Aditya, K. E. K. Lee, V. Wong, L. Peng Huei, K. Wu, C. Ouyang and P. P. Shum, "Photonic Generation of Tunable Continuous-Wave Microwave Signals Using a Temporally-Stretched and Chirped Pulse-Train," *Lightwave Technology, Journal,* vol. 30, pp. 1269-1277, 2012.

[28] F. Zhang, X. Ge and S. Pan, "Background-free pulsed microwave signal generation based on spectral shaping and frequency-to-time mapping," *Photonics Research,* vol. 2, pp. B5-B10, 2014.

[29] Z. Weifeng, Z. Jiejun and Y. Jianping, "Largely chirped microwave waveform generation using a silicon-based on-chip optical spectral shaper," in *Microwave Photonics (MWP) and the 2014 9th Asia-Pacific Microwave Photonics Conference (APMP), 2014 International Topical Meeting on*, 2014.

[30] Y. Xu, Z. Shi, H. Chi, X. Jin, S. Zheng, and X. Zhang, "Relaxed dispersion requirement in the generation of chirped RF signals based on frequency-to-time mapping," *Optics Communications*, vol. 331, pp. 278-281, 2014.

[31] M. Bolea, J. Mora, L. R. Chen, and J. Capmany, "Highly Chirped Reconfigurable Microwave Photonic Filter," *Photonics Technology Letters, IEEE*, vol. 23, pp. 1192-1194, 2011.

[32] C. Li *et al.*, "A Review on Recent Progress of Portable Short-Range Noncontact Microwave Radar Systems," in *IEEE Transactions on Microwave Theory and Techniques*, vol. 65, no. 5, pp. 1692-1706, 2017.

[33] A.Y. Nashashibi, K. Sarabandi, P. Frantzis, R.D. De Roo, and F.T. Ulaby, "An ultrafast wide-band millimeter-wave (MMW) polarimetric radar for remote sensing applications," *IEEE Transaction on Geoscience and Remote Sensing*, vol. 40, pp. 1777-1786, 2002.

[34] M. Miyakawa and J.Ch. Bolomey, "Microwave imaging I: microwave computed tomography," in *Non-Invasive Thermometry of the Human Body*: CRC Press, 1995, pp. 105-126.

[35] G.G. Brown, B.C. Dian, K.O. Douglass, S.M. Geyer, S.T. Shipman, and B.H. Pate, "A broadband Fourier transform microwave spectrometer based on chirped pulse excitation," *Review of Scientific Instruments*, vol. 79, 2008.

[36] T. Nagatsuma, H. Nishii, and T. Ikeo, "Terahertz imaging based on optical coherence tomography [Invited]," *Photonics Research*, vol. 2, pp. B64-B69, 2014.

[37] T. Ikeou, T. Isogawa, K. Ajito, N. Kukutsu and T. Nagatsuma, "Terahertz imaging using swept source optical-coherence-tomography techniques," *IEEE International Topical Meeting on Microwave Photonics*, pp. 290-293, Noordwijk, 2012.

[38] A. T. Abdalla, M. T. Alkhodary and A. H. Muqaibel, "Multipath Ghosts in Through-the-Wall Radar Imaging: Challenges and Solutions". *ETRI Journal*, vol. 40, pp. 376-388, 2018.

[39] M. Schmidt. 2011, *Analysis, Modeling and Dynamic Optimisation of 3D Time-of-Flight Imaging Systems* (Doctoral dissertation). Retrieved from: https://mafiadoc.com/dissertation-universitat-heidelberg_5a50b6d91723dd805ce5d2b7.html

CHAPTER 6

CONCLUSION

6.1 Summary

This final chapter concludes the thesis and an attempt specifying future research direction is outlined. The broad aim of this thesis was to advance the state-of-the-art in Photonics-based MM-Wave and microwave measurement and generation schemes by exploiting the potential applications pertaining to real-time FBG strain sensing, non-invasive dimensional metrology and MM-Wave coherence tomography utilising microwave photonic techniques. Both fibre and free-space based sensing applications are extensively investigated and a Photonic Time-Stretch based demodulation scheme proposed and implemented.

In this thesis, photonic Time-Stretch based MM-Wave generation is explored and improved upon. Previous works have analysed and implemented photonic generation of MM-Wave signals, but here, the applications for high throughput measurements of fibre grating sensors and Non-Contact Sensing for optical path length difference calculation in a Michelson interferometer are implemented. High throughput refers to the ultrafast speed attained due to the mode-locked laser bit rate, which translates to the generated microwave and MM-Wave pulse repetition rate. Further, the previous works on MM-Wave and THz generation are more focused towards RoF or THz wireless communication for improving MIMO systems based on commercial products. However, we combine the ultrafast mode-locked laser dynamics with the principle of photonic Time-Stretch and Photonics-based MM-Wave generation for high throughput measurements. The constraints and challenges in its implementation have also been outlined.

The principal achievements of this thesis are as follows:

- Enabling photonic Time-Stretch to analyse spectral content as a temporal analogue allows covering a range of applications that were traditionally limited to slow spectroscopic measurement techniques hampering its use in monitoring real-time dynamic events.

- Ultrafast and ultrahigh-resolution interrogation of a chirped fibre Bragg grating for strain evaluation can be employed in a novel demodulation scheme allowing temperature independent, intra-grating strain sensing along the length of the chirped fibre Bragg grating. Conventional schemes targeting fibre grating strain interrogation measure the average value of strain, the intra-grating scheme proposed builds on existing intra-grating strain sensing and develops a high-speed intra-grating solution. Real time structural analysis of infrastructure at sensitive contact points enables hot-spot localized strain evaluation. The experiments are conducted in lab environment with one grating acting as the reference grating shielded from external perturbation and fixed closely to the sensor grating in a Michelson interferometer configuration. Temperature change has minimum influence on strain measurement since the two CFBGs have relatively short lengths and are placed in close proximity. Temperature change will lead to an identical change to the wavelengths of the two CFBGs; thus, the relative distance between the two CFBGs essentially remains unchanged, making the beat frequency independent of the environmental temperature change.

- Dimensional metrology of infrared transparent samples can be obtained via a novel demodulation scheme employing microwave pulse generation. A high-speed real-time sensing solution benefits from applications as an online industry-monitoring tool. The proposed concept is considered suitable for thin film sensing with applications in the microelectronics, semi-conductor and packaging industry.

- MZMs biased at minimum transmission point and cascaded in series can be utilised to generate chirped microwave and MM-Wave pulses with enhanced TBWP. The experimental challenge in its implementation needs to be addressed.

- Differential dispersion based interferometry applied for generation of chirped MM-Wave pulses emitted in free space provides a flexible and dynamic control method. The central frequency, chirp and temporal duration can be adjusted accordingly.

- Photonic generation of ultrafast chirped MM-Wave pulses can be used as a potential source for high throughput free space MM-Wave coherence tomography. The high speed source could be studied further to investigate its full utility in long range and short range sensing for potential applications pertaining to autonomous or driverless vehicles could be explored.

The main strength of this thesis is not related to theoretical developments but to its experimental findings. Although in general the work undertaken was quite challenging, and the results obtained not fully demonstrating state-of-the-art solutions yet, it opens very interesting area of research especially in MM-wave coherence tomography.

6.2 Contributions

The contributions of this thesis will be summarised in the following two sub-sections:

6.2.1. Conceptual Contributions

Industry 4.0 predicts computing and communication capabilities soon being embedded in all types of physical devices leading to the cyber world converging more and more with the physical world. Such physical devices are becoming more open, interactive and linked to other systems via the global data networks like the Internet. As a result, a new generation of systems is arising which can exploit and harness the eminent cyber-physical convergence (CPS). CPS essentially integrates computing, communication and storage capabilities with monitoring and or control of entities in the physical world using a complex wireless sensor network configuration, and must do so dependably, safely, securely, efficiently and in real-time. The technology shaping up in the next five years is gearing towards surpassing current systems in autonomy, adaptability, reliability, efficiency, functionality, security and safety. It is said that CPSs will improve not only current industry standards but also generate new industries, which will revolutionise our future. In this pursuit, exploiting inter-disciplinary knowledge and expertise such as microwave photonics to innovate advanced sensing solutions is cutting-edge research opening the gateway for future wireless and wired sensing networks. Microwave and MM-Wave pulse generation holds enormous promise. It enables us to detect a new range of phenomena in real time at high fidelity. As our lives become increasingly governed by data, and our physical world becomes increasingly intertwined with the cyber world, this particular source of rich, accurate, real-time data can only become more important.

6.2.2. Practical Contributions

Firstly, a novel demodulation scheme targeting a Michelson interferometer based strain sensing mechanism along the length of a chirped fibre Bragg grating enabling measurement at an ultrahigh-resolution and ultrafast rate is implemented. Previous studies focused on measuring the average strain value whereas our scheme is able to relate the strain applied at various spatial locations along the length of the grating itself. Besides, conventional fibre grating sensors do not differentiate between strain and or temperature variation as both correspondingly modify FBGs. Our interferometric interrogation scheme allows both reference and sample grating to be maintained at the same temperature and thus ensuring the only measurable difference in response is generated due to strain along the length of the sensor grating. The technique was extended to precisely locate a crack along the surface over which the CFBG is taut or embedded in. An ultrarapid measurement speed of 50 MHz with a high spatial resolution of 31.5 μm over a gauge length of 25 mm and a strain resolution of 9.1 με have been achieved.

Secondly, based on the same principles, i.e. photonic Time-Stretch enabled microwave and MM-Wave interferometry, infrared transparent samples are depth profiled to a very high accuracy using mode-locked infrared laser pulses as the probe beam and surface properties extraction based on reading the output microwave signal captured at the photodetector. IR probe beam is split into reference and sample arm. Samples of variable thickness are inserted in the sample arm, and a reflecting mirror is fixed at the end of both arms. Interference spectrum is mapped to a temporal replica, translating surface profile information to generated microwave and MM-Wave pulse. Information is encoded in instantaneous frequency along the temporal duration of generated microwave pulse. STFT analysis of signals obtained reveals an ultrafast surface scanning mechanism with high accuracy and real-time monitoring capability allowing the scheme to be employed for fast vibrating surface inspection such as aeroplane wing blades diagnosis etc. Ultrafast real-time measurement of glass slides (BK-7) of various thickness and thin films such as Mylar samples at a measurement speed of 50 MHz with a lateral resolution of 12.5 μm over a beam width of 3.83 mm and a depth resolution of 42.5 μm is achieved.

Finally, photonically generated chirped MM-Wave pulses are emitted in free space and implemented in a quasi-optical setup for MM-Wave CT applications. Photonic microwave generation schemes based on UB-TPS is initially exploited. The unique advantages based on a cascaded MZM scheme is outlined for the generation of chirped MM-Wave pulses. Simulations verify fourfold increase in TBWP of output signal. The practical challenges in the implementation of cascaded MZM scheme are outlined. Ultimately, a differential dispersion based chirped MM-Wave pulse generation setup is experimentally demonstrated. A frequency swept microwave signal with chirp rate 1.6 ~ 1.8 GHz/ns is experimentally verified. The generated chirped MM-Wave pulses allow good frequency sweep stability due to low jitter exhibited by Mode-Locked lasers. An ultrafast measurement and scanning capability is proposed for preliminary MM-Wave based Non-Destructive Testing. The thickness and optical path length measurements using MM-Wave CT is investigated.

6.3 Limitations and Future Work

Photonic Time Stretch in the 1550 nm is implemented to take advantage of minimum dispersion to attenuation ratio of components available in the telecommunication band. However, 1550 nm has limited utility in applications pertaining to biomedical imaging due to its poorer spectral resolution and water absorption properties. Both the fibre grating sensing resolution and dimensional metrology capability of the system is limited by the sampling rate of oscilloscope employed. The proposed experimental schemes for non-contact measurement are currently limited in obtaining a 3-D image of the surface or the volume content and non-uniform or multi-layer material characterisation making up the sample under test. Nor is it able to determine the size of a defect. The signal processing employed for extracting information from measured signal needs to be refined further to enable calculation of defect size, and depth and the complexity of the system could be reduced further to lower cost price of the system. Although the system has the capacity to carry out high throughput measurement, the measurement speed is limited by the width to which the pulse can be stretched before overlapping with neighbouring pulses and the need for calibration with a reference slows down the overall information processing ability. A limitation is also observed in the measurement of translucent and opaque materials; when the intensity of one of the arms falls, the interference fringes reduce and at a point where no light can transmit the sample material, interference fringes vanish. However, the visibility of the fringes could be used to estimate the absorptive properties of the sample under test, and thus the complex refractive index of the material can also be evaluated.

Future work can explore and investigate new and improved THz CT techniques to boost system performance.

- Researchers can employ advanced photonic integrated circuits (PICs) integrating waveguides, polarisation controllers, optical couplers and splitters. Since some optical components such as passive components can be integrated easily on a Silicon substrate and active components such as laser sources can be integrated on an Indium-Phosphide platform, a hybrid integration technology could reduce system footprint. A high detection bandwidth and advanced signal processing can improve the range resolution and subsequently replace large subsection of the equivalent fibre based Michelson interferometer reducing system cost even further.

- The demodulation scheme can be improved, and novel algorithms employed for obtaining multi-parameter sensing wherein the permittivity and permeability of material under test can be extracted as well. An extension of the famous Nicholson-Ross-Weir method can be applied to extract the complex refractive index from the reflection and transmission measurements through sample under test. The complex refractive index can in turn be related to the dielectric constant.

- Photonic generation of MM-Waves and sub-THz waves suffer from a degradation in output power, mainly due to the photodetectors optical responsivity and capability of state-of-the-art THz transmitters. Introducing multiple photodiode arrays and antennae arrays can overcome the transmitted power challenge.

- Similarly using state-of-the-art THz transistor amplifiers for boosting output power suffer from non-linearities introduced in the generated signal. Advanced THz amplifiers, with wider bandwidths at a reduced cost could enhance the progress made in the photonic sub-THz generation and detection applications.

- Enabling mode-locked lasers to generate microwave pulses at the bit rate of the laser also requires compatible detection electronics that can have a temporal response to cope with the pulse repetition rate and temporal duration. High-frequency amplitude detectors, which refer to MM-Wave detectors that can respond to the MM-Wave band of interest, with high temporal resolution could expand the utility of free space MM-Wave coherence tomography schemes.

- Testing an electronic device or system is an important aspect of industrial Quality Assurance and Engineering practices; applying the right stimuli to the device or system under test and analysing the resulting behaviour is an essential Quality Assurance practice. In some cases, stimuli supplied by an instrument such as an arbitrary waveform generator (AWG) to ensure repeatable and deterministic testing is required. As devices and interfaces become faster and more complex, the flexibility of test instruments becomes more and more critical. The underlying techniques outlined in this thesis provide a firm foundation for flexible chirp and shape control of the generated microwave and

MM-Wave waveforms and these techniques can be further improved on and applied accordingly.

- Due to the similarity of the underlying techniques with laser Doppler vibrometer, velocimetry, rapid surface diagnostics and surface metrology applications, novel demodulation schemes with enhanced resolution, unprecedented speed, economical equipment and ease of implementation can be exploited. The rate of change of displacement with time can be explored to obtain velocity or vibration measurement.

- The interferometric configuration leads to system instability, direct transmission and or reflection-based measurements can be explored and system complexity reduced. Near field imaging for enhanced resolution could be explored as well.

- Despite the fact that the Photonic Time-Stretch enabled system has empowered high-throughput measurement, the instruments innately create an amazingly high-rate information stream, which can be as high as one hundred billion bits for each second. This storm of information will overpower even the most advanced information securing circuits and the backend processors. Most electronic arrangements miss the mark for this situation because of the electronic bottleneck in speed and data transfer capacity. In this manner, new and productive photonic approaches, which highlight ultrafast speed and to a significant degree broadband transfer speed, are exceptionally requested to address the developing enormous information issues in ultrafast measurement frameworks. Compressive Sensing is a promising technique, which could take care of this issue.

APPENDIX A

```
%**********************************
%STFT analysis


y=load (filename);


scale=2000;   %ps/div
N=length(y); %sample points
x=zeros(N,1);
for i=1:N
    x(i)=i*scale*10/N;


end


t=x*1e-12;  %ps
M=length(y);
deltat=t(2)-t(1);
T=deltat*M;
t=(0:deltat:T-deltat);
deltaf=1/T;
F=1/deltat;
f=linspace(-F/2,F/2,M);


figure(1)
subplot(211)
plot(t*1e9,y);
subplot(212)
%Calculate fft of signal y
Y_w=fftshift(fft(y));
plot(abs(Y_w)); %plot absolute of fft of 'y'


Y_w(596:606)=0; %Remove the baseband
y_ac=real(ifft(ifftshift(Y_w))); %calculate inverse fft
plot(t*1e9,y_ac)
```

```
%Find instantaneous frequency and phase of signal
figure(2)
H_w=hilbert(y_ac); %calculate hilbert transform of baseband removed signal
phi=unwrap(angle(H_w),0.1*pi); %unwrap signal phase
subplot(211)
plot(t*1e9,phi);
subplot(212)
instant_freq=diff(phi); %calculate instantaneous frequency for signal
plot(t(1:N-1)*1e9,instant_freq);

%plot signal spectrogram (essentially magnitude square of short-time-fourier-
transform)
figure(3)
window=hann(300);
noverlap=290;
nfft=5*N;
Fs=100e9; % overall bandwidth
spectrogram(y_ac,window,noverlap,nfft,Fs,'yaxis');
%view(-27,62)
shading interp

%Fetch absolute max. instant. freq points along spectrogram
figure(4)
[S,F,T]=spectrogram(y_ac,window,noverlap,nfft,Fs,'yaxis');
instfq=zeros(1,length(T));
size(T)
for i=1:length(T)
   [Y,I]=max(abs(S(:,i)));
   instfq(i)=F(I);
end
plot(T,instfq,'-o')
```

APPENDIX B

```
%**********************************
%Finding envelope


pulse=y;
close all;hold on;Box on;
plot(pulse(:,1),pulse(:,2),'r')
package=100;num=0;envelope=zeros(length(pulse),2);
envelope(:,1)=pulse(:,1);
for sweep=1:package:(length(pulse)-package+1)
   [MAX COLUMN]=max(abs(smooth_pulse([sweep:sweep+package],2)));
   num=num+1;
   COLUMN_=package*(num-1)+COLUMN+1;
   envelope(COLUMN_,2)=pulse(COLUMN_,2);
end
plot(envelope(:,1),envelope(:,2),'k')
%**********************************
%finding suitable Gaussian function
[a b]=find(envelope(:,2)~=0);
Envelope(:,1)=envelope(a,1);
Envelope(:,2)=envelope(a,2);
plot(Envelope(:,1),Envelope(:,2),'.r')
Mu=sum(Envelope(:,1))/(length(Envelope(:,1))-1)
Variance=sum((Envelope(:,1)-Mu).^2)/(length(Envelope(:,1))-1)
a=1e-8/(sqrt(Variance)*sqrt(2*pi));
b=Mu;
c=sqrt(Variance);
IDEAL_ENVELOPE=a*exp(-(Envelope(:,1)-b).^2/(2*c^2))
% IDEAL_ENVELOPE=a*exp(-(([-5:.1:5]-b).^2/(2*c^2)))
plot(Envelope(:,1),IDEAL_ENVELOPE,'c')
threshold=1;
for a=0.6:0.01:0.8
   for b=2.20e-8:1e-10:2.22e-8
```

```
      for c=1e-10:1e-11:2e-8

         workshop=a*exp(-(Envelope(:,1)-b).^2/(2*c^2));
         error=abs(sum(abs(workshop)-abs(Envelope(:,2))));
         if error < threshold
         threshold=error
         close all;hold on;
         plot(Envelope(:,1),workshop,'.r')
         plot(Envelope(:,1),Envelope(:,2),'b')
         ENVELOP_DATA=[a b c];
         IDEAL_DATA=[Envelope(:,1),workshop];
         pause(.5)
         end

      end
   end
end

%********************************
%fft from pulse
close all;hold on;Box on;
y=smooth_pulse;
NFFT = 2^nextpow2(length(smooth_pulse)); % Next power of 2 from length of y
Y = fft(smooth_pulse(:,2),NFFT)/length(smooth_pulse);
T=smooth_pulse(end,1)/length(smooth_pulse);
Fs = 1/T;
f = Fs/2*linspace(0,1,NFFT/2+1);
% Plot single-sided amplitude spectrum.
plot(f,2*abs(Y(1:NFFT/2+1)))
title('Single-Sided Amplitude Spectrum of y(t)')
xlabel('Frequency (Hz)')
ylabel('|Y(f)|')
```

APPENDIX C

This appendix gives a list of the major components and measurement equipment used in this thesis.

Mendocino series FPL type C -band Desktop 1550nm femtosecond lasers

Operating Wavelength = 1550 nm

Optical Bandwidth = 9 - 16 nm

Average Output Power = 10 – 20 mW

Pulse width = 800 fs

Repetition rate = 50 MHZ

Optical Circulator - 1310/1550 nm (Thor Labs)

Optical circulator is a special fibre optic device that is capable of separating optical power traveling in opposite directions in one optical fibre. Typical isolation between ports 1 and 3 ~ 40 dB.

Optical Fibre Splitter (Thor Labs)

Split ratio = 50/50

Operation wavelength = 1550 nm

Temperature sensitivity = <0.002 dB/°C

Directivity and Return loss = > 55 dB

Dispersive Fibres (Thor Labs)

Dispersion = 17 ps/nm/km

Length = 20 km

Fibre Optic Retroreflectors (Thor Labs)

- SM, PM, or MM Fibre Optic Retroreflector Patch Cables
- One End has Protected Silver Mirror Coating
- $R_{avg} \geq 97.5\%$ from 450 nm to Fibre's Upper Wavelength Limit
- 2.0 mm Narrow Key FC/PC or FC/APC Versions Available
- Suitable for Laser Power up to 300 mW
- 1 m Long Cables

Broadband Photodetector (NewFocus)

These ultrahigh-speed New Focus photodetectors show flat response up to 45 GHz. Input power was 0.45 mW at 1.06 µm. Measurement accuracy is ±1.5 dB up to 40 GHz.

Mixed Signal Oscilloscopes (Tektronix)

Analogue Bandwidth = 23 GHz

Sample rate = 100 GS/sec

Record length = 31.25 M points

Agilent 86100A Sampling Oscilloscope

Key Features & Specifications

53 GHz optical channel for 9/125 fibres

- Wavelength range: 1000-1600 nm
- Characteristic rms noise: 60 uW (50 GHz BW / best sensitivity), 160 uW (53 GHz BW / best pulse fidelity)
- Maximum displayed peak power: 20 mW

63 GHz electrical channel with 1.85 mm male input

- Characteristic rms noise: 0.6 mV (43 GHz BW / best sensitivity), 1.7 mV (63 GHz BW / best pulse fidelity)
- Maximum input signal: ± 2 Vdc

Chirped Fibre Bragg Gratings (Aston University, Birmingham, UK)

Length = 25 mm

Bandwidth = 7 nm

Centre wavelength = 1550 nm

- **Tunable Optical Time Delay (Thor Labs)**
- **Diffraction Grating and Focussing Optics (Thor Labs)**

MVNA (AB MILLIMETER)

MVNA-8-350 is a vector network analyser (VNA), an instrument which measures the complex, or vector, impedance (a real and an imaginary part of the impedance or an amplitude and a phase of the microwaves) in the millimeter and sub-millimeter frequency domain.

The basic MVNA-8-350 configuration consists of:

- an MVNA central unit,
- a PC computer fitted with interface cards, running a powerful software package for command, data acquisition, processing and visualization,
- a graphic printer attached to the PC computer,
- a control oscilloscope visualizing in the real-time the detected millimeter waves amplitude, phase and signal-to-noise ratio.

Antennaes (Pasternack)

V band – 40 ~ 75 GHz

Omnidirectional

MM-Wave waveguides

V band: 40 – 75 GHz

Quasi-Optical Setup (VUB, ETRO)

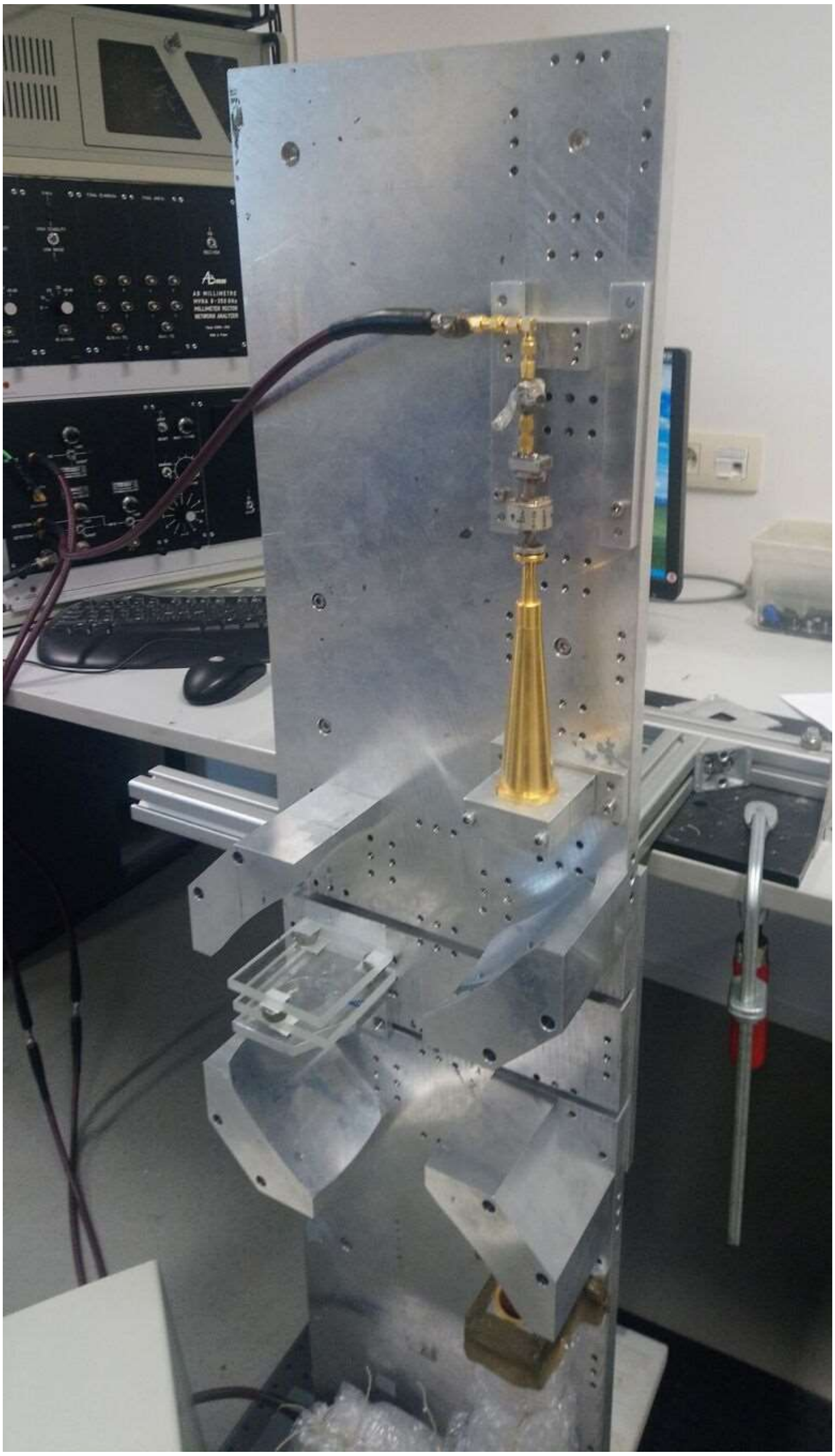

The free space quasi-optical MM-Wave setup is designed by the ETRO team at VUB. However, the setup was modified to implement MM-Wave coherence tomography.